2017

Investigation of Local Structures in Cation-Ordered Microwave Dielectric a Solid-State Nmr and First Principle Calculation Study

Rony Gustam Kalfarisi
College of William and Mary, rgkalfarisi@email.wm.edu

Investigation of Local Structures in Cation-ordered Microwave Dielectric
A Solid-state NMR and First Principle Calculation Study

Rony G. Kalfarisi

Williamsburg, Virginia

Master of Science, College of William & Mary, 2012
Bachelor of Science, University of Pelita Harapan (Indonesia), 2007

A Dissertation presented to the Graduate Faculty
of the College of William & Mary in Candidacy for the Degree of
Doctor of Philosophy

Department of Physics

College of William & Mary
August 2017

APPROVAL PAGE

This Dissertation is submitted in partial fulfillment of
the requirements for the degree of

Doctor of Philosophy

Rony G. Kalfarisi

Approved by the Committee, April, 2017

Committee Chair
Professor Gina L. Hoatson, Physics
College of William & Mary

Emeritus Professor Robert L. Vold, Applied Science
College of William & Mary

Professor Marc Sher, Physics
College of William & Mary

Professor Henry Krakauer, Physics
College of William & Mary

Eric J. Walter, Ph.D., IT/High Performance Computing Group
College of William & Mary

Professor Myriam Cotten, Applied Science
College of William & Mary

ABSTRACT

Solid-state Nuclear Magnetic Resonance (ssNMR) spectroscopy has proven to be a powerful method to probe the local structure and dynamics of a system. In powdered solids, the nuclear spins experience various anisotropic interactions which depend on the molecular orientation. These anisotropic interactions make ssNMR very useful as they give a specific appearance to the resonance lines of the spectra. The position and line-shape of these resonance lines can be related to local structure and dynamics of the system under study.

My research interest has focused around studying local structures and dynamics of quadrupolar nuclei in materials using ssNMR spectroscopy. ^{7}Li and ^{93}Nb ssNMR magic angle spinning (MAS) spectra, acquired at 17.6 and 7.06 T, have been used to evaluate the structural and dynamical properties of cation-ordered microwave dielectric materials. Microwave dielectric materials are essential in the application of wireless telecommunication, biomedical engineering, and other scientific or industrial implementations that use radio and microwave signals. The study of the local environment in terms of average structure, by method such as X-ray diffraction (XRD), is commonly used for exploring of the correlations between structure and properties of these materials. Extending this type of investigation to specific local structures, on distance scales of a few lattice spacings, can be achieved with the use of ssNMR techniques. Even though XRD results show cationic ordering at the B-site (third coordination sphere), NMR spectra show a presence of disorder in the materials. This was indicated by the observation of a distribution in NMR parameters derived from experimental ^{93}Nb NMR spectra and is supported by theoretical calculations.

TABLE OF CONTENTS

ACKNOWLEDGMENTS

I would like to express my gratitude to both my supervisors, Prof. Gina Hoatson and Prof. Robert Vold (professor emeritus of Applied Science) for providing guidance during my doctorate program in physics department with specialty in ssNMR spectroscopy. This research area is difficult one and both of my supervisors have shown their relentless support during the entire time of my research and study. Not only I have learned about ssNMR techniques, I also learned how to think critically in all situations which is an invaluable lesson. For this, I thank you both.

I want to acknowledge the tremendous help by my density functional theory (DFT) mentor Eric Walter, who has been really patient and helpful in guiding and teaching me to do first principle calculation using William and Mary high-performance computing cluster. I also would like to give a shout to my Indonesian friend, Christopher Hendriks, who has been giving a helpful suggestions in the technicality of the calulation. I'm deeply grateful to all the members of NMR lab group past and present. David Gerovski, Rachel Hynneman, and, especially to Jeremy Ellden for teaching me all the nuts and bolts of doing NMR experiments. Thank you all for the helps and great discussions.

I would like to recognise the tremendous help from the physics department at College of William and Mary which give financial support to all of the graduate students when there was no funding available from the group. Without its support, it would be difficult for me to continue the program (like many students that I know personally from different department/university).

Lastly, I would like to thank my family and, especially, my wife. My parents encouragement and prayers are appreciated despite living on opposite side of the Globe. My wife's encouragement that I need but don't deserve. For all of her patience through our journey together, I appreciate it sincerely.

I present this thesis in honor of my parents.

LIST OF TABLES

LIST OF FIGURES

INVESTIGATION OF LOCAL STRUCTURES IN CATION-ORDERED MICROWAVE DIELECTRIC

CHAPTER 1

Introduction

1.1 Background and Motivation

Oxides perovskites, chemical formula ABO_3, are probably the most widely studied metal oxides. In part, this is because of their ability to accommodate extensive chemical substitution on both the *A* and *B* sites. These complex oxides show a wide variety of interesting and useful physical and chemical properties. Modern wireless communication technology and microelectronics have benefited a lot from these types of materials [3]. Their importance can also be shown by the numerous researches and studies of their properties that have been done all over the world [4–10].

In microwave microelectronic technology, dielectrics are used the most for structural and assembly as well as for circuit application such as filtering, modulation, and detection. Solid dielectric materials are commonly used in the manufacture of many passive microwave components (such as microstrip lines, electrical capacitors, dielectric resonators, antennae, etc.) as well as active elements (such as phase shifters, modulators, detectors, etc). Primary design goal of the complex dielectric properties in

microwave ceramics include high dielectric constant ($\epsilon = 20 - 200$), low loss of electromagnetic energy at microwave frequencies, and good temperature stability of properties [11]. The continued development and improvement of this technology will rely upon our fundamental understanding to enhance performance and potential manipulation of these systems.

The physical and chemical characteristics of metal oxide perovskites are closely related to the identity and coordination environment of octahedral B-site cations. The ability to control the B-site cation, stoichiometry, and ordering therefore plays an important role in designing materials to have interesting electrical, magnetic, and mechanical properties. When B-site cations include more than one chemical element, the material is known as a complex perovskite, denoted by the chemical formula $AB'_xB''_{1-x}O_3$. The B′ and B″ cations can occupy B-sites in either random or ordered fashion. If an ordered arrangement is adopted, the symmetry and the size of the unit cell are changed. Thus, ordering of B-site cations has been identified by X-ray diffraction to adopt 1:1, 1:2, and 1:3 ordering along [111] direction [12, 13].

Previous works on cation-ordered microwave dielectrics have focused on understanding the relationship between the structure, stoichiometry, and chemistry in order to optimize the dielectric response of microwave ceramics [14, 15]. For some of these systems, the degree of chemical order on *B*-sites plays an essential role in contributing to the dielectric response and the highest performance was found to be associated with a fully ordered *B*-site sub lattice arrangement. Many studies have been performed on these and related materials using IR, Raman, and X-ray diffraction spectroscopy [12, 13, 16]. Dielectric loss characterizes the transformation of electrical energy into heat and is an important electrophysical parameter of the dielectric. However, the loss is to a large extent dependent on the presence of various type of defects or impurities within the system. Hence, it is interesting to study these materials with a complimen-

tary method such as solid-state NMR, that is sensitive to local chemical structure and dynamics, even in the absence of long range crystalline order.

Solid-state nuclear magnetic resonance (ssNMR) spectroscopy has proven to be a powerful method to probe the local structure and dynamics of a system [17]. In principle, it can detect all nuclei which possess nuclear spin through their interaction with an external magnetic field (Zeeman interaction). A number of anisotropic interactions make ssNMR very useful as they have a specific effects on the resonance lines of the spectra. The position and shape of these spectra can be related to local structure and dynamics of the system under study. The cloud of electrons surrounding the ions or molecules will adjust in such a way as to produce an induced magnetic field which opposes the external magnetic field [18]. As a consequence, this modifies the nuclear resonance frequencies and makes different electronic sites distinguishable. This *chemical shift* interaction is typically dominant in NMR spectra of nuclei with nuclear spin $I = 1/2$. For $I > 1/2$ nuclei, another important interaction arises from the electric field gradient (EFG) resulting from the local electric charge distribution interacting with the nuclear quadrupole moment of the observed nucleus.

Although NMR is a promising technique that may form a bridge between diffraction studies and microscopic observations based on the study of transition metal nuclei, there are a number of challenges that need to be addressed. Many nuclei encountered in transition metals have a large quadrupolar moment $e \cdot Q$. The strength of the interaction, expressed through the quadrupolar coupling constant $C_q = e^2qQ/h$, can be very large easily in the tens of MHz regime. Although this interaction can still be treated as a perturbation to the Zeeman Hamiltonian, in general it has to be treated as a second-order. Even at high external magnetic fields, the second-order interaction can result in megahertz line-broadening for nuclei such as ^{93}Nb. To excite such large bandwidth efficiently, very large rf-field strengths are needed. In addition, if more than one distinct

site is present in the system, spectral overlap is likely to occur, and this demands careful analysis using spectral deconvolution. Finally, to interpret NMR spectra in terms of structures, accurate quantum mechanical calculations, such as those available using first principles density functional theory (DFT), are desirable.

1.2 Structure of the Thesis

Chapter 1 is reserved for discussing fundamental concepts and key features of the solid-state NMR. In this chapter, the global Hamiltonian of an NMR system is defined and discussed.

Chapter 2 will be devoted to the analysis of cation-ordered microwave dielectric materials. This layered systems belong to the family of $A'_{1-x}A''_xB'_{1-x}B''_xO_3$ or $AB'_{1-x}B''_xO_3$. Structural analysis performed based on a combination of ^{7}Li and ^{93}Nb ssNMR techniques are shown.

Chapter 3 the spin dynamics of this system are investigated by measuring ^{7}Li nuclear spin lattice relaxation rates as a function of temperature and magnetic field strength.

Chapter 4 shows the quantum mechanical (density functional) calculation for some of the samples in the system. The model structures used in the calculations will be described to obtain NMR parameters.

Chapter 5 concludes the entire thesis with summary and prognosis for future work.

1.3 Basic Principles and Techniques of NMR spectroscopy

This section will focus on describing the basic principles of nuclear spin systems, the interactions of such systems to external magnetic fields and other sources of local

magnetic fields, the Hamiltonians that describe these interactions, and also introducing all quantities necessary for the quantum mechanical description of the systems.

Spectroscopy is branch of science concerned with the investigation and measurement of spectra produced when matter interacts with electromagnetic radiation. For the radiation to be able to interact with matter, the difference in energy levels should match the incoming/outgoing radiation energy and this condition is termed *"resonance"*. This idea forms the basis understanding for nuclear magnetic resonance (NMR). However, for NMR, the matter is under the influence of an applied magnetic field.

NMR was first observed in 1938 by Isidor Rabi. By extending the Stern-Gerlach experiment, he was able to measure the magnetic moment of a nucleus in molecular beam [19]. He was awarded the Nobel Prize in Physics for this breakthrough in 1944. Later in 1945, this phenomenon was observed by E. M. Purcell in solids [20] and by F. Bloch in liquids [21–23] the following year. Both of them share the Noble Prize in physics in 1952 for the development of methods in measuring precision NMR experiments. Rabi, Purcell, and Bloch observed that nuclei such as ^{1}H, ^{31}P, and ^{19}F when placed in magnetic field responded differently, i.e. each nucleus having specific absorption frequency. This gave them confidence that the NMR phenomenon would later turn out to become a very strong and powerful spectroscopic technique which can be applied to various branches of science.

During the 20 years after Bloch & Purcell's observations of NMR in bulk matter, a growing NMR community saw the discovery of spin echoes, general theories for spin-lattice and spin-spin relaxation, pure quadrupole resonance and multiple quantum NMR. Until 1966[1], NMR was studied primarily by continuous wave (CW) irradiation techniques, which suffered from inherent low of sensitivity. R. R. Ernst solved this problem by averaging the signal in the time domain following repeated RF-pulses

[1] Purcell and others used pulsed NMR well before FT-NMR was discovered.

with subsequent Fourier transformation to recover the spectrum [24]. Fourier transform NMR (FT-NMR) turned out to be a revolutionary way to study matter in which physicists, chemists, and biologists around the world now use to extract structural information and dynamics of the system of interest, and R. R. Ernst was awarded Noble prize in physics in 1991 for this discovery.

1.4 Quantum Mechanical Picture

1.4.1 Magnetic moment, nuclear spin, and spin states

Matter is composed of atoms, and atoms consist of nucleons and electrons. The electron can be viewed as orbiting a nucleus and possesses orbital angular momentum, denoted as *L*. In addition to this, electrons also possess an intrinsic angular momentum called spin. Spin is quantum phenomenon and cannot be thought as geometrical spinning of electron on its axis. The electron magnetic dipole moment $\boldsymbol{\mu_e}$, arises from this spin. Similarly, protons and neutrons also possess intrinsic spin, denoted as *I*, and hence nuclear magnetic moments $\boldsymbol{\mu_n}$. The overall spin of a nucleus is determined by the spin quantum number of its constituents. If the number of both protons ($I_p = 1/2$) and neutrons ($I_n = 1/2$) are even in a given nuclide, then $I = 0$. Just as electrons in atomic orbitals, even numbers of protons or even numbers of neutrons pair up giving zero overall spin. However, a proton and a neutron will have lower energy when their spins are parallel, rather than anti-parallel.

The magnetic moment operator is related to the spin operator according to the relation

$$\hat{\boldsymbol{\mu}} = \gamma\hbar\hat{\mathbf{I}} \tag{1.1}$$

where γ is known as nuclear gyromagnetic ratio, a constant for a given type of nucleus, and is given to a first approximation by,

$$\gamma = \frac{q}{2m} \tag{1.2}$$

q and m are nuclear charge and mass respectively. When the nucleus is put under static and uniform magnetic field, the nuclear magnetic moment will interact with it. The interaction of the nuclear spin in a static magnetic field is described by,

$$\hat{H} = -\hat{\boldsymbol{\mu}} \cdot \mathbf{B_0} \tag{1.3}$$

This hamiltonian is often referred to as the *Zeeman hamiltonian* where $\mathbf{B_0}$ is the static magnetic field and usually taken along the positive *z*-axis in the laboratory frame. So, combining (1.1) and (1.3), we have

$$\hat{H} = -\gamma \hbar B_0 \hat{I}_z \tag{1.4}$$

The *eigenfunctions* (or *eigenstates*) of $\hat{H}$ are the wavefunctions describing the possible states of the spin system in the $\mathbf{B_0}$ field. Since $\hat{H}$ is proportional to operator $\hat{I}_z$, this means they commute and they share the same eigen-functions. For simplicity, we use the eigen-functions of $\hat{I}_z$ as the shared eigenfunctions. Using Dirac *bra-ket* notation, these functions can be denoted as $|l, m\rangle$ where *I* is the nuclear spin quantum number. The quantum number *m* take values of $I, I-1, I-2, \cdots, -I$. The energies associated with different possible spin states are the eigenvalues of the operator $\hat{H}$. These

eigenvalues can be obtained by operating $\hat{H}$ to the spin wavefunctions,

$$\hat{H}\,|l,m\rangle = E_{l,m}\,|l,m\rangle \tag{1.5}$$

where $E_{l,m}$ is the energy of the eigenstate $|l,m\rangle$. Substituting (1.3) to (1.5) yields,

$$\hat{H}\,|l,m\rangle = -\left(\gamma\hbar B_0\right)\hat{I}_z\,|l,m\rangle = -\left(\gamma\hbar B_0\right)m\,|l,m\rangle \tag{1.6}$$

since $|l,m\rangle$ is an eigenfunctions of $\hat{I}_z$ with eigenvalue of *m*. The energies of the eigenstates are obtained by comparing (1.5) and (1.6), so

$$E_{l,m} = -\gamma\hbar B_0 m \tag{1.7}$$

As an example of a spin system with $I = \frac{1}{2}$, *m* takes value of $\pm\frac{1}{2}$. This suggests that there are two possible eigenstates with energy $E_{\frac{1}{2},\pm\frac{1}{2}} = \mp\frac{1}{2}\gamma\hbar B_0$. These states are frequently referred to as the *Zeeman states*. The difference of energy between these two states is $\Delta E = \gamma\hbar B_0$ and is called the transition energy. The associated transition frequency is $\omega = \gamma B_0$ (or $\nu_0 = \frac{1}{2\pi}\gamma B_0$) and this is called *Larmor frequency*.

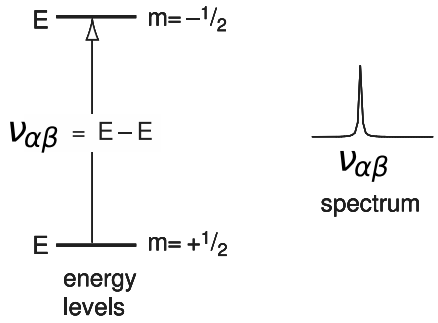

FIG. 1.1: The frequency $\nu_{\alpha\beta}$ of a spectral line matches the energy difference of the spin eigenstates.

1.5 Vector Model

For many spectroscopy techniques, it is sufficient to think about energy levels and selection rules. However, this is not true for NMR. For example, using only energy levels approach we cannot even describe how the most basic pulsed NMR experiments work, let alone the more complicated two-dimensional experiments. Even though the vector model can only be applied to a small number of situations, the ideas carry over into more sophisticated treatments. It is therefore essential to have a good understanding of the vector model and how to apply it.

1.5.1 Nuclei in a static, uniform magnetic field

The net nuclear magnetization $\mathbf{M}$ in a sample (i.e. equivalent to bulk nuclear magnetic moment) is the vector sum of all individual nuclear magnetic moments.

$$\mathbf{M} = \sum_i \boldsymbol{\mu_i} \tag{1.8}$$

If the nuclei are placed in a uniform magnetic field $\mathbf{B}$ as in the NMR experiment, a torque $\mathbf{T}$ is exerted on the magnetization vector

$$\mathbf{T} = \frac{1}{\gamma}\frac{d}{dt}\mathbf{M} \tag{1.9}$$

In this situation the torque is given by

$$\mathbf{T} = \mathbf{M} \times \mathbf{B} \tag{1.10}$$

Substituting (1.9) to (1.10), we get

$$\frac{d\mathbf{M}}{dt} = \gamma \mathbf{M} \times \mathbf{B} \tag{1.11}$$

which describes the motion of the magnetization vector **M** in the magnetic field **B**. The implication of Equation (1.11) is that suppose we, somehow, manage to tip the magnetization vector away from the *z*-axis such that it makes an angle θ from it, the magnetization vector will rotate around the direction of the magnetic field sweeping out a cone with constant angle. The vector is said to *precess* about the magnetic field and this particular motion is called *Larmor precession*. In NMR the magnetic field is taken to be $\mathbf{B} = (0, 0, B_0)$, and the frequency with which the magnetization precesses about this field, defined as ω_0, is known as the *Larmor frequency* [25].

$$\omega_0 = -\gamma B_0 \tag{1.12}$$

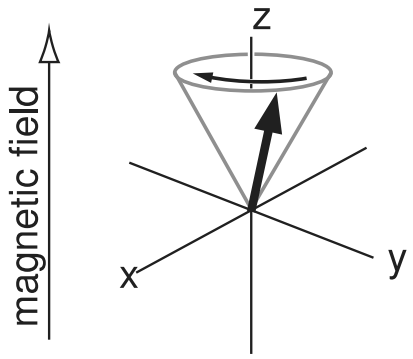

FIG. 1.2: Precession of magnetization vector around the magnetic field.

1.5.2 Detection

Larmor precession of the magnetization vector is what we actually induces and get detectable signal in NMR experiments. If a small coil is placed with its axis in the *xy*-plane, the magnetization vector will sweep through its cross-sectional area. According to Faraday's law, an induced current will be produced. This current, which is the NMR signal, can be amplified and recorded. Due to relaxation processes, the signal will decay hence it is called *free induction decay*, or FID.

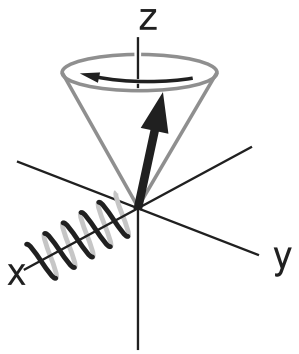

FIG. 1.3: Precessing magnetization will induce a current in the coil. This coil is part of an LC circuit and is tuned to the Larmor frequency.

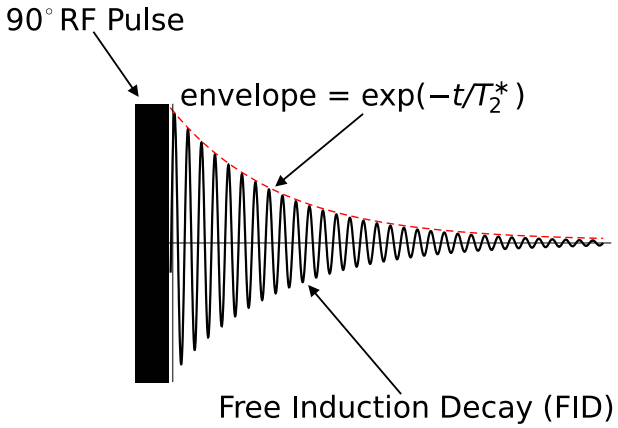

FIG. 1.4: The free induction decay (FID) of NMR signal.

1.5.3 The effect of RF pulses

The most important question now is how one turns the magnetization vector away from its equilibrium position along the *z*-axis. Theoretically, this is easy to achieve. We just need to replace (suddenly) the magnetic field along the *z*-axis with one in the *xy*-plane (for example along *x*-axis). Unfortunately, this is not practical since the static magnetic field is supplied by a powerful superconducting magnet and there is no way this can be switched off quickly.

One possible approach is using *resonance*. The idea is to apply a very small magnetic field along the *x*-axis which oscillates near or at the Larmor frequency. This method provides a convenient way since we can use the same coil to generate the oscillating magnetic field and to detect the precessing magnetization. All we need to do is supply radio-frequency (RF) power to the coil and the resulting current creates an oscillating magnetic field along the *x*-axis and this is called *radio-frequency* or *RF* field.

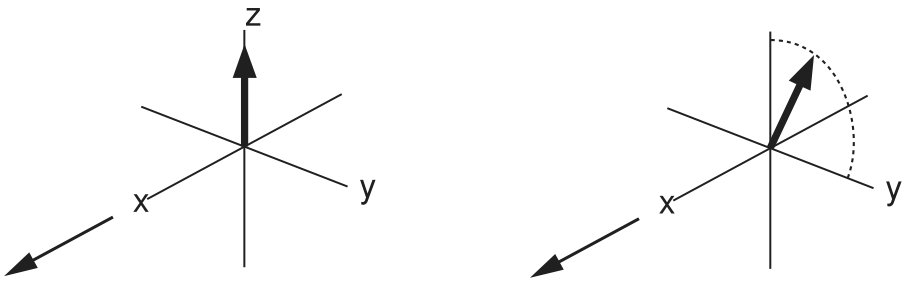

FIG. 1.5: The precession of magnetization vector around the *RF* field on the *x*-axis. As a result the magnetization vector will rotate away from its equilibrium position.

When RF power with frequency of $\pm\omega_{rf}$ is applied to the coil along the *x*-axis, the result is an oscillating magnetic field. The magnetic field moves back and forth along the $+x$ and $-x$ passing through zero along the way. This view is easy to picture, but it turns out, it's a lot easier to work out if the *linearly* oscillating magnetic field is replaced with two counter-rotating ones, as can be seen from Fig. 1.6. The frequency

of these two components can be written as $\pm\omega_{rf}$, where ω_{rf} is the frequency of the rf pulse. Furthermore, it can be shown that only the component, which rotates in the same sense as the precession of the magnetization vector, has any significant effect and we label this component $\mathbf{B}_1(t)$.

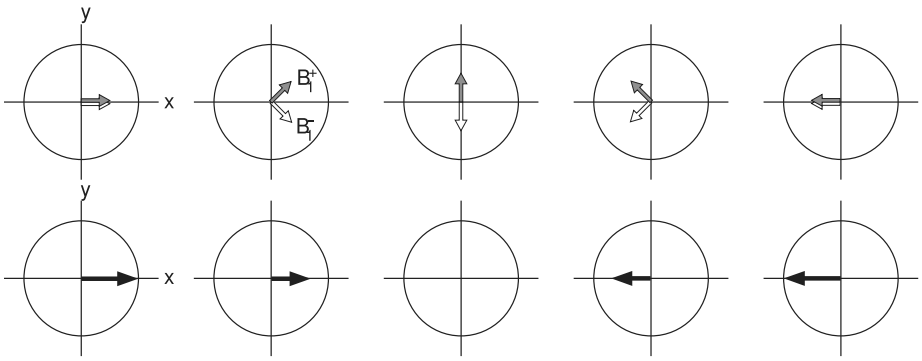

FIG. 1.6: A linearly oscillating magnetic field (bottom row) is equivalent to the counter-rotating components (top row) with half the amplitude.

The effect of this field can be easily seen by transforming the whole problem into a frame that rotates at frequency ω_{rf} around $\mathbf{B}_0$. In this frame, $\mathbf{B}_1(t)$ appears to be static, i.e. its time dependence has been removed. Also, if the pulse is *on resonance*, i.e. the frequency of the rotating frame is the same as the Larmor frequency ($\omega_{rf} = \omega_0$), the magnetization appears stationary. The *apparent* Larmor frequency in this frame is *zero*, in another words, the static magnetic field has been removed. The only field remaining in the rotating frame now is the effectively static $\mathbf{B}_1$ field. As a result, the magnetization vector will now precess around the resultant field, which is now only $\mathbf{B}_1$, at frequency $\omega_1 = -\gamma\mathbf{B}_1$ and this frequency is called the *nutation frequency*.

If the rf-pulse is applied for a duration τ_p with a magnitude B_1, the net magnetization **M** will be rotated at an angle

$$\theta_p = \omega_1\tau_p = -\gamma\mathbf{B}_1\tau_p \tag{1.13}$$

when the duration is such that the angle is 90° (magnetization vector is then in the *xy*-plane), we call that pulse a 90°-pulse.

1.6 General Expression of Nuclear Interaction

In addition to the interaction due to static magnetic field and the rf-pulses, nuclei also interact with other magnetic fields arising from their surroundings. These sources of magnetic fields are internal to the sample, and for solids can cause and extensive line broadening. Using quantum mechanics, it's possible to consider all the interactions of one nuclear spin with other magnetic field sources. The general Hamiltonian is thus described as the sum of individual terms,

$$\hat{H}_{tot} = \sum_i \hat{H}_{loc,i} \tag{1.14}$$

Each term in the Hamiltonian can be represented as the interaction of the nuclear spin of the *m*-th nucleus, $\hat{I}_m$, with a local magnetic field $B_{loc,i}$. The source of the local magnetic field determines the characteristic of the interaction

$$\begin{aligned} \hat{H}_{loc,i} &= -\gamma \hat{\mathbf{I}_m} \cdot \mathbf{B}_{loc} \\ &= -\gamma \left(\hat{I}_x B_x^{loc} + \hat{I}_y B_y^{loc} + \hat{I}_z B_z^{loc} \right) \end{aligned} \tag{1.15}$$

When we consider specific nuclear spin interactions, we will find that we can always express the local magnetic field $\mathbf{B}_{loc}$ as

$$\mathbf{B}_{loc} = \mathbf{A}_{loc} \cdot \mathbf{S} \tag{1.16}$$

where $\mathbf{A}_{loc}$ is a second-rank Cartesian tensor, often referred to as the *coupling tensor*. This tensor describes the interaction's strength and its orientation dependence. The vector **S** is the source of the local magnetic field, $\mathbf{B}_{loc}$, felt at the probed nucleus. For example, it will be another nuclear spin in the case of dipolar coupling and $\mathbf{B}_0$ itself in the case of chemical shielding. Hence, we can write a general contribution to the nuclear spin Hamiltonian from an interaction *A* as,

$$\hat{H}_A = -\gamma \hat{\mathbf{I}} \cdot \mathbf{B}_{loc} = \hat{\mathbf{I}} \cdot \mathbf{A}_{loc} \cdot \mathbf{S} \tag{1.17}$$

It's possible to choose one axis frame so that the interaction tensor is diagonal. This axis frame is called *principal axis* system and designated with capital letter as the subscript. The three principle values are frequently expressed as the isotropic value, A_{iso}, the anisotropy, Δ_A, and the asymmetry, η_A, of the interaction. These quantities are defined from the principle values as follows:

$$\begin{aligned} A_{\text{iso}} &= \frac{1}{3}\left(A_{XX} + A_{YY} + A_{ZZ}\right) \\ \Delta_A &= A_{ZZ} - A_{\text{iso}} \\ \eta_A &= \frac{A_{XX} - A_{YY}}{\Delta_A} \end{aligned} \tag{1.18}$$

We can picture an interaction tensor as being represented by an ellipsoid fixed within the molecule and centered on the nucleus being observed. The principal axis of the ellipsoid will coincide with the principal axis system of the interaction tensor and the length of each principal axis corresponds to the magnitude of the principal value of the interaction tensor. If the orientation of the molecules change, so does the interaction tensor. The interaction tensor also reflects the symmetry of the crystallographic site of the nucleus.

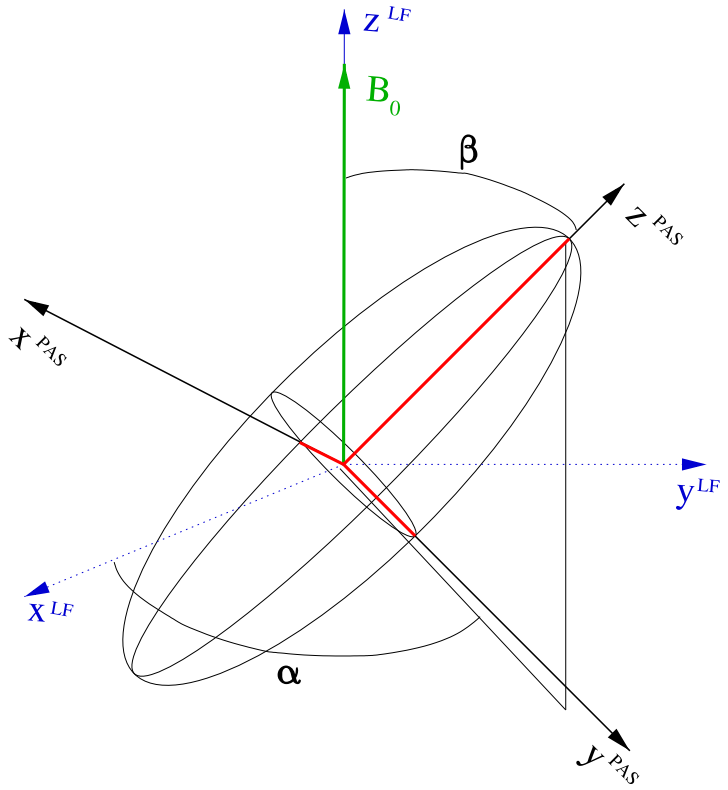

FIG. 1.7: Representation of an interaction tensor by an ellipsoid in the laboratory frame (LAB). The principal axes of the ellipsoid coincide with the interaction tensor principal axis system (PAS).

1.6.1 Cartesian and spherical tensor formalism

The interaction tensor often needs to be expressed in different coordinate system, thus rotation operations are needed. When tensors need to be expressed into a new coordinate system related to the old one by rotation operation about *Euler* angles (α, β, γ), it is more convenient to express the tensors with the use of spherical tensor formalism.

A second-rank tensor can be decomposed into three irreducible spherical tensors in terms of Cartesian components, based on the following relationship [26]

$$\begin{aligned}
A^{(0,0)} &= -\frac{1}{\sqrt{3}}\left(A_{xx} + A_{yy} + A_{zz}\right) \\
A^{(1,0)} &= -\frac{i}{\sqrt{2}}\left(A_{xy} - A_{yx}\right) \\
A^{(1,\pm1)} &= -\frac{1}{\sqrt{2}}\left[A_{zx} - A_{xz} \pm i\left(A_{zy} - A_{yz}\right)\right] \\
A^{(2,0)} &= -\frac{1}{\sqrt{6}}\left[3A_{zz} - \left(A_{xx} + A_{yy} + A_{zz}\right)\right] \\
A^{(2,\pm1)} &= \mp\frac{1}{\sqrt{2}}\left[A_{zx} + A_{xz} \pm i\left(A_{zy} + A_{yz}\right)\right] \\
A^{(2,\pm2)} &= \frac{1}{\sqrt{2}}\left[A_{xx} - A_{yy} \pm i\left(A_{xy} + A_{yx}\right)\right]
\end{aligned} \tag{1.19}$$

When the Cartesian tensor is symmetric and has zero trace, only five rank-two irreducible tensor components have non-zero values. This is the case, for example, for dipolar and quadrupolar interaction, while chemical shift has non zero trace.

From (1.17), we can express I_i and S_j as a unique tensor T_{ij}. Consider a dyadic product of

$$T_{ij} = I_i S_j \tag{1.20}$$

Using this definition, it is possible to rewrite the spin interaction Hamiltonian in terms of

irreducible spherical tensors

$$H = \sum_{k=0}^{2} \sum_{q=-k}^{+k} (-1)^q A^{(k,q)} T^{(k,-q)} \tag{1.21}$$

1.7 The NMR Hamiltonian in Solids

The total interaction energy of a nucleus is the result of the sum of all individual contributions experienced by the nucleus. The total NMR Hamiltonian is the sum of internal and external interactions.

$$\hat{H}_{total} = \hat{H}_{int} + \hat{H}_{ext} \tag{1.22}$$

Since NMR experiments involve putting the samples in static magnetic field and manipulating spin system using rf-pulse, the external Hamiltonian comprise of these two interactions and all other interactions form the internal Hamiltonian. Hence,

$$\hat{H}_{ext} = \hat{H}_{Zeeman} + \hat{H}_{rf}(t) \tag{1.23}$$

while,

$$\hat{H}_{int} = \hat{H}_{CS} + \hat{H}_D + \hat{H}_J + \hat{H}_Q + \hat{H}_{hyp} \tag{1.24}$$

The interactions in NMR solids are quite complicated due to the anisotropic terms, but they are very useful in providing information about the local structure of the system under study. The first term in (1.24) is the *chemical shielding* which defines the interaction between the nucleus and the local changes in magnetic field due to any changes in electron density. The *dipolar interaction* is direct and through-space interaction while

J-coupling term defines through-bonds interaction between the nuclei and is usually ignored since the CS and dipolar terms are usually large. The fourth term is called the *quadrupolar interaction* and only exist for nuclei with spin greater than half ($I > 1/2$). The last term is the *hyperfine interaction* (paramagnetic interaction) and this is due to the interaction of unpaired electron with the nucleus.

In NMR spectroscopy, it is generally the case that

$$\hat{H}_{ext} \gg \hat{H}_{int} \tag{1.25}$$

as far as this condition is valid, and particularly the Zeeman interaction is the dominant interaction, it's possible to consider the *z*-axis of the field B_0 as the quantization axis for the energy level of the system, *i.e.* the internal interactions can be considered as perturbation to the Zeeman interaction. Also, based on the magnitude of the interactions, there are only four terms that really matter in NMR solids and those are chemical shielding, dipolar interaction, quadrupolar interaction, and hyperfine interaction.

1.7.1 Shielding and chemical shift interaction, $\hat{H}_{CS}$

When a sample is put in a uniform static magnetic field, $\mathbf{B}_0$, the applied field will induce motion of electrons inside the molecules. This motion of electrons, in turns, will generate a local magnetic field $\mathbf{B}_{\mathrm{int}}$, known as nuclear shielding. This nuclear shielding will create a unique environment for the nucleus and allow us to differentiate each inequivalent nuclei in solids. The local field at a nucleus is therefore

$$\mathbf{B}_{loc} = \mathbf{B}_0 + \mathbf{B}_{\mathrm{ind}} \tag{1.26}$$

The magnetic shielding tensor is defined through the response of the system to an external uniform magnetic field. It relates the induced magnetic field at the nucleus position $\mathbf{B}_{\mathrm{ind}}(r)$ to the applied external magnetic field $\mathbf{B}_0$ according to

$$\mathbf{B}_{\mathrm{ind}}(r) = -\boldsymbol{\sigma}(r) \cdot \mathbf{B}_0 \tag{1.27}$$

According to Ramsey [27–29], the total nuclear shielding (NS), σ, has two contributions: diamagnetic (σ_D) and paramagnetic (σ_P) shielding

$$\sigma = \sigma_D + \sigma_P \tag{1.28}$$

The diamagnetic shielding contribution will result in shielding the nucleus (i.e. the induced field $\mathbf{B}_{\mathrm{int}}$ will oppose $\mathbf{B}_0$, hence reducing the effective Larmor frequency) while paramagnetic shielding will de-shield the nucleus (i.e. the induced field $\mathbf{B}_{\mathrm{int}}$ will have same direction as $\mathbf{B}_0$, hence increasing the effective Larmor frequency).

The chemical shielding Hamiltonian can be described as

$$\hat{H}_{CS} = -\sum_k \gamma_k \hat{\mathbf{I}}_k \cdot (\mathbf{1} - \boldsymbol{\sigma}) \cdot \mathbf{B}_0 \tag{1.29}$$

where $\hat{\mathbf{I}}_k$ is the nuclear spin angular momentum operator of the k-th nucleus and $\boldsymbol{\sigma}$ is 3×3 second rank tensor that describes the nuclear shielding as,

$$\boldsymbol{\sigma} = \begin{pmatrix} \sigma_{xx} & \sigma_{xy} & \sigma_{xz} \\ \sigma_{yx} & \sigma_{yy} & \sigma_{yz} \\ \sigma_{zx} & \sigma_{zy} & \sigma_{zz} \end{pmatrix} \tag{1.30}$$

where x, y, z is some unspecified axis frame. The tensor can be further decomposed

into *symmetric* and *anti-symmetric* components. In principal axis system, the tensor can be expressed as

$$\boldsymbol{\sigma}_{\mathbf{PAS}} = \begin{pmatrix} \sigma_{11} & 0 & 0 \\ 0 & \sigma_{22} & 0 \\ 0 & 0 & \sigma_{33} \end{pmatrix} \tag{1.31}$$

The principal values are assigned such that $\sigma_{33} \geq \sigma_{22} \geq \sigma_{11}$ (i.e. σ_{33} and σ_{11} are the most and least shielded components, respectively. The isotropic nuclear shielding (NS) is the average of the three principal values

$$\sigma_{\mathrm{iso}} = (\sigma_{11} + \sigma_{22} + \sigma_{33})/3 \tag{1.32}$$

NS values are described with respect to bare nucleus (i.e. with no electrons) which is completely de-shielded ($\sigma_{\mathrm{bare}} = 0$). However, it is not practical to measure NS of a bare nucleus, though one can calculate theoretical values with respect to this reference point. Experimentally, one measures *chemical shifts*, which are compared against a reference standard. Hence, the chemical shift (CS) is the shielding of a nucleus of the sample, σ_{sample}, with respect to reference standard, σ_{ref}.

$$\delta_{ii}^{\mathrm{sample}} = -\left(\frac{\sigma_{\mathrm{iso}}^{\mathrm{ref}} - \sigma_{ii}^{\mathrm{sample}}}{1 - \sigma_{\mathrm{iso}}^{\mathrm{ref}}}\right) \approx -\left(\sigma_{\mathrm{iso}}^{\mathrm{ref}} - \sigma_{ii}^{\mathrm{sample}}\right) \tag{1.33}$$

Hence, the isotropic chemical shift (the most important quantity in the context of high-resolution NMR) can be determined as,

$$\delta_{\mathrm{iso}}^{\mathrm{sample}} = -(\sigma_{\mathrm{iso}}^{\mathrm{ref}} - \sigma_{\mathrm{iso}}^{\mathrm{sample}}) \tag{1.34}$$

There are a number of different conventions for describing the shielding anisotropy.

In this thesis, to enable a clear comparison with the experimental data, the shielding tensor are defined according to Haeberlen-Mehring-Spiess convention where the principal components of are arranged such that

$$|\delta_{33} - \delta_{\mathrm{iso}}| \geq |\delta_{11} - \delta_{\mathrm{iso}}| \geq |\delta_{22} - \delta_{\mathrm{iso}}| \tag{1.35}$$

The isotropic chemical shift is given by

$$\delta_{\mathrm{iso}} = (\delta_{11} + \delta_{22} + \delta_{33})/3 \tag{1.36}$$

while the chemical shift anisotropy is characterized by

$$\Delta_{\delta} = \delta_{33} - \delta_{\mathrm{iso}} \tag{1.37}$$

and the anisotropy

$$\eta_{\delta} = (\delta_{22} - \delta_{11})/(\delta_{33} - \delta_{\mathrm{iso}}) \tag{1.38}$$

In solutions, the molecules are moving and tumbling rapidly in random fashion. In effect, this averages out the CSA and only sharp peak is observed on the spectrum. This peak corresponds to the isotropic chemical shift, δ_{iso}. However, this is not the case for solid-state NMR. In solids, broad powder patterns are often observed due to CSA where all possible tensor orientations are present. The effect on the spectrum is shown in Fig. 1.8.

1.7.2 Dipolar interaction, $\hat{H}_D$

Each nucleus with an associated nuclear spin I has a magnetic moment $\boldsymbol{\mu}$ and will generate a local magnetic field that is experienced by other nuclei. This interaction

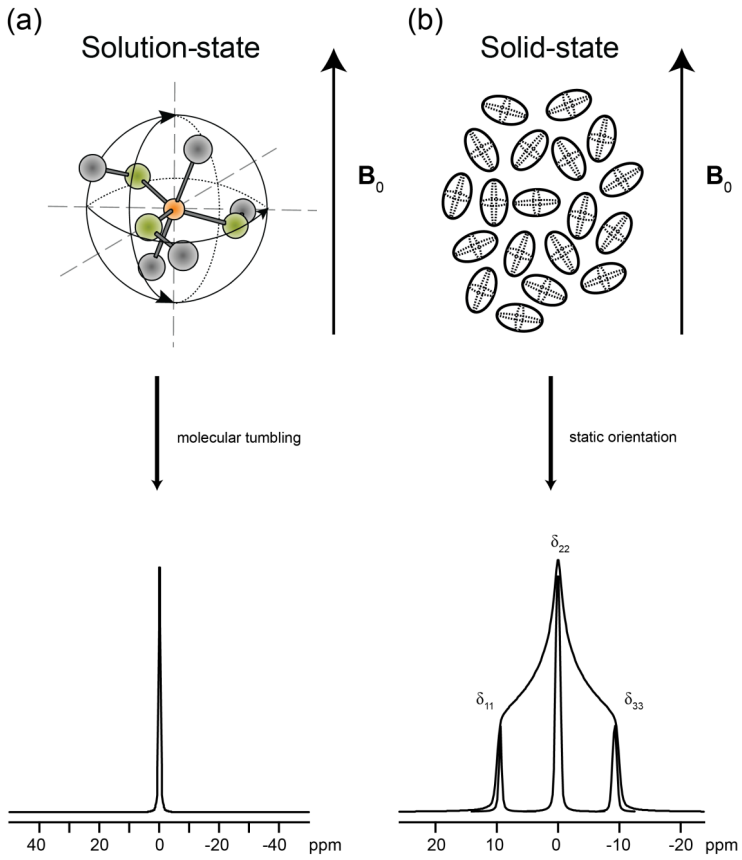

FIG. 1.8: (a) Rapid molecular tumbling in solutions serve to averages out the CSA to isotropic value. (b) Simulated static spectrum

occurs through space and is called the direct dipole-dipole coupling. In solutions, this interaction averages out to zero due to rapid molecular tumbling, where as in solid systems it is one of the major cause of line broadening. By extending the classical picture for dipole-dipole interaction, we can write the dipolar interaction Hamiltonian between spin I and S as

$$\hat{H}_D = -\frac{\mu_0}{4\pi}\gamma_I\gamma_s\hbar\left\{\frac{\hat{\mathbf{I}}\cdot\hat{\mathbf{s}}}{r^3} - 3\frac{(\hat{\mathbf{I}}\cdot\mathbf{r})(\hat{\mathbf{S}}\cdot\mathbf{r})}{r^5}\right\} \tag{1.39}$$

Alternatively, we may express the dipolar interaction Hamiltonian in the Cartesian tensorial form

$$\hat{H}_D = -2\hat{\mathbf{I}}\cdot\hat{\mathbf{D}}\cdot\hat{\mathbf{S}} \tag{1.40}$$

where the spin S is the ultimate source of local magnetic field at nucleus I. The tensor **D** is the dipole coupling tensor, with principal value of $-d/2, -d/2, +d$ where d is known as *dipolar coupling constant* (in unit of rad·s^{-1}) and given by

$$d = \frac{\mu_0}{4\pi}\gamma_I\gamma_s\hbar \tag{1.41}$$

1.7.3 Quadrupolar interaction, $\hat{H}_Q$

More than 70% of NMR active nuclei have a nuclear spin greater than $1/2$ and therefore they possess an electric quadrupole moment. This nuclear quadrupole moment comes from the non-spherical distribution of the positive charge at the nucleus [30, 31] and it will interact with electric field gradients (EFG) at the site of the probed nucleus. This EFG comes from the surrounding nuclei, electrons, and reflects the local symmetry [32, 33]. The quadrupolar interaction has the effect of changing the nuclear spin levels and energies. The magnitude of this interaction depends on the nuclear

quadrupole moment and the EFG at the center of the nucleus. The quadrupolar interaction Hamiltonian can be described as

$$\hat{H}_{\mathrm{Q}} = \frac{eQ}{2I(2I-1)\hbar}\hat{\mathbf{I}} \cdot \mathbf{V} \cdot \hat{\mathbf{I}} \tag{1.42}$$

where eQ is the nuclear quadrupole moment. The quadrupolar interaction tensor **V** can be diagonalized to transform the EFG to its principal axis system

$$\mathbf{V}_{\mathrm{PAS}} = \begin{pmatrix} V_{11} & 0 & 0 \\ 0 & V_{22} & 0 \\ 0 & 0 & V_{33} \end{pmatrix} \tag{1.43}$$

The magnitude of the quadrupolar interaction is typically described by the *quadrupolar coupling constant* and defined by

$$C_{\mathrm{Q}} = \frac{eQV_{33}}{\hbar} = \frac{e^2qQ}{\hbar} \tag{1.44}$$

Since $V_{33} = eq$ the EFG tensor is connected to the local symmetry of the nucleus under study, this reflects the electronic structure and bonding situation surrounding the nucleus. The symmetry of the environment will be reflected by the asymmetry parameter, η_Q, which is defined by

$$\eta_Q = \frac{V_{11} - V_{22}}{V_{33}}, \tag{1.45}$$

where $|V_{11}| \leq |V_{22}| \leq |V_{33}|$ are the principal axis values of the EFG tensor and using this we have $1 \geq \eta_{\mathrm{Q}} \geq 0$. This tells us, the higher the symmetry the less the magnitude of C_{Q} will be [34]. Alternatively, the quadrupolar interaction sometimes reported in the

form of the quadrupolar frequency, which is defined as

$$\omega_{\mathrm{Q}} = \frac{3C_{\mathrm{Q}}}{2I(2I-1)} \tag{1.46}$$

Under, the high-field approximation ($\omega_0 \gg \omega_{\mathrm{Q}}$), the quadrupolar interaction may be treated as a perturbation to Zeeman interaction. In most cases, quadrupolar interaction is quite big and this can be seen from the value of C_{Q} that can range from a few kHz to several MHz. Hence, it's necessary to treat the perturbed Hamiltonian through the second order. Thus, the quadrupolar Hamiltonian can be written as

$$\hat{H}_{\mathrm{Q}} = \hat{H}_{\mathrm{Q}}^{[1]} + \hat{H}_{\mathrm{Q}}^{[2]} \tag{1.47}$$

By only taking secular terms in the quadrupolar Hamiltonian (ones that commute with $\hat{I}_z$), we have

$$\hat{H}_{\mathrm{Q}}^{[1]} = \frac{eQ}{4I(2I-1)\hbar}\frac{\sqrt{6}}{3}[3\hat{I}_z^2 - I(I+1)]V^{(2,0)} \tag{1.48}$$

and

$$\hat{H}_{\mathrm{Q}}^{[2]} = -\frac{1}{\omega_0}\left\{\frac{eQ}{4I(2I-1)\hbar}\right\}^2 \times \big\{2V^{(2,-1)}V^{(2,1)}\hat{I}_z[4I(I+1) - 8\hat{I}_z^2 - 1] + 2V^{(2,-2)}V^{(2,2)}\hat{I}_z[2I(I+1) - 2\hat{I}_z^2 - 1]\big\} \tag{1.49}$$

Taking into account the first and second order quadrupole terms, $\hat{H}_{\mathrm{Q}}^{[1]}$ and $\hat{H}_{\mathrm{Q}}^{[2]}$, the Zeeman energy levels get shifted. Since $\hat{H}_{\mathrm{Q}}^{[1]}$ is an even function of $\hat{I}_z$, the energy-level shifts having the same magnetic number $|m|$ are shifted by the same amount, that is $\langle m|\, \hat{H}_{\mathrm{Q}}^{[1]}\, |m\rangle = \pm\omega_{\mathrm{Q}}$. For spin $I = \frac{3}{2}$, the transition $\left(-\frac{1}{2} \leftrightarrow \frac{1}{2}\right)$ is called the central transition and the other two transitions $\left(-\frac{1}{2} \leftrightarrow -\frac{3}{2}\right)$ and $\left(\frac{1}{2} \leftrightarrow \frac{3}{2}\right)$ are called satellite transitions. As can be seen from Fig. 1.9, the CT is not affected by $\hat{H}_{\mathrm{Q}}^{[1]}$ while the ST are shifted by

$\pm 2\omega_{\mathrm{Q}}$.

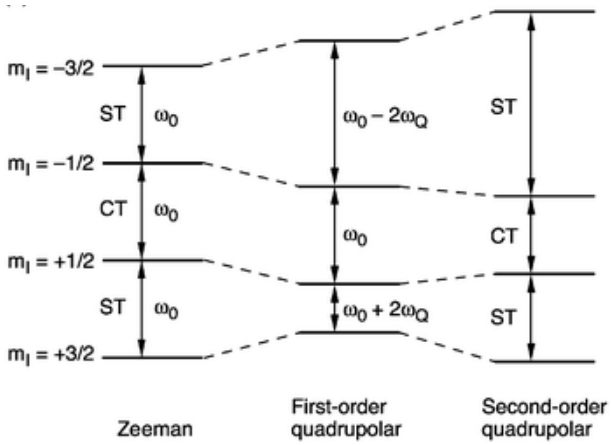

FIG. 1.9: The energy level diagram for spin $I = 3/2$ nucleus showing the effect of Zeeman, first order, and second order quadrupolar interaction.

The second order effect of $\hat{H}_{\mathrm{Q}}^{[2]}$ is to shift the energy levels further. An additional shift called *second-order quadrupole shift* occurs for each transition line. As $\hat{H}_{\mathrm{Q}}^{[2]}$ is and odd function of $\hat{I}_z$, the energy-level shifts having the same magnetic number $|m|$ are shifted by the same quantity but in the opposite direction.

1.8 High-resolution in ssNMR Experiments

In solid-state NMR, we generally deal with powder samples, that is samples containing many crystallites with random orientations. All nuclear spin interactions that have been discussed in previous sections are quite similar in form. Particularly, the interactions for the same tensor rank are dependent on crystallite orientation (they also behave in exactly the same way). As a result, NMR spectra of polycrystalline powder samples consists of broad lines, or *powder patterns*. When there is more than one inequivalent nuclear site present in the system, the powder patterns from each site may overlap. This will render NMR spectrum more difficult to analyse for structural determination.

One technique that has been used primarily in ssNMR to increase spectral resolution and sensitivity is called magic angle spinning (MAS). This is achieved, suggested by its name, by spinning the sample at an angle $\theta_m = 54.74^\circ$ (magic angle) with respect to static external magnetic field. With this technique, the dipole-dipole interaction averages to zero while CSA interaction averages to its non-zero value (the *isotropic chemical shift*) at magic angle. However, for the quadrupolar interaction, only the first order terms are fully averaged by MAS leaving residual second order-quadrupolar broadening.

In analysing powdered or disordered samples with moderately strong quadrupolar couplings, all the allowed $\Delta S_z = \pm 1$ transitions will be broadened, in most cases, beyond the NMR detection limit except the $\left(\pm\frac{1}{2} \leftrightarrow \mp\frac{1}{2}\right)$ transition (central transition or CT). It is consequently on these CTs that most ssNMR of half-integer quadrupolar nuclei are focused on. A number averaging procedures have been proposed, capable of achieving high-resolution NMR to quadrupolar nuclei [35–39]. These are double rotation (DOR), dynamic-angle spinning (DAS), multiple-quantum magic angle spinning (MQMAS), and satellite transition magic angle spinning (STMAS). But the most practical and widely used techniques are MQMAS and STMAS. In this thesis we will focus on understanding the local structure and dynamics of cation-ordered microwave dielectric materials using ssNMR spectroscopy of quadrupolar nuclei. This investigation is crucial since ssNMR spectroscopy can give additional information to diffraction studies and may form a bridge to microscopic observations in the study of transition metal of complex perovskite structures.

1.8.1 Magic angle spinning (MAS)

Rapid isotropic molecular tumbling of molecules in solutions serves to average anisotropic NMR interactions to their isotropic values, giving rise to high-resolution NMR

spectra. In solids, we achieve a similar effect by introducing a coherent sample rotation about a laboratory fixed axis at certain angle with respect to the magnetic field. To do this, the powdered sample is put inside a container (i.e. rotor) and spun at a constant rate, ω_R. In a strong magnetic field, the secular part ($T^{(2,0)}$) of all second rank tensor interactions has the same angular dependence, $(3\cos^2\theta - 1)$, where θ is the angle between the rotor axis and the magnetic field. This term is zero when $\theta = 54.74^\circ$, hence the name *magic angle* since this removes the anisotropic part of interaction tensor.

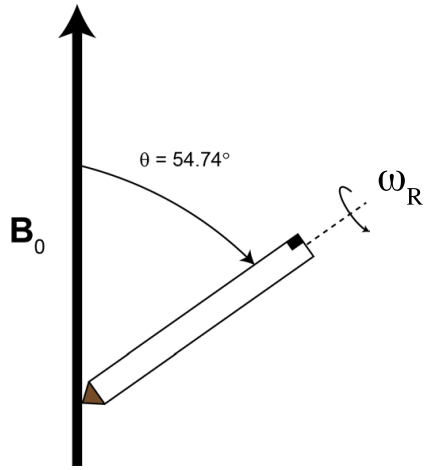

FIG. 1.10: The schematic for sample rotation at magic angle $\theta = 54.74^\circ$.

Moreover, it can be shown that for sample rotation rates on the order of the interaction strength or greater, the coherent time-dependence of the non-secular terms ($T^{(2,\pm1)}$ and $T^{(2,\pm2)}$) produce a manifold of spinning side-bands at multiple of the spin-rate. The isotropic tensor component ($T^{(2,0)}$) is invariant to rotation and yields a single narrow peak at the isotropically averaged frequency.

In many software packages that calculate and simulate MAS spectra, the model assumes infinite spin-rate and hence omits the side-bands. Slower spinning rate (i.e. the rate is comparable to anisotropic magnitude or even less) will produce *spinning side-bands* in addition to the isotropic chemical shift. The spinning side-bands are sharp lines that trace-out the *anisotropic* part of the ($T^{(2,0)}$) tensor. It is noteworthy that

the isotropic value will not always be the most intense line. The illustration of MAS on the chemical shift can be seen from Fig. 1.11 and isotropic chemical shift is highlighted inside the red box.

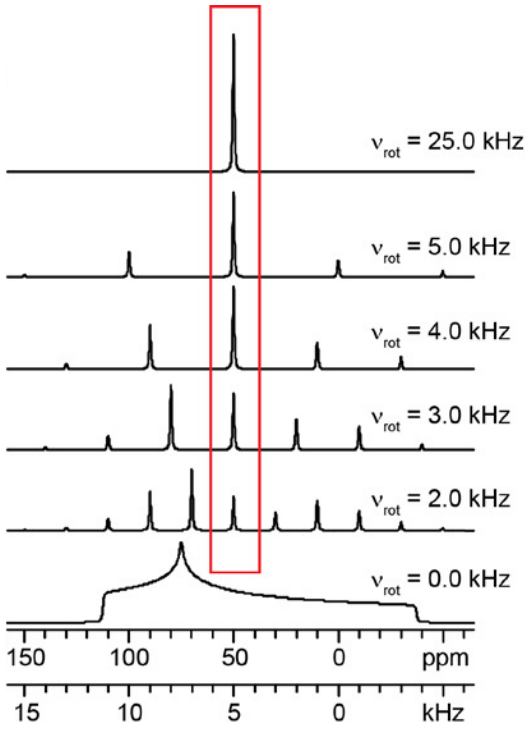

FIG. 1.11: Simulated spectra illustrating the effect of MAS on a $I = \frac{1}{2}$ nucleus.

1.8.2 Pulse sequences

Spin-echo or Hahn-echo

The NMR signal observed following an initial excitation pulse decays with time due to spin relaxation, and also any inhomogeneous effects which cause different spins in the sample to precess at different rates. The first of these, relaxation processes, leads to irreversible loss of transverse magnetization. However, inhomogeneous dephasing can be reversed by applying a 180° inversion pulse that inverts the precessing magnetization vectors [40]. Examples of inhomogeneous effects include a magnetic

field gradient and a distribution of chemical shifts. If the inversion pulse is applied after a period t of de-phasing, the inhomogeneous evolution will re-phase to form an echo at time $2t$. In simple cases, the intensity of the echo relative to the initial signal is given by $\exp^{-2t/T_2}$ where T_2 is the time constant for spin-spin relaxation.

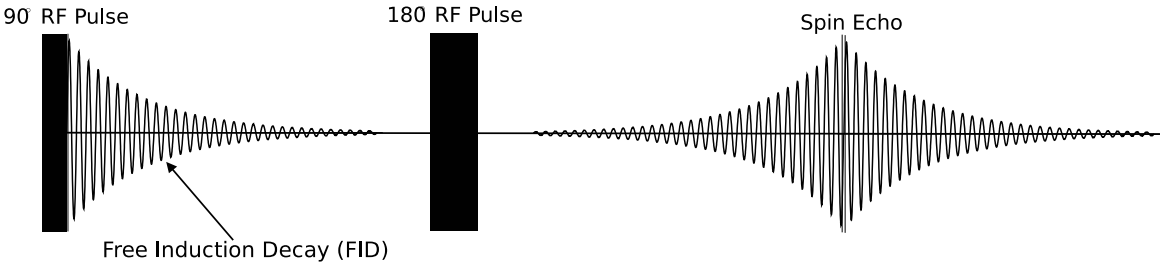

FIG. 1.12: The *echo* signal detection after appling 180° pulse.

1.8.3 Multiple quantum magic angle spinning (MQMAS)

The CT of quadrupolar nuclei under MAS is much narrower than the powder pattern observed under static condition. However, the anisotropic effects of the second-order quadrupolar interaction cannot be average out completely by conventional MAS experiments. Therefore, difficulties can arise when extracting information from MAS spectra with multiple resonances. Many different techniques have been developed in order to average the second-order quadrupolar interaction and acquire high-resolution spectra of quadrupolar nuclei, such as DOR and DAS which unfortunately require specialize probes. Fortunately, one NMR technique was developed using a clever method to correlate multiple- and single-quantum coherences that utilizes a conventional MAS probe. This technique is widely known as multiple-quantum MAS or MQMAS [39] for short. Multiple-quantum coherences are established with high power radio frequency pulse and then the spin systems are allowed to evolve during a period t_1 called the *evolution time*. A "mixing" pulse (or pulse sequence) is applied to convert the multiple-quantum

coherence to observable signal. In NMR, the observable signal has $\Delta m = \pm 1$ coherence and by convention focused on -1 pathway. After mixing, the resulting signal is observed and recorded in the detection time t_2. In order to get two-dimensional (2D) spectra, the evolution time t_1 is incremented and the signals are Fourier transformed with respect to both t_1 and t_2.

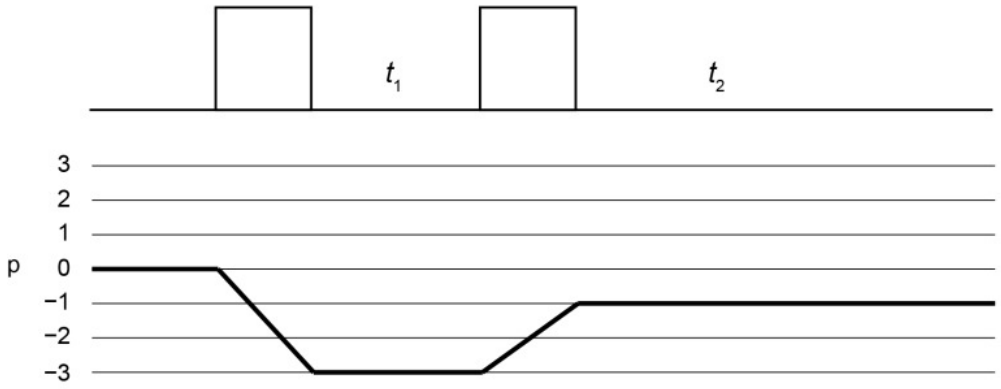

FIG. 1.13: Pulse sequence and one possible coherence pathway diagram for 3QMAS.

Unfortunately, this method will produce a *phase-twisted* lineshape which cannot be phased correctly. Therefore, modifications to the original experiment have been developed to ensure that the lineshape can be phased properly. This includes the phase- and amplitude-modulated experiments with respect to the t_1 increments. One dimensional (1D) spectra which correspond to isotropic resonances can be obtained by taking orthogonal projection along the slope of lineshape ridges. The slope of these ridges depends on the spin system and is called the MQMAS ratio, *R*. In practice, a mathematical transformation, known as shearing, is applied to the spectra which adjust the ridges so that they are parallel with respect to F_2 dimension. Using this transformation, the isotropic projections can be easily obtained and analysed.

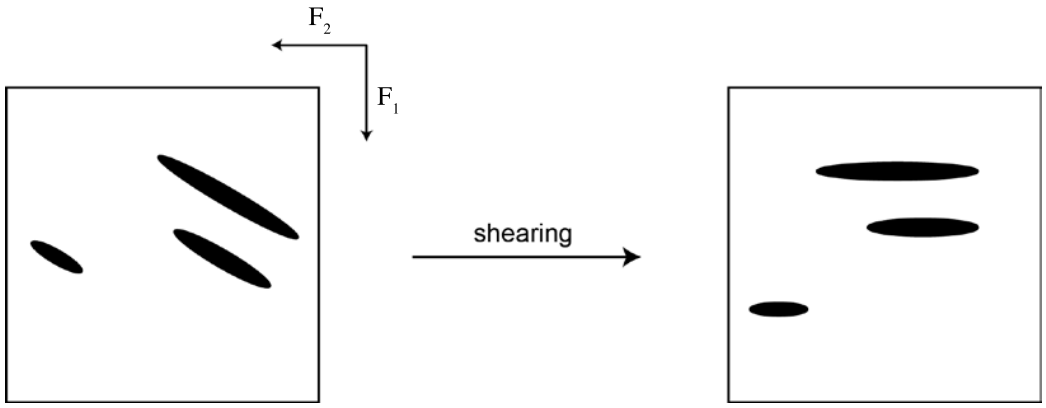

FIG. 1.14: Representation of shearing transformation on MQMAS spectrum.

CHAPTER 2

Complex Perovskite: Microwave Dielectrics

2.1 Introduction

Many electronic ceramics which have interesting physical properties, such as ferroelectric, piezoelectric, high-temperature superconductor and colossal magneto-resistive materials have perovskite or perovskite-related structures. Microwave ceramics are oxide perovskites that have been widely studied in part because of its technological application to wireless communications. The ability of perovskites and perovskite-related structure to accommodate a wide range of atomic substitutions results in a wide range of chemical and physical properties. These oxides provide a unique platform to study correlations between structure and bulk properties. When the A- and/or B-sites contain mixtures of two or more different atoms, the ability to control positional ordering of the cations in a complex perovskites gives rise to unique electronic responses of the materials.

Many well known perovskite materials have complex compositions with mixtures of cations on A- and/or B-site. These include technologically important ferroelectric (e.g. $PbZr_{(1-x)}Ti_xO_3$ or PZT) and microwave dielectrics (e.g. $BaZn_{1/3}Ta_{2/3}O_3$ or BZT). In these systems, additional changes in overall symmetry can arise from the ordering of different cations occupying the same site. Octahedral tilting and chemical ordering on the crystal chemistry of the perovskites has a huge impact on the physical characteristics of the materials. Distortion of the octahedra through Jahn-Teller effects is not expected to play a role in the d^0 systems of interest here and is not discussed.

2.2 Overview of Perovskite Crystal Structure

Perovskites have a cubic crystal structure with general formula ABO_3. In this structure (as can be seen from Fig. 2.1) An A-site cation is positioned at the corner of the cube and is usually an alkaline earth or rare earth element. The B-site cations, positioned on the center of the cube, could be 3d, 4d, 5d transition metal elements, while oxygen atoms are positioned at the face of the cube. In an ideal cubic perovskite, the A- and B-sites cations find their equilibrium bond distance to oxygen without any distortion of the unit cell. This happens when A-site cations are in contact with twelve oxygen atoms and B-site cations are in contact with six oxygen atoms, hence we have $d_{A-O} = \sqrt{2}d_{B-O}$. However, in the majority of complex perovskites, the A-O and B-O bond lengths are geometrically incompatible due to the different sizes of the atoms.

To predict whether a combination of A- and B-site cations are likely to produce a perfect or distorted perovskite structure, a criterion was devised called Goldschmidt tolerance factor [41]

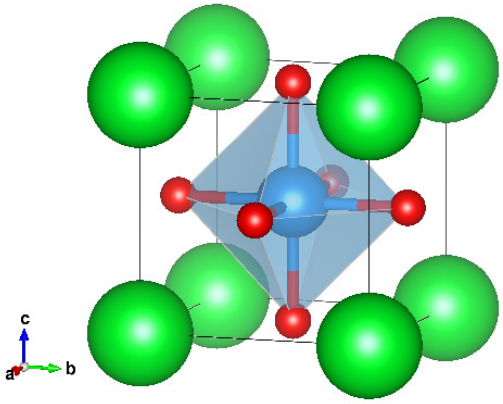

FIG. 2.1: Ideal cubic of ABO_3 perovskite structure. A-sites ion is marked green, B-sites ion is light blue, and oxygen atoms are red

$$t = \frac{r_A + r_O}{\sqrt{2}(r_B + r_O)} \tag{2.1}$$

where r_A, r_B, and r_O are the radii of A-site, B-site, and oxygen atoms and using this criterion we have $t = 1$ for ideal perovskite. A large number of metallic elements are stable in the perovskite structure if the tolerance factor *t* is in the range of 0.75 - 1.06 [42]. The alternative view for perovskite structure with cubic symmetry can be described as consisting of corner-sharing BO_6 octahedra with the A-site cation sitting in the middle of the cube of eight such octahedra surrounded by 12 oxygen anions.

When A-site cation is too small for its cage (i.e. $t < 1$, e.g. $CaTiO_3$), the surrounding BO_6 octahedra can tilt to decrease the A-O bond length and lower the coordination number for the A-site cation. When the B-site cation is too small for its cage ($t > 1$, e.g. $BaTiO_3$ or $PbTiO_3$), it adopts an off-centred coordination and destroys the centre of symmetry of the unit cell. In some cases, this change gives rise to a ferroelectric response. Any distortion will lower the symmetry of the structure. Perovskites with $t < 1$ may exhibit tetragonal, rhombohedral, orthorombic, and monoclinic distortion of

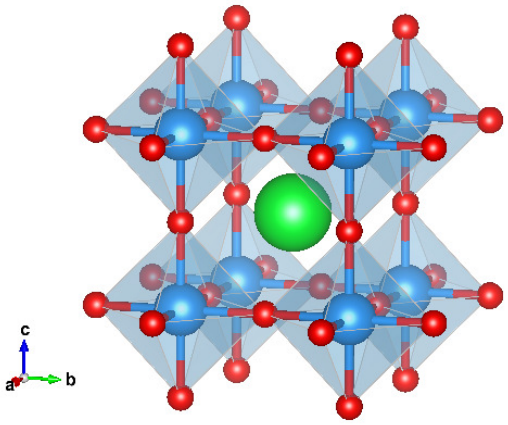

FIG. 2.2: Alternative view for ABO_3.

the initial cubic cell. Some of the ABO_3 compounds with $t > 1$ adopt perovskite-like structures which contain hexagonal stacking faults. The tolerance factor is a critical and useful tool in evaluating cell distortion of perovskite structure.

2.2.1 Complex perovskites

When two cation species occupying the same site in a perovskite differ sufficiently in the charge and/or ionic radius, an ordered arrangement may be observed. Cation order-disorder transitions play a huge role in adjusting the crystal structure, phase stability, and properties of many complex oxide perovskites. Altering the degree of ordering can make substantial changes in magnetic behaviour, dielectric/ferroelectric response, and electronic/ionic conductivity [12]. An ordered arrangement is usually stabilized when two cationic species occupying the same site differ sufficiently in their coordination preference, valence, and/or size. Even though many B-site ordered perovskites have been characterized, the A-site ordering examples are quite rare and often involve vacancies as the alternate cation species. The type of B-site ordering in perovskites are categorized according the crystallographic site stoichiometry of the ordered cells. The

most common examples are 1:1, 1:2, and 1:3 ordering of two different B-site cations. Other stoichiometric ratios are not impossible, however, no examples have been reported so far.

The 1:1 ordered arrangement of B-site cation systems, $A(B'_{1/2}B''_{1/2})O_3$ or $A_2(B'B'')O_6$, are the most frequently encountered family of ordered complex perovksites. Of this so called *double perovskite*, the different cations occupy an alternate B-site in a NaCl-type arrangement. This ordering maximizing the separation of similar ions, where each B′ cation has six B″ cations as nearest B-site neighbour (nBn) and vice versa. With this arrangement the intermediate oxygen anions can satisfy the different bond length requirements of the two cations by moving toward the smaller one. This structure often viewed in terms of an ordered alternation of B′ and B″ cation layers perpendicular to the [111] direction.

Compared to the many example of double perovskites, very few example of 1:2 ordered system of $A(B'_{1/3}B''_{2/3})O_3$ or $A_3(B'B''_2)O_9$ have been reported. The 1:2 layering of B-site cations as $\cdots$B′B″B′B″ $\cdots$ along the [111] direction yield a hexagonal superstructure with $a_{\mathrm{order}} = a_{\mathrm{c}}\sqrt{2}$ and $c_{\mathrm{order}} = a_{\mathrm{c}}\sqrt{3}$ as can be seen in Fig 2.3. The reason for limited occurrence of 1:2 ordering is related to the resultant bonding environment of the oxygen anions. In this system, the different size and charge of the B′/B″ cations are accommodated via a coordinated long-range displacement of the intermediate layer of anions toward the <111> layer containing the smaller and more highly charged B-site ions (typically B″) [43–45]. Because, the anions lying between two B″ layer are overbonded, this arrangement can only form when B″ cations undergo displacement away from the center of their octahedra to lengthen the three B″-O-B″ bonds, and shorten the other three B″-O-B′ bonds and thus reduce the bond valence sum for O^{2-}. This off-center coordination is usually observed only for small highly charged transition metal cations such as Nb^{5+} and Ta^{5+}.

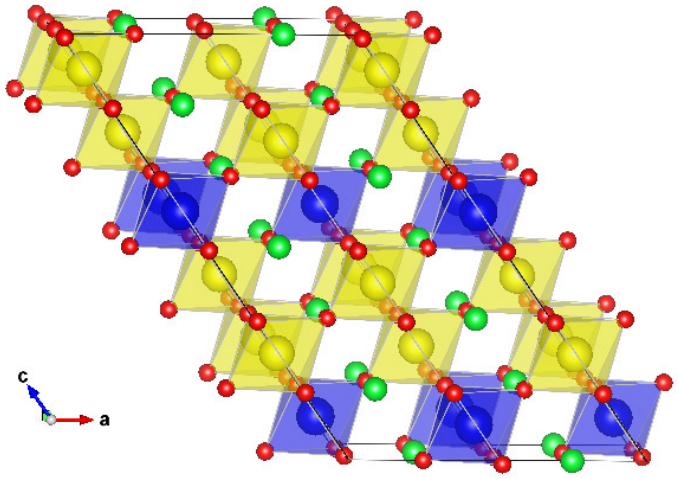

FIG. 2.3: Schematic representation for a 1:2 order system projected along [111] directions. $B'O_6$ octahedra are shown in blue while $B''O_6$ octahedra are in yellow; $A^{2}+$ ions are in green while oxygen ions are in red

After the discovery of 1:1 and 1:2 ordering in perovskites, many attempts were made to stabilize order systems with stoichiometric ratios of 1:3. However, many of these $A(B'_{1/4}B''_{3/4})O_3$ or $A_4(B'B''_3)O_{12}$ systems were reported to be disordered and for quite some time perovskite with hexagonal stacking sequences were believed to be the only examples for which the ordering involved a more complex stoichiometry. However, in recent years, 1:3 layer ordering was identified in metastable polymorph $Ca_4Nb_2O_9$ and in this case the 1:3 layering yields a monoclinic base-center supercell with $a_{\mathrm{order}} = a_{\mathrm{c}}\sqrt{6}$, $b_{\mathrm{order}} = a_{\mathrm{c}}\sqrt{2}$, $c_{\mathrm{order}} = a_{\mathrm{c}}2\sqrt{2}$, $\beta = 125.3^{\circ}$ as can be seen in Fig 2.4.

2.3 NMR Experimental Procedure

Using NMR spectroscopy, we can look for differences between average and local arrangements of B-site cation in the system.

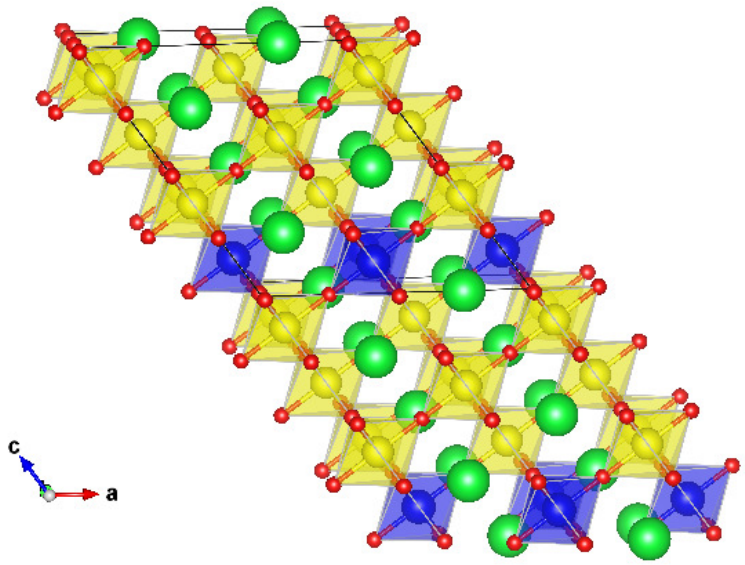

FIG. 2.4: Schematic representation for a 1:3 order system projected along [111] directions. B′O_6 octahedra are shown in blue while B″O_6 octahedra are in yellow; $A^{2}+$ ions are in green while oxygen ions are in red

2.3.1 The samples

NMR measurements were made on five cation-ordered complex perovskite powder samples which can be grouped, as seen in Table 2.1, into two different categories; single A-site and mixed A-site cation systems. The ordering in these systems adopts repeating layers of BO_6 octahedra in the <111> direction of simple cubic perovskite cells. The cation (layered) ordering was characterised by Davies and co-workers [1, 2, 13], using X-ray diffraction and has been refined using Retvield refinement of neutron diffraction. It was also confirmed that more that 99.9$\%$ of the desired phase had been produced. Although the ordering on *B*-site cations was confirmed, no ordering was observed for the *A*-site cations in group **1**. The detail synthesis of these samples can be found in the reference . Table 2.2 gives dielectric properties for these materials.

Group	Chemical Formula	B-site ordering	Space group	Name in this work
1	$(Sr_{2/3}La_{1/3})(Li_{1/3}Ta_{2/3})O_3$	1:2	Monoclinic $P2_1/c$	SLLT
	$(Sr_{2/3}La_{1/3})(Li_{1/3}Nb_{2/3})O_3$	1:2		SLLN
	$(Ca_{2/3}La_{1/3})(Li_{1/3}Nb_{2/3})O_3$	1:2		CLLN
2	$Ca(Li_{1/4}Ta_{3/4})O_3$	1:3	Triclinic $P1$	CLT
	$Ca(Li_{1/4}Nb_{3/4})O_3$	1:2	Monoclinic $P2_1/c$	CLN

TABLE 2.1: List of the microwave ceramics samples studied in this work

Group	Samples	ϵ_R	Q.f (8.7 - 10.2 GHz)	τ_f (ppm/°C)
1	SLLT	25	25,200	-25.1
	SLLN	29	6,300	-75.5
	CLLN	30	26,500	-25.7
2	CLT	27	30,000	
	CLN	37	22,800	

TABLE 2.2: Dielectric properties of microwave ceramics samples. Q.f. stands for quality factor and τ_f is the temperature coefficient of the resonant frequency

2.3.2 ^{7}Li MAS NMR measurement

^{7}Li magic angle spinning (MAS) NMR spectra were collected at ambient temperature at two different magnetic fields, 7.06 T (Larmor frequencies $\nu_0 = 116.57$ MHz) and 17.6 T (Larmor frequency $\nu_0 = 291.46$ MHz), using Bruker AVANCE 300 and Bruker AVANCE 750 spectrometers. All samples were spun at 3, 5, and 10 kHz and the measurements were performed using Bruker 2.5 mm H/X MAS probes. The ^{7}Li data were acquired with single pulse experiments (SPE) with radio frequency (rf) field strength $\nu_1 = 333.33$ kHz, correspond to a π/2 pulse of 0.75 μs. The NMR spectra were externally referenced to 1M LiCl solution in H_2O at 0 ppm. A total of 64-128 transients were acquired with relaxation delay between transient in the range of $25 - 60$ s, which was found to ensure complete recovery between scans.

2.3.3 ^{93}Nb MAS and 3QMAS NMR measurement

^{93}Nb MAS NMR experiments were acquired at ambient temperature at 17.6 T with Larmor frequency $\nu_0 = 183.47$ MHz. The MAS spectra were acquired using Bruker 2.5 mm H/X MAS probe capable of spinning at $\nu_r = 30$ kHz. ^{93}Nb NMR data were acquired using conventional single pulse experiments and non-selective pulse was calibrated on each samples. π/2 pulse duration of $\tau_p = 0.9$ μs ($\nu_1 = 277.78$ kHz) was obtained for all samples. Between 16000 to 32000 transients were acquired and recycle delay of $300 - 500$ ms were found sufficient for complete relaxation in all samples. ^{93}Nb NMR chemical shifts were referenced to a saturated solution of $NbCl_5$ in acetonitrile at 0 ppm. However, for convenience, powdered $LiNbO_3$ (LN) was also used as a secondary reference for which the central peak was set at -988 ppm relative to $NbCl_5$.

In addition to single-quantum measurements, two-dimensional ^{93}Nb triple-quantum (3Q) MAS NMR measurements were acquired to elucidate distinct environments sur-

rounding the niobium nuclei [46]. 2D 3QMAS spectra were obtained by using an amplitude modulated z-filter experiment ($p_1 - t_1$(3Q evolution)$-p_2 - \tau - p_3 - t_2$(acquire)). The optimised pulses lengths for triple quantum excitation (p_1) and reconversion pulses (p_2) were $p_1 = 0.9$ μs and $p_2 = 0.5$ μs, respectively, selective read-out of π/2 (p_3) pulse was set to 20 μs. The 2D 3QMAS measurement required 64 to 128 rotor synchronised t_1 increments of 33.33 μs (corresponding to $\nu_r = 30$ kHz) acquired with 8k transient per t_1 slice, the evolution τ period was set to one rotor period with the recycle delay of 0.3 - 0.5 s. All 2D ^{93}Nb 3QMAS data were Fourier transformed, sheared and referenced in the indirect (F1) dimension according to standard Bruker TOPSPIN algorithms.

2.3.4 MAS ssNMR data processing and simulation

Both ^{7}Li and ^{93}Nb are quadrupolar nuclei, with spin $I = 3/2$ and $I = 9/2$ respectively. Thus, in addition to the Zeeman interaction and induced magnetic field interaction (chemical shift), the nuclei also interact with the local electric field gradient (EFG). To first-order, the spectral features of the satellite transitions are spread over a wide frequency range of the order $\nu_Q = 3C_{\mathrm{Q}}/(2I(2I-1))$ while the shape of the observed patterns reflect the asymmetry parameter η_Q of the interaction. The central transition $\pm 1/2 \leftrightarrow \mp 1/2$ (CT) is not affected by quadrupolar interaction to first-order, while the second-order features are dispersed over a frequency range of the order ν_Q^2/ν_0. In the presence of significant second order quadrupolar interactions, the *center of gravity* (CG) peak position of CT in MAS NMR spectrum is given as the sum of the *isotropic chemical* shift (δ_{iso}) and the *isotropic* second-order *quadrupolar-induced* shift or QIS ($\delta_{\mathrm{iso}}^{\mathrm{QIS}}$) [47]. The CT peak position can then be expressed as

$$\delta^{\mathrm{CG}} = \delta_{\mathrm{iso}} + \delta_{\mathrm{iso}}^{\mathrm{QIS}} \tag{2.2}$$

the *isotropic* second order QIS is given by

$$\delta_{\mathrm{iso}}^{\mathrm{QIS}} = -A_Q + A_Q F(\theta, \phi, \eta) \tag{2.3}$$

where (θ, ϕ) defines the crystallite orientation with respect to external magnetic field. The function *F* depends on the crystallographic orientation and is responsible for the powder pattern line shape. This function averages to zero under MAS. The factor A_Q is defined (in ppm) as

$$A_Q = \frac{3}{40}\frac{C_Q^2}{\nu_L^2}\frac{[I(I+1)-3/4]}{[I(2I-1)]^2}\left(1+\frac{\eta_Q^2}{3}\right)\times 10^6 \tag{2.4}$$

$C_Q = e^2 V_{33} Q/h$ is called quadrupolar coupling constant and is a measure of the strength of interaction between the nuclear quadrupole moment (eQ) and EFG (eV_{33}). The EFG tensor is connected to the local symmetry of the nucleus under study and thus reflects the electronic structure and bonding situation. The symmetry of the environment will be reflected by the asymmetry parameter, η_Q, which is defined by

$$\eta_Q = \frac{V_{11} - V_{22}}{V_{33}}, \tag{2.5}$$

where $|V_{11}| \leq |V_{22}| \leq |V_{33}|$ are the principal axis values of the EFG tensor and from this we have $1 \geq \eta_{\mathrm{Q}} \geq 0$.

All MAS NMR spectra simulations were performed using DMFIT [48] line shape simulation software designed to handle convoluted quadrupolar and/or chemical shift anisotropy (CSA) dominated line shapes. Eight parameters are necessary to completely characterise the local atomic environment and to simulate the NMR spectral line shapes: two for quadrupolar interaction (quadrupolar coupling constant (C_{Q}) and quadrupolar asymmetry parameter (η_{Q})), three for chemical shift interaction (isotropic

chemical shift ($\delta_{\rm iso}$), the CSA (δ_δ) and chemical shift asymmetry parameter (η_δ)) and the three Euler angles (ϕ, χ, ψ) that describe the relative orientation of the EFG and CS tensors. Uncertainties were determined statistically by performing several simulations of each spectrum.

For the chemical shift interaction, the following convention was used,

$$\delta_{\rm iso} = (\delta_{11} + \delta_{22} + \delta_{33})/3 \tag{2.6}$$

while the chemical shift tensor is characterized by the asymmetry

$$\delta_\delta = \delta_{33} - \delta_{\rm iso} \tag{2.7}$$

and the anisotropy

$$\eta_\delta = (\delta_{22} - \delta_{11})/(\delta_{33} - \delta_{\rm iso}) \tag{2.8}$$

$$|\delta_{33} - \delta_{\rm iso}| \geq |\delta_{11} - \delta_{\rm iso}| \geq |\delta_{22} - \delta_{\rm iso}| \tag{2.9}$$

with this definition, we have ($1 \geq \eta_\delta \geq 0$).

2.4 Results and Discussion

All the samples studied have perovskite-like structure where lithium and niobium (or tantalum) atom are octahedrally coordinated by six oxygen atoms in the first coordination sphere. The B-site ordering and presence of BO_6 octahedral tilting in the system, lower the symmetry and modify the parameters of the unit cell of the crystal structure. The average structures, for all samples except CLT, can be described by monoclinic crystal structure with space groups $P2_1/c$ whereas CLT shows triclinic crystal structure

with space group *P*1. The summary for the lattice parameters for the samples is given in table 2.3.

In every crystal structure, there is only a single crystallographic site for lithium and is located at the center of LiO_6 octahedra. Each LiO_6 octahedron is linked to six other NbO_6 (or TaO_6) octahedra units by six bridging oxygen (BO) (refer to Fig. 2.2). The octahedral network for both LiO_6 and NbO_6 (or TaO_6) extend along the *ab* plane (refer to Fig. 2.3 or 2.4). For group **1**, Ca, La, and Sr are distributed over the same crystallographic site and they are located at the interstitial site of these octahedral network. The average structure derived from diffraction data suggests that A-site has mixed occupancy, i.e., the single site is occupied by the two different cations of either La^{3+} and Sr^{2+} or La^{3+} and Ca^{2+} with 1:2 ratio of occupancy probability and an associated formal charge of $+2.33$.

On the local scale, the arrangements of Sr/La or Ca/La may induce local distortion and deviation from the ideal average structure and this will be reflected in the local environment of the individual Li and Nb (or Ta) sites.

Compound	Lattice Parameter					
	a(Å)	*b*(Å)	*c*(Å)	α	β	γ
SLLT	9.811	5.648	17.120	-	125.22°	-
SLLN	9.804	5.653	17.107	-	125.24°	-
CLLN	9.588	5.648	16.630	-	124.90°	-
CLT	9.599	5.472	11.259	89.95°	125.35°	90.55°
CLN	9.680	5.500	17.001	-	125.11°	-

TABLE 2.3: Lattice Parameter for the cation-ordered microwave dielectric samples take from ref [1] and [2]

2.4.1 ^{7}Li MAS NMR spectra

^{7}Li MAS NMR spectra of cation-ordered microwave dielectrics, for both group **1** and group **2**, recorded at 17.6 T is shown in Fig. 2.5 and 2.6 respectively. One strong and sharp peak around -0.2 to -1.8 ppm is observed at the centerband and correspond to central transition (CT). The spectra are also accompanied by a spinning sideband manifold, due to the $\pm 3/2 \leftrightarrow \pm 1/2$ satellite transitions (ST). No *anisotropic* second order quadrupolar broadening was observed for the centerband peak and since the QIS correction is very small (~ 0.004 ppm on 7.06 T), the position of the peak can be taken as the isotropic chemical shift, δ_{iso}. This implies that we can model the spectra with *first order* quadrupolar interaction only.

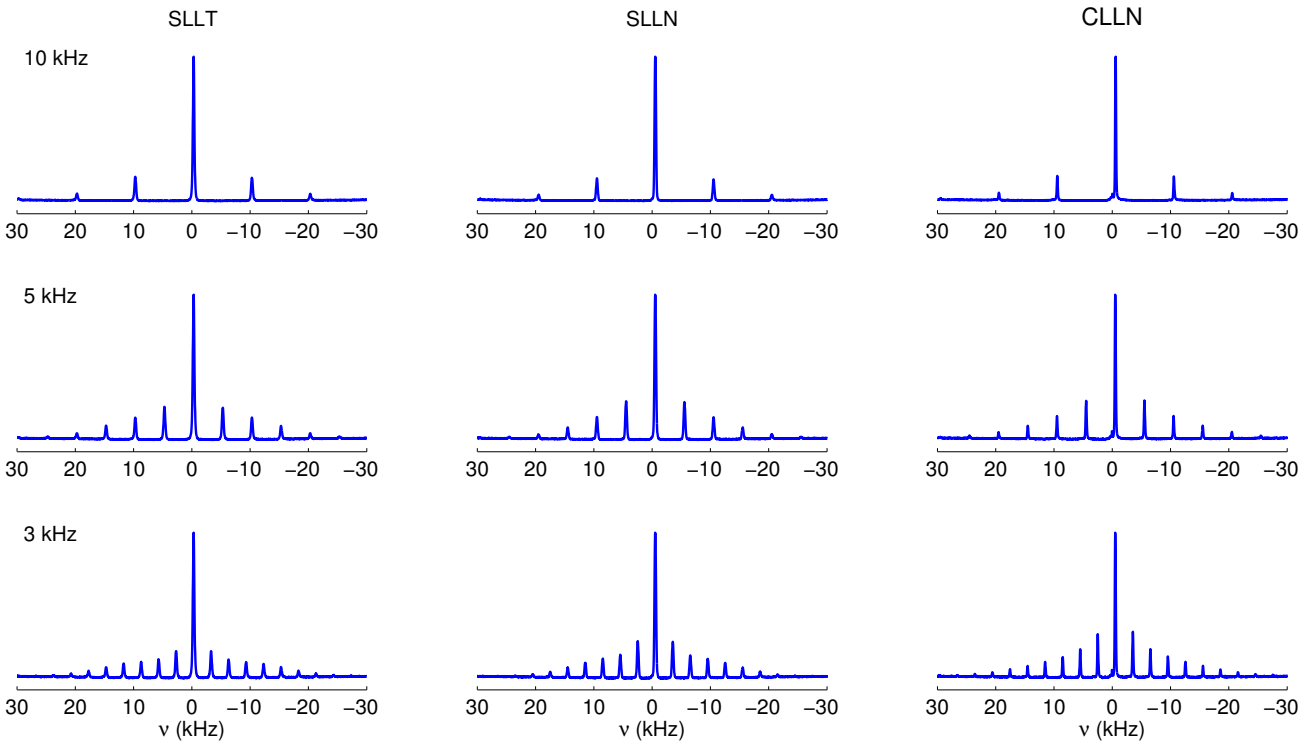

FIG. 2.5: ^{7}Li MAS NMR spectra of group **1** microwave ceramics at 17.6 T rotating at 3, 5, and 10 kHz. All spectra show one strong and sharp central transition as well as spinning sideband manifold resulting from the satellite transition.

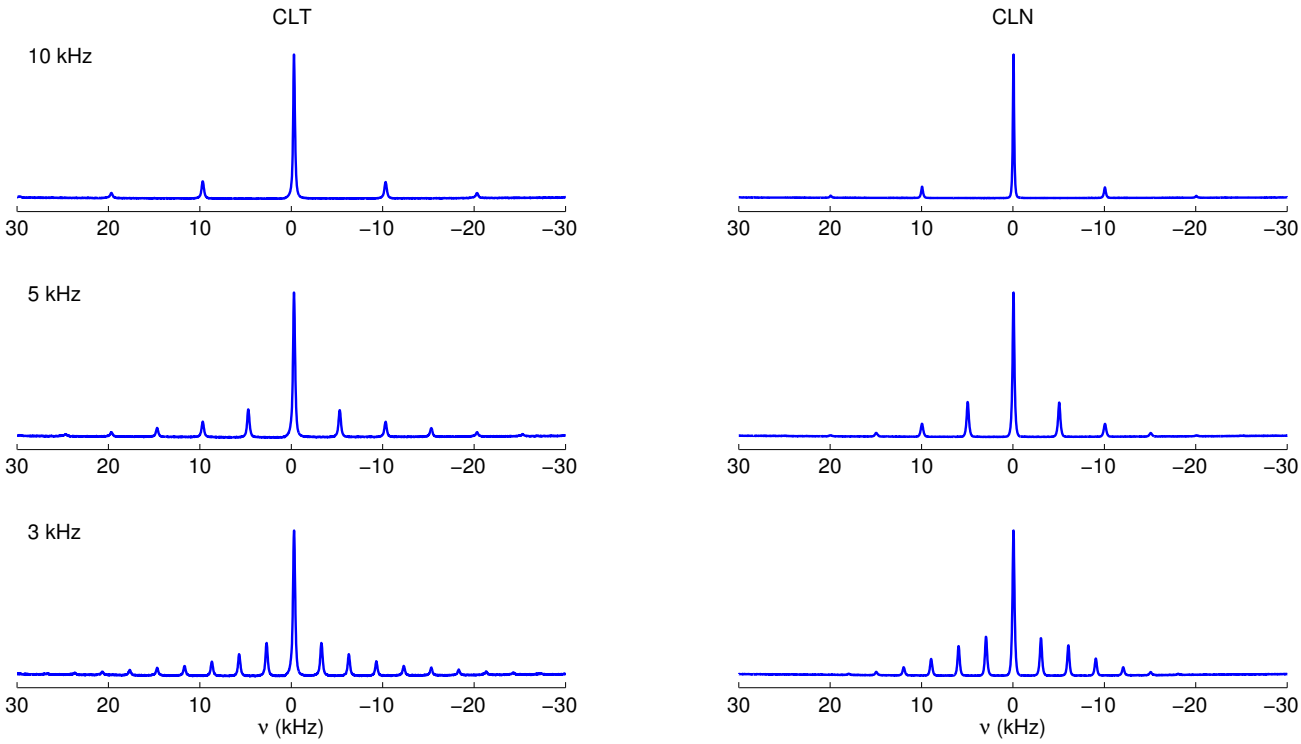

FIG. 2.6: ^{7}Li MAS NMR spectra of group 2 microwave ceramics spun at 3, 5, and 10 kHz.

The ^{7}Li MAS NMR spectra at two field strengths, 7.06 and 17.6 T, confirmed the phase purity of lithium cation ordering, showing only one single resonant component without traces at the downfield regions. In a diamagnetic environment, δ_{iso} of the ^{7}Li were only observed over a narrow range [17] and is the case with our samples. The pseudo-Voigt profile was used to fit the centerband peak and summarized in Table 2.4. The narrow centerbands indicates the samples contain Lithium cations on the highly symmetric and uniform sites. On the other hand, the broader peak of samples observed indicate more distorted or irregularity in the lithium-centered octahedra.

The experimental spectra can be compared to fit models under various assumptions and for this purpose SLLT is taken as an example. The Fig. 2.7 shows (a) the experimental spectrum of SLLT, (b) spectrum of a pure quadrupolar interaction, (c) spectrum for both quadrupolar and chemical shift interaction with coincidence tensor, and (d) the spectrum of both quadrupolar and chemical shift interactions with Euler angles. A detail inspection of Fig 2.7(a) and (b) reveals that the intensities of the spinning side bands in the calculated spectrum are underestimated and do not fit well with the experimental one. Therefore, a perfect agreement with experimental spectrum by only taking into account the quadrupolar interaction is not achieved. Surprisingly, the addition of chemical shift interaction into the calculation didn't improve the model, as can be seen from Fig 2.7(c). This is evidence by the root-mean squared deviation of the simulated spectra relative to the experimental spectrum *R*, which is defined by,

$$R = \sqrt{\sum_{n} \left[Y_{\mathrm{calc}}(n) - Y_{\mathrm{exp}}(n)\right]^{2}} \tag{2.10}$$

were observed not to decrease at all when the shielding anisotropy and asymmetry parameter of the shielding tensor were introduced. To further improve the model, the three Euler angles were introduced (these angles will orient the CSA tensor in the Quadrupo-

lar tensor principal axes) and a significant decrease in R was observed. The corresponding ^{7}Li NMR interaction parameters for all the samples are given in Table 2.5.

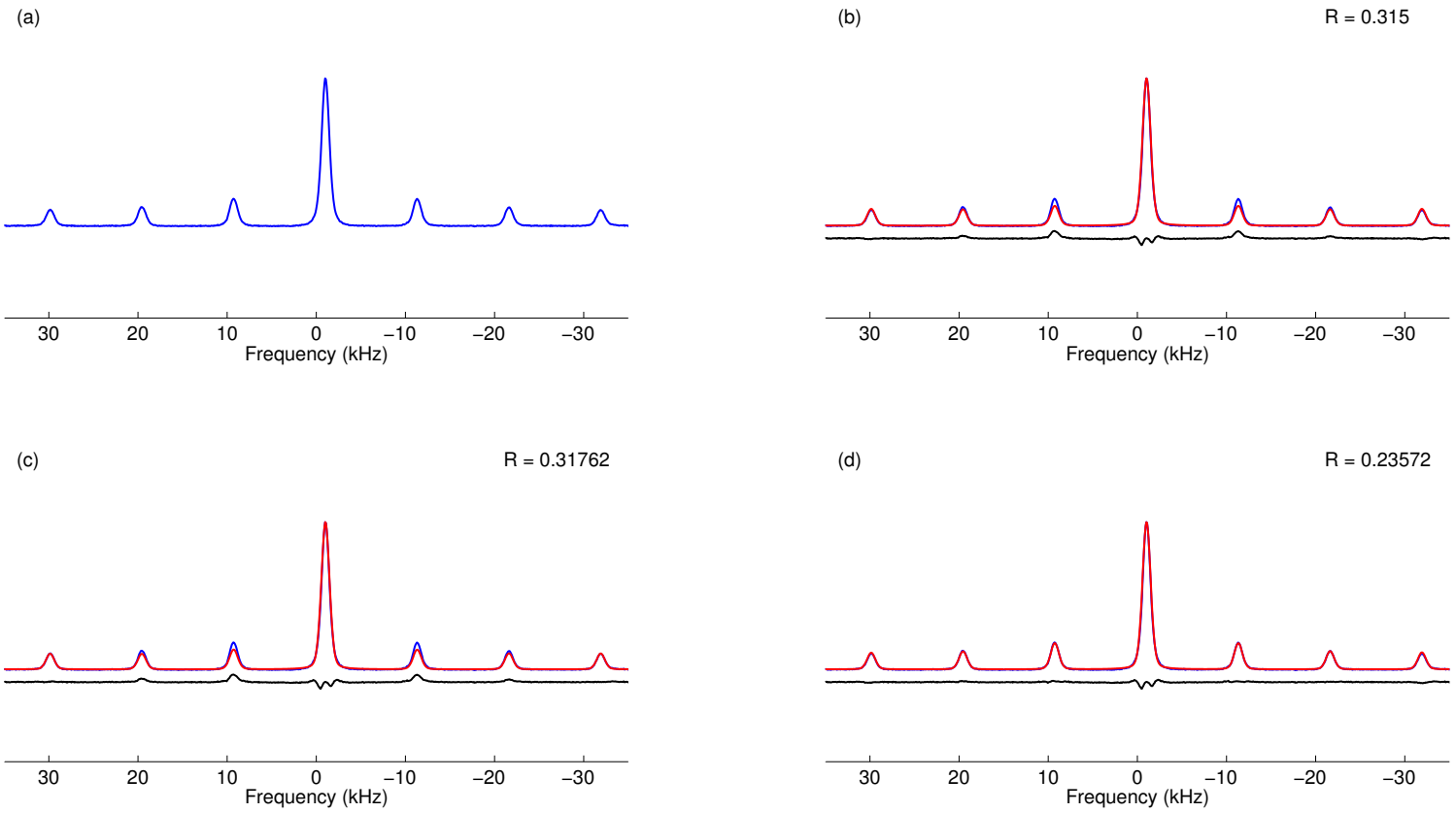

FIG. 2.7: ^{7}Li MAS NMR spectra of SLLT where (a) the experimental data, (b) simulation using quadrupolar interaction only, (c) simulation using quadrupolar and chemical shift interaction with coincident tensors, (d) simulation using the quadrupolar and chemical shift interaction and three Euler angles.

In the case of CLLN, the spectrum shows one additional peak at CT (inset of Fig. 2.8). The second resonance is weaker and the integrated intensity ratio with respect to the strong one is 1:9. It is also broadened by quadrupole interaction with C_Q = 2.6 MHz. This indicates that a second distinct lithium atom environment is present for

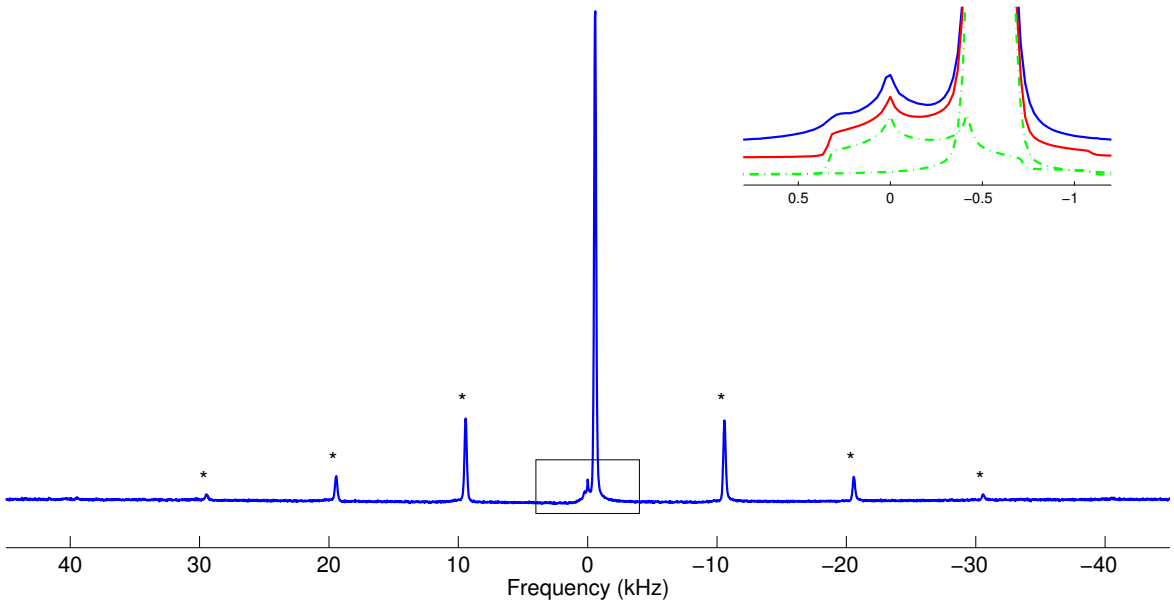

FIG. 2.8: ^{7}Li MAS spectrum of CLLN at 17.6 T rotating at 10 kHz. Inset figure shows two resolvable resonances at the central transition. The simulated spectrum (red) and individual line components (green) are shown below the experimental data.

Samples	δ_{iso}	Linewidth[a](ppm)	x[b]
SLLT	-1.03	1.09	0.77
SLLN	-1.85	1.07	0.98
CLLN	-1.78	0.67	0.62
CLT	-1.05	0.96	0.40
CLN	-0.21	0.91	0.51

[a] Full width at half maximum
[b] Lorentzian component

TABLE 2.4: Psuedo-Voigt profile of the ^{7}Li MAS NMR centerband peak

Sample	$\delta_{\rm iso} \pm 0.05$ (ppm)	$\delta_{\rm CSA} \pm 2$ (ppm)	$\eta_{\rm CSA} \pm 0.02$	$C_{\rm Q} \pm 2$ (kHz)	$\eta_{\rm Q} \pm 0.05$	$\phi \pm 5°$	$\chi \pm 5°$	$\psi \pm 5°$
SLLT	-1.05	-7.2	0.96	45.3	0.61	182	45°	282
SLLN	-1.85	-10.5	0.95	40.7	0.55	234	58°	145
CLLN								
peak 1	-1.80	13.9	0.81	46.0	0.49	-6	46°	17
peak 2	1.45	0	0	(2.6$\pm$0.1) MHz	0.40	0	0°	0
CLT	-1.05	-10.2	0.91	45.4	0.45	183	48°	218
CLN	-0.20	10.6	0.81	29.0	0.55	183	45°	312

TABLE 2.5: ^{7}Li NMR parameters of the microwave ceramics samples

this particular sample. Since we know the ^{7}Li quadrupole moment is very small (-0.04 e·barn), the contribution to this large value must come from a different EFG tensors surrounding this specific lithium atom (lattice property).

2.4.2 ^{93}Nb MAS NMR spectra

Niobium (^{93}Nb) is another nucleus found in the samples that can be probed with solid-state NMR. Thanks to its natural abundance (100$\%$) and its relatively high content in the samples, ^{93}Nb MAS NMR spectra with good signal to noise ration can be obtained within a few hours. Unfortunately, ^{93}Nb has a high nuclear spin ($I = 9/2$) and a large quadrupole moment (-0.32 barn), which complicates the NMR techniques needed to study this particular nucleus. There are only three samples which contain niobium nuclei (SLLN, CLLN, and CLN) and their respective MAS NMR spectra can be seen in Fig. 2.9. Each of these structures has been highly ordered, with niobium in a well-defined environment, and consists of corner-shared LiO_6 and NbO_6 octahedra. The crystal structure predicts one niobium site for 1:2 cation-ordering and two niobium sites for 1:3 cation-ordering.

The whole MAS spectrum for each sample can be seen at Fig. 2.9 which shows partially averaged second-order quadrupolar powder pattern for the CT and an array of

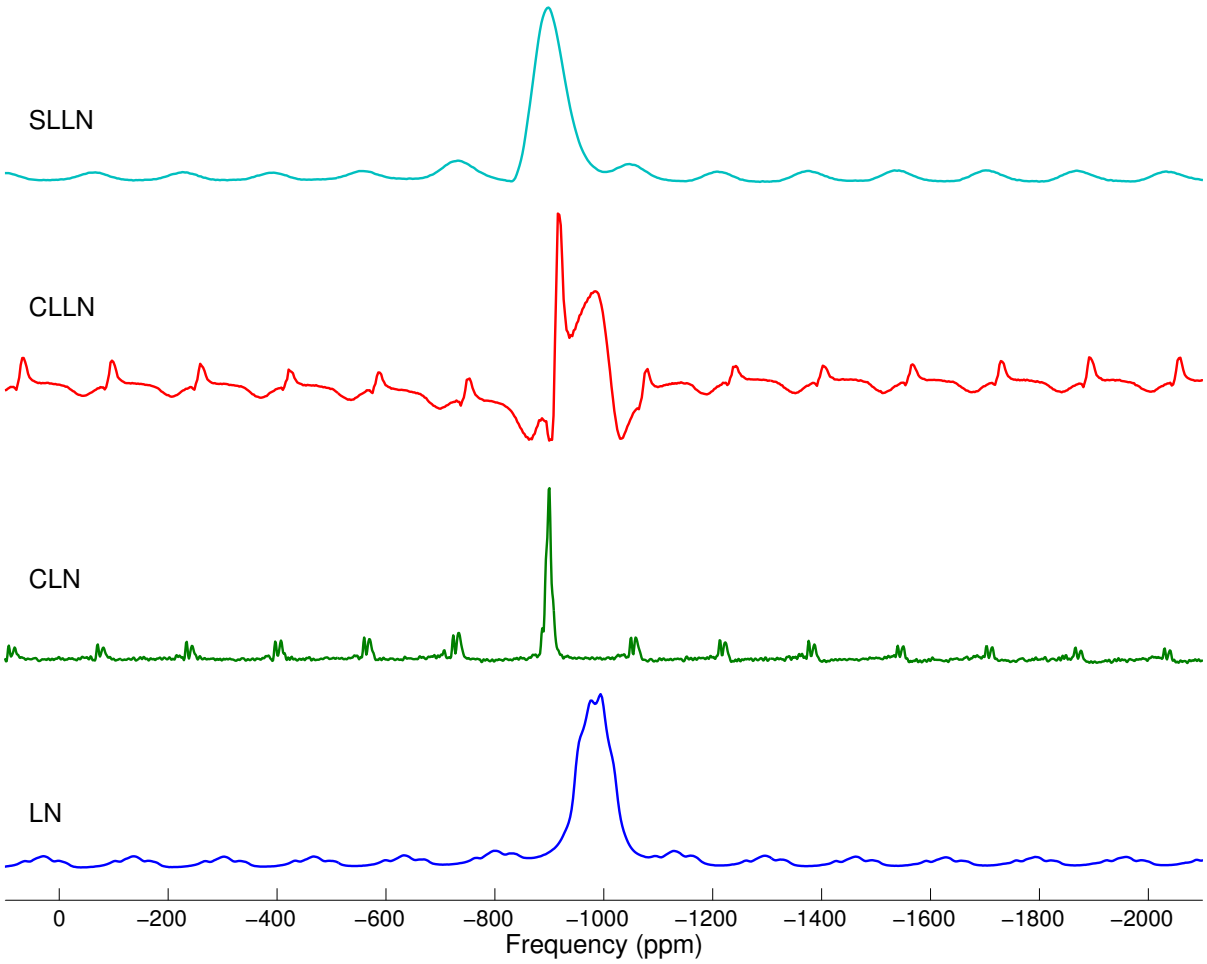

FIG. 2.9: ^{93}Nb MAS NMR spectra of SLLN, CLLN, and CLN spun at 30 kHz. The spectral window is 1 MHz wide.

spinning sidebands due to ST that extend beyond 1 MHz spectral window, indicating very large C_Q values. Measurements using selective irradiation of the central transition were made and the results are shown at Fig 2.10. Interestingly, the ^{93}Nb MAS NMR spectra of SLLN and CLN show only one peak while CLLN show four distinct peaks.

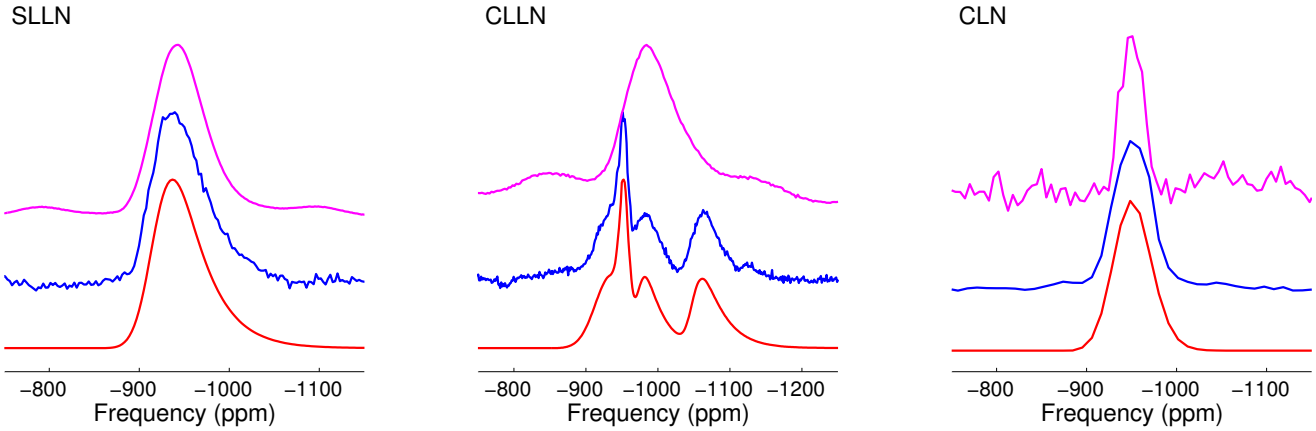

FIG. 2.10: ^{93}Nb MAS NMR selective excitation spectra of SLLN, CLLN, and CLN spun at 30 kHz. The spin-echo (Hahn-echo) experiments are shown in magenta, single pulse excitation experiments are in blue, and simulated spectra are in red.

The spectra also show center band peaks with asymmetric line-shapes, skewed to one side toward the low frequency region. They are also lacking the usual sharp discontinuities typically observed in quadrupolar powder patterns. It has been documented previously [49] that when a MAS NMR central transition resonance shows a tail toward low frequency region and lacks quadrupolar broadening, this indicates the presence of a distribution of both chemical shifts, $\delta_{\rm iso}$, and quadrupole parameters, $C_{\rm Q}$ and $\eta_{\rm Q}$. This distribution may come from structural disorder, such as a distribution of bond angles and bond lengths. The distribution also makes the $C_{\rm Q}$ and $\eta_{\rm Q}$ irresolvable since these quantities are somewhat coupled. Therefore, a detailed study of the line-shapes can be interpreted in terms of structural variations in these materials if one can extract the probability density function for the quadrupolar parameters from the spectra

and compute the EFG tensors for a given structure. Unfortunately, the extraction of the probability density function from NMR spectra of randomly oriented powder samples is not trivial as the distribution in quadrupolar NMR parameters is convoluted with the powder averaging over all possible tensor orientations in the ensemble. Nevertheless, using appropriate simulation tools, many details of this distribution can still be extracted.

A physically sound model for describing the distribution of EFG in disordered and amorphous solids has been developed by Czjzek *et al* [50]. They proposed a joint probability density function

$$P(C_{\mathrm{Q}}, \eta_{\mathrm{Q}}) = \frac{1}{\sqrt{2\pi}\sigma^5} C_{\mathrm{Q}}^4 \eta_{\mathrm{Q}} \left(1 - \frac{\eta_{\mathrm{Q}}^2}{9}\right) \exp\left[-\frac{C_{\mathrm{Q}}^2(1+\eta_{\mathrm{Q}}^2/3)}{2\sigma^2}\right] \tag{2.11}$$

in which the average quadrupolar coupling constant depends on σ alone, the standard deviation of an *isotropic* chemical shift gaussian distribution. As was outlined by d'Espinose de lacaillerie and co-workers [51], the Czjzek distribution can only be used if the number of structural elements contributing to the EFG is sufficiently large, meaning that for a given coordination shell the coordination number should be large. Therefore the Czjzek distribution can, in principle, only be used if the first coordination sphere hardly contributes to the EFG as is the case with our system of octahedrally coordinated niobium sites.

To effectively simulate the spectra to extract quadrupolar information, we need to analyze the contributions of chemical shielding and quadrupolar coupling to the spectrum. As can be seen in Fig. 2.11, the CLLN spectrum at high field show four well resolved peaks with reduced linewidth for each peaks. At lower field, the first three peaks cannot be distinguished very well and are clumped together. This suggests that the spectra are dominated by second-order quadrupolar interactions, since quadrupolar line broadening is proportional to ω_0/ω_Q^2. Therefore, we simulated the spectra by

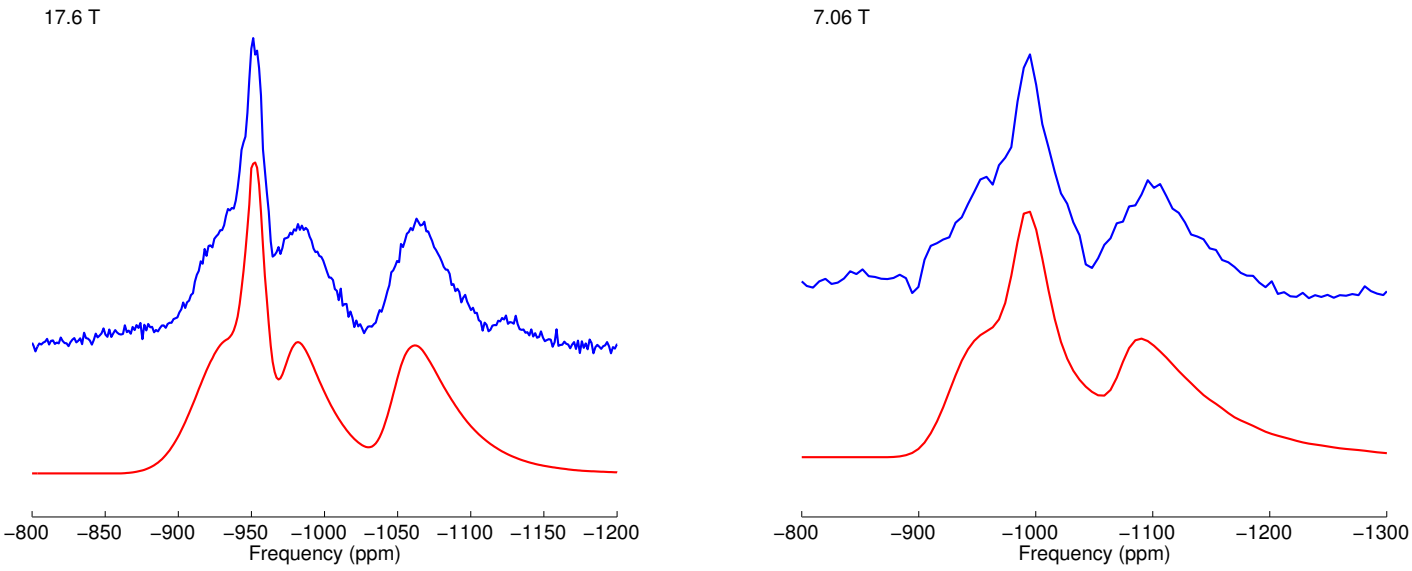

FIG. 2.11: ^{93}Nb MAS NMR selective excitation spectra of CLLN at both magnetic field strength.

neglecting the chemical shielding anisotropy of niobium. in Fig. 2.11, both spectra were simulated considering the distribution of quadrupolar parameters using Czjzek model. The resulting simulations are shown below each spectrum in Fig. 2.10 and 2.11. The quadrupolar parameters using Czjzek model for all samples can be seen in Table 2.5

It is possible to establish relation between ^{93}Nb chemical isotropic shift and the distinct type of octahedral niobate (NbO_6) species. From Fig. 2.10 and Table 2.6, it is clear that the isotropic position for all peaks fall in the range of -900 to -1050 ppm. This suggest that the niobates in all these samples are having non-cubic symmetry and in the vicinity of M^{+n} cations with $n = +1, +2$ and $+3$ [52, 53].

For CLLN, four distinct peaks were observed where the first three peaks can be assigned based on the number of cations occupying the six *next* B-site *neighbour* (nBn) of niobate. Since ^{93}Nb chemical shift of lithium niobate (LN) is at -988 ppm, this suggests that the CLLN peak at -971 ppm has six Nb^{+5} cation in the nBn. It has been reported from numerous study [54, 55] that there exist a systematic up-field of ^{93}Nb chemical

Sample	$\langle\delta_{iso}\rangle \pm 5$ (ppm)	$\sqrt{\langle C_{Q\eta}^2\rangle} \pm 3$ (MHz)	$\Delta\delta_{\mathrm{iso}} \pm 5$ (ppm)
SLLN	-910	26	40
CLLN			
peak 1	-922	18	48
peak 2	-950	7	14
peak 3	-971	23	15
peak 4	-1045	26	28
CLN	-935	16	44
LN	-988	22.25	N/A

where $\langle\delta_{iso}\rangle$ is the istotropic average value, $\sqrt{\langle C_{Q\eta}^2\rangle}$ is the root mean square of quadrupolar product in the Czjzek model.

TABLE 2.6: ^{93}Nb NMR parameters using Czjzek model for the distribution of chemical shifts and quadrupole couplings

shift in the form of $NbO_{6-x}(OB)_x$, where B is the nBn cation. Therefore, we can deduce that the CLLN peak at -950 and -922 ppm are due to the five (and one Li^+) and four Nb^{+5} (and two Li^+) cation in the nBn. Finally, the peak of SLLN and CLN also can be assigned to four Nb^{+5} cation in the nBn.

2.4.3 ^{93}Nb 3QMAS NMR spectra

Fig. 2.12 shows a 3QMAS experiment on SLLN which reveals a single resonance which is broadened along the 'CS' and 'QIS', axes which give the direction of the isotropic chemical shifts and the quadrupole induced shifts, respectively [56]. This broadening supports our finding in 1D ^{93}Nb MAS NMR experiments which suggests that the NMR parameters distribution is present in the system. This distribution can be interpreted as many slight variations of A-site cations and nBn environment surrounding the niobium cations.

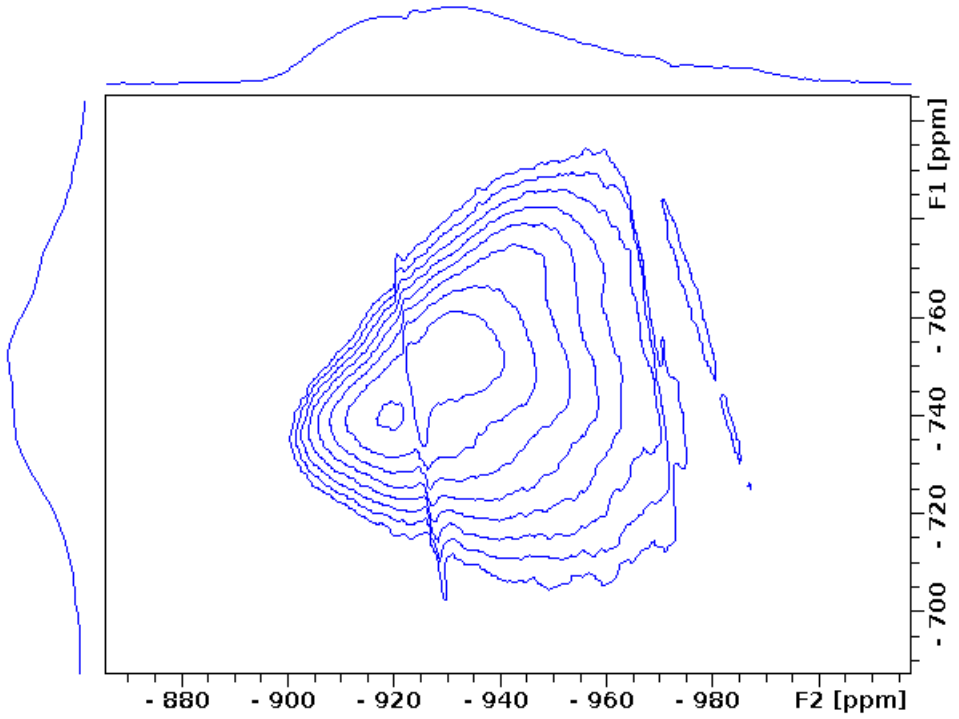

FIG. 2.12: ^{93}Nb 3QMAS NMR spectrum of SLLN which shows one broadened peak along CS and QIS axis.

The 3QMAS experiment for CLLN is shown in Fig. 2.13. This spectrum consists of two clusters site and they are also broadened along the CS and QIS axes. At the lower cluster there are three peaks that are close together which is in agreement with 1D ^{93}Nb MAS NMR spectra. The 3QMAS experiment of CLN (Fig. 2.13) also shows this broadening.

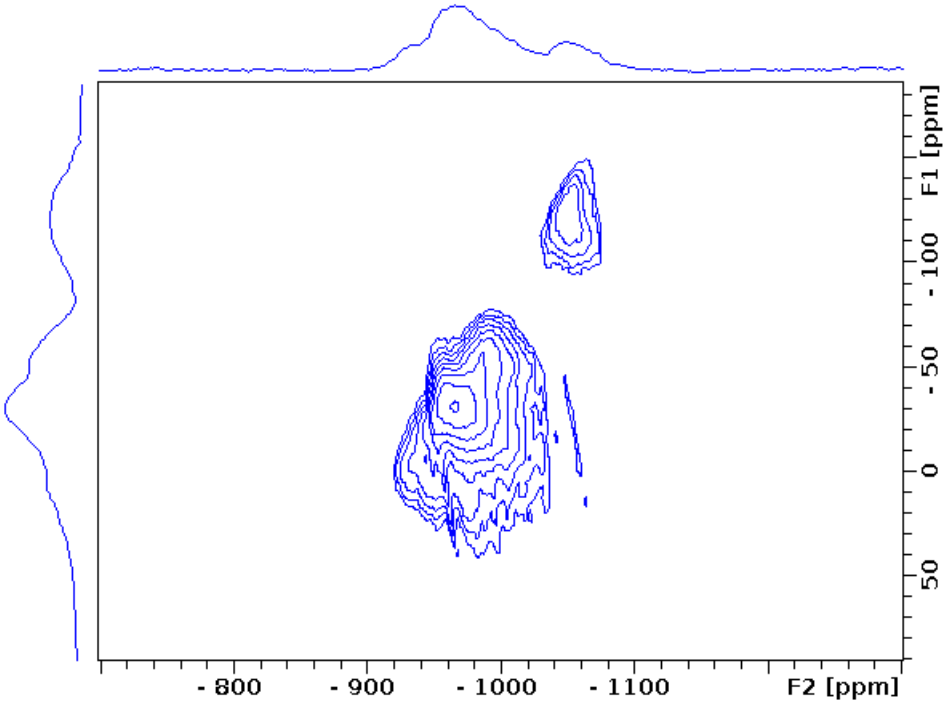

FIG. 2.13: ^{93}Nb 3QMAS NMR spectrum of CLLN which shows two broadened peak along CS and QIS axis.

2.5 Conclusion

^{7}Li and ^{93}Nb MAS NMR experiments have been performed on cation-ordered microwave dielectrics materials at two different magnetic field strengths and varied spinning rates (^{7}Li MAS NMR). In all ^{7}Li NMR measurement only one strong peak (with the exception of CLLN) was observed which confirm that there is only one crystallographic

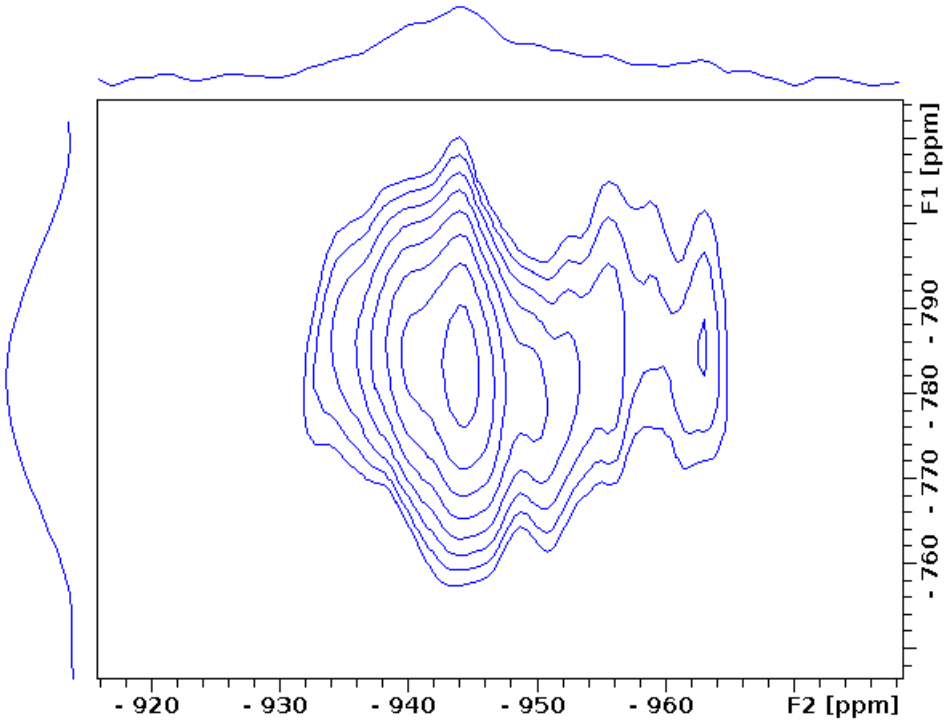

FIG. 2.14: ^{93}Nb 3QMAS NMR spectrum of CLN.

site for Li^+ cations in the system. It's also proved that in order to model the ^{7}Li NMR parameters accurately, spectral simulations with quadrupole and chemical shift interaction along with Euler angles (that bring the CSA tensor into principle axis of quadrupolar tensor) are necessary.

^{93}Nb MAS NMR measurements of niobium-containing samples show spectra with an asymmetric shape and low-frequency tail at the central transition resonance. They also lack the second order quadrupolar pattern which is a trademark of quadrupolar nuclei. This is a clear indication of the presence of NMR parameters (chemical shift and quadrupolar coupling) distribution. Only one resonance peak was observed for all niobium-containing samples, except CLLN which shows 4 peaks. The assignments of these peaks can be explained according to the next B-site neighbours of niobate. It's also established that the first three peaks of CLLN can be assigned to nBn of four, five,

and six NbO_6.

CHAPTER 3

Spin-Lattice Relaxation

Nuclear spin relaxation refers to the mechanism by which nuclear spins in a strong magnetic field arrive at thermal equilibrium, with bulk magnetization parallel to the applied magnetic field. The time scale of this process can vary from micro-seconds to hours, depending on the nature for the interactions between the nuclear spins and randomly time-dependant local magnetic fields. The terms "spin-lattice" and "spin-spin" relaxation, characterized by the relaxation times T_1 and T_2 respectively, are deeply ingrained in NMR literature [18, 20, 57]. T_1 generally refers to the rate at which spin eigenstate populations return to Boltzmann equilibrium following perturbation, while T_2 refers to the (usually much faster) process by which individually processing spin magnetic moments lose phase coherence. It is important to recognize that due to the small nuclear moments, the frequency of resonant photons is far too low to produce significant relaxation by spontaneous emission, which is dominant in other branches of spectroscopy. Instead, measurements of nuclear spin relaxation provide unique information about rapidly fluctuating and random time-dependent local magnetic fields arising from the very same interactions whose time average describe the NMR lineshape.

The "lattice" (an energy reservoir) can be any system with a much larger heat capacity than that of the nuclear spin system. The large heat capacity of the "lattice" ensures that the lattice temperature can be assumed to be constant during the relaxation process. Furthermore, it is assumed that dissipative processes within the lattice destroy any coherences caused by contact with the spin system within a characteristic time τ_c, the correlation time of the lattice. In insulating solids, the physical nature of the "lattice" can be described by ordinary lattice vibrations (phonons), or by two level systems (disorder modes) in amorphous solids at temperatures below 100 K. Adsorbed atoms or molecules in crystals or porous materials can also represent the "lattice" if they have a large heat capacity. In this chapter, definitions and concepts of relaxation will be introduced and explained. We will also introduce the experiment to probe the relaxation mechanism and how it depends on the molecules parameters and molecular motions.

3.1 Introduction to Relaxation

3.1.1 Transition rate in the spin-system and lattice

The total Hamiltonian for the description of spin-lattice relaxation can be described by

$$\hat{H} = \hat{H}_Z + \hat{H}_Q(t) + \hat{H}_L \tag{3.1}$$

where $\hat{H}_Z$ and $\hat{H}_L$ represent the time-independent Hamiltonians for the spin system (Zeeman interaction) and the lattice (reservoir), respectively. $\hat{H}_Q(t)$ denotes the time-dependent coupling between the spin system and the lattice, in this case it is the quadrupolar Hamiltonian. For the eigenfunctions of the combined system, $\hat{H}$, the prod-

uct functions of $|m,r\rangle = |m\rangle\,|r\rangle$, are used, where

$$\hat{H}_Z\,|m\rangle = E_m\,|m\rangle\,, \quad \hat{H}_L\,|r\rangle = E_r\,|r\rangle \tag{3.2}$$

By separating the time-independent part, we can describe the coupling Hamiltonian in the interaction picture as

$$\hat{H}_{Q,i}(t) = \exp\{-\frac{i}{\hbar}(\hat{H}_Z + \hat{H}_L)t\} \cdot \hat{H}_Q(t) \cdot \exp\{\frac{i}{\hbar}(\hat{H}_Z + \hat{H}_L)t\} \tag{3.3}$$

Using Dirac's first-order time-dependent perturbation theory, we can obtain the transition probability, P, between energy levels of $|m,r\rangle \to |m',r'\rangle$ as

$$\langle m',r'|\,P\,|m,r\rangle = \frac{1}{\hbar^2}\left|\int_0^t \langle m',r'|\,\hat{H}_{Q,i}(t')\,|m,r\rangle\,dt'\right|^2 \tag{3.4}$$

Therefore, the rate at which photon is absorbed (emitted) by the lattice to cause a spin-flip in the nuclear system can be obtained by,

$$\langle m',r'|\,W\,|m,r\rangle \equiv W_{mr,m'r'} = \frac{\partial\,\langle m',r'|\,P\,|m,r\rangle}{\partial t} \tag{3.5}$$

If $\hat{H}_Q$ is time-independent, and the lattice states are close enough, we have

$$\langle m'|\,W\,|m\rangle = \frac{2\pi}{\hbar}\left|\langle m'|\,\hat{H}_Q\,|m\rangle\right|^2 \rho(E) \tag{3.6}$$

where $\rho(E)$ represents the energy density of the considered processes in the lattice. In general, for quadrupolar hamiltonian, the transition rate can be obtained from the

following relationship

$$W_{mr,m'r'} = \frac{(2m \pm 1)^2 (I \mp m)(I \pm m + 1)}{(2I)(2I-1)^2} W_1(r,r') \delta_{m',m\pm1} + \frac{(I \mp m)(I \pm m + 1)(I \pm m + 2)}{(2I)(2I-1)^2} W_2(r,r') \delta_{m',m\pm2} \quad (3.7)$$

The $W_n(r,r')$ represents spectral density of the correlation function of the process in the lattice. For more detail derivations, the readers are referred to Appendix A.

3.1.2 Master equation

In order to describe the time-dependence of the magnetization, we can start with the master equation of the population numbers, N_m, at a particular state. The average number of spins populating the Zeeman level m is given by,

$$\frac{dN_m}{dt} = \sum_{n=-I}^{I} W_{nm}(N_n - N_{n0}) - (N_m - N_{m0}) \sum_{n=-I}^{I} W_{nm} \quad (3.8)$$

where N_{n0} and N_{m0} are thermal equilibrium population of level E_n and E_m, respectively. W_{nm} follows from Eq. 3.7 and denotes the transition rate of $n \to m$ in the spin system for all possible transitions in the lattice. The general solution is of the form

$$N_m(t) - N_{m0} = \sum_{k=-I}^{I-1} c_k(t=0) \exp\{-\lambda_k t\} \quad (3.9)$$

Since the total number of spins is a constant, the system has only $2I$ non-vanishing eigenvalues, λ_k. The initial conditions are given by the excitation, (e.g. for 180° pulse on resonance, we will have $N_n(t=0) = -N_{-n}(t=0)$) and as a result, some of the constant c_k will vanish. This equation can lead to a equation describing the motion of

z-magnetization as,

$$\frac{M_z(t) - M_\infty}{M_z(0) - M_\infty} = e^{-t/T_1} \tag{3.10}$$

where M_∞ is the magnetization at equilibrium. In words, this says that the *z*-magnetization from $M_z(0)$ to M_∞ follows and exponential law. Time-constant of exponential $R_1 = -1/T_1$ is called the *longitudinal* or *spin-lattice* relaxation time.

3.2 Relaxation Mechanism

3.2.1 Spin-phonon Coupling in insulating crystals

Relaxation due to a fluctuating EFG caused by lattice vibrations (phonons) involves processes by which the photons, which cause random nuclear spin-flips in the system, are emitted/absorbed by the lattice. The effectiveness of such processes depends on the spin-lattice coupling and the lattice properties. This description has to be expressed in quantum mechanical terms and Van Kranendonk [58] presented the first theoretical approach for these processes. In a later paper, he and Walker [59] introduced a new mechanism, and reviewed the previous literature. In his paper, he described that the EFG tensor can be approximated in symbolic sum as

$$V = V_0 + V_k\epsilon_k + \epsilon_k V_{kl}\epsilon_l + \cdots \tag{3.11}$$

The strains, ϵ_k, are derivatives of the displacements of the nuclei with respect to the coordinates, which can be calculated from the quantized displacement operators given by the lattice Hamiltonian. The components of the EFG in the basis of the strain tensor components depend on the actual lattice structure. We can make crude estimation by

assuming that these components are comparable to the magnitude of the static electric field gradient. The lattice Hamiltonian, which depends on the actual structure as well, is approximated by its harmonic and anharmonic parts. The static part of the quadrupole interaction is neglected. Nevertheless, with the mentioned assumptions and Debye's model of the phonon density, it is possible to find the field and temperature dependence for several terms, and to estimate their magnitudes using Eq. 3.6.

Since the energies for the two possible nuclear spin-flips, $\hbar\omega_0$ or $2\hbar\omega_0$, are very small quantities compared with the lattice, the density of phonons can be approximated as being constant over an energy range of $2\hbar\omega_0$. Therefore, we have $W_1 \approx W_2$. The first term of the expanded EFG is the constant (static) term. The second term is proportional to ϵ_k, and thus involves only one phonon. In this *direct process*, the lattice absorbs (emits) the photon necessary for the nuclear spin-flip. The relaxation rate of for this process (with the approximation $W_{m,m+1} \approx W_{m,m+2} \approx 1/T_1$) can be written in the form

$$\frac{1}{T_1} = C_1 \omega_0^2 T \tag{3.12}$$

where C_1 is a constant and T is absolute temperature. Although the probability for multi-phonon processes in the lattice decreases rapidly with the number of involved phonons, it was also shown [58] that the direct process can be neglected compared with the two-phonon process (called *Raman process*), the third term in the expansion for V, where the photon necessary for the nuclear spin-flip is absorbed (emitted) by a two-phonon process in the lattice. The conservation of energy yields $n\hbar\omega_0 = \hbar\omega_1 + \hbar\omega_2$. The relaxation rate for this process can be written in the form

$$\frac{1}{T_1} \approx C_2 \frac{T^2}{\Theta_D} \tag{3.13}$$

where Θ_D is Debye temperature of the lattice and C_2 is a constant. At lower temperatures, the dependence is more complicated. The so called *low-temperature Raman process* can be written as

$$\frac{1}{T_1} \approx C_2' \frac{T^7}{\Theta_D^6} \tag{3.14}$$

3.3 Experiment detail

The nuclear spin-lattice relaxation (SLR) rate was obtained using saturation recovery experiments. Saturation of the nuclear spins was achieved by radiating the samples with a train of 90° pulse. Immediately after the train of pulses, a free induction decay (whose amplitude is proportional to the z-magnetization just before the pulse) can be observed by applying a read-out 90° pulse. We then wait a time τ so that some magnetization has been re-established, and then apply another 90° read-out pulse to the recovering system. The read-out 90° pulse will rotate any *z*-magnetization into the *xy*-plane, where it will produce FID signal proportional to the recovered magnitude it had just before the read-out pulse. If this pulse is repeated for different values of τ, the amplitude of the FID as a function of τ will give the value of T_1 (Please see Fig. 3.1 and Fig. 3.2)

The number of 90^0-pulse trains used in the saturation recovery experiment was 64, with delay time of 25 μs between pulses. Nuclear magnetization growth along the *z*-direction was measured immediately after saturation of the spin system and the central peak height was fitted to Eq. 3.10. Nuclear SLR time measurements were repeated over a temperature range of $220 - 370$ K. The samples temperatures were maintained constant by blowing cold nitrogen gas pass a heater coil into the sample chamber.

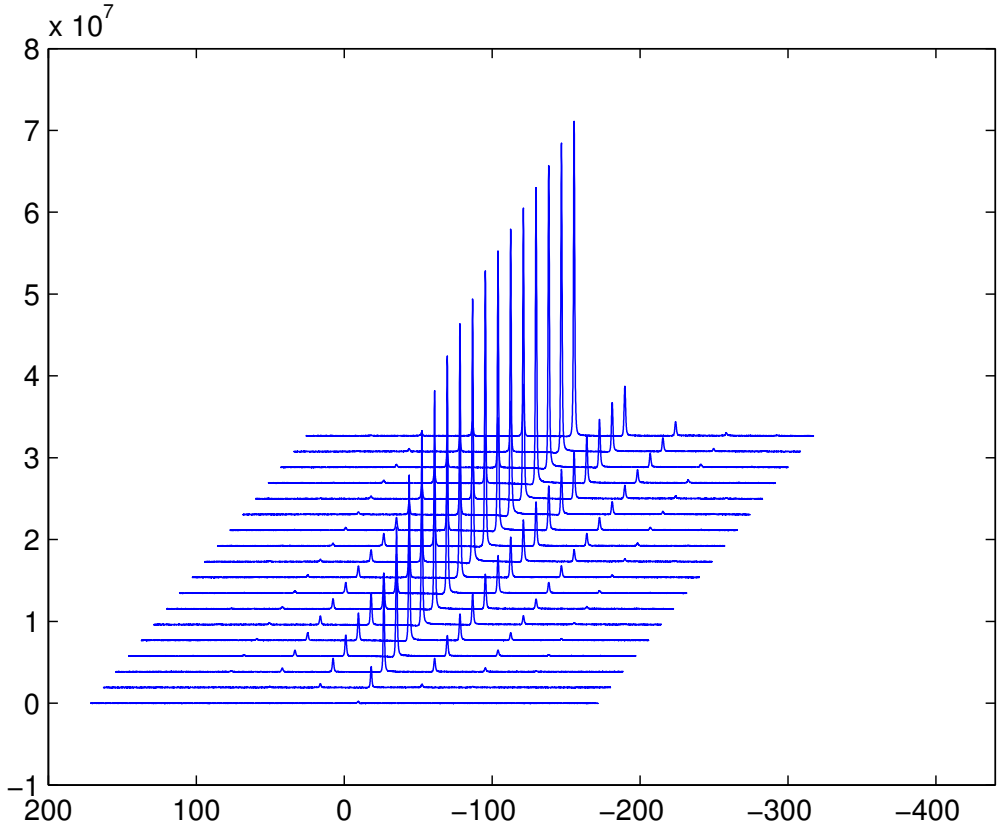

FIG. 3.1: The magnetization growth of one sample at ambient temperature.

3.4 Results and Interpretation for ^{7}Li SLR rate

3.4.1 Temperature dependence

The temperature dependence of ^{7}Li SLR rate, T_1^{-1}, for the central transition is shown in Fig. 3.3 (7.06 T) and in Fig. 3.4 (17.6 T). At both fields, the relaxation rates were found to be proportional to temperature. This is evident from the data that are well represented by the linear relation of $R_1 = \alpha T + \beta$. The linear least-squares fit parameters are listed in table 3.1.

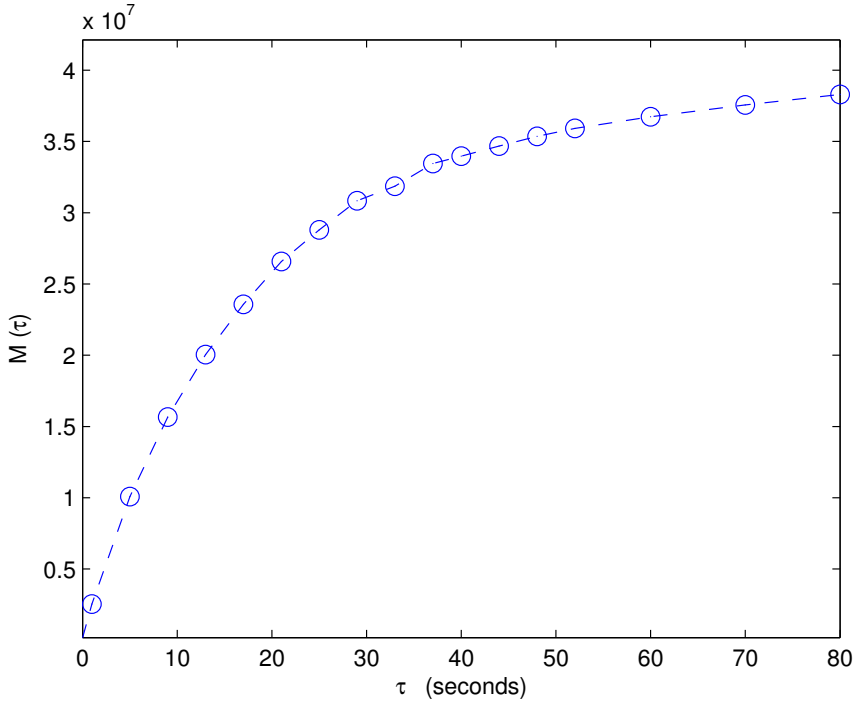

FIG. 3.2: The plot of the central peak intensity with respect to recovery time.

The relaxation rate obtained for group **1** shows several features. First, SLLT and SLLN show a very weak temperature dependence at low and high magnetic field, suggesting there is no significant changes in the dynamics of the system over the temperature range of $220 - 370$ K. Furthermore, it is found that the curves for those two samples at both field are quite similar even though they have different cations at B'-site, namely Ta^{5+} and Nb^{5+}. This indicates that the relaxation mechanism for both samples is independent of the nBn cations. The reason for this may be that both B′-ions have very similar ionic radius (78 pm for Ta^{5+} and 78 pm Nb^{5+} [60]). Second, CLLN showed a more obvious change with respect to temperature, compared to other samples in group **1**. This can be explained by taking into account that CLLN contains calcium cations at A-site rather than strontium. Since calcium cations have smaller ionic radius than

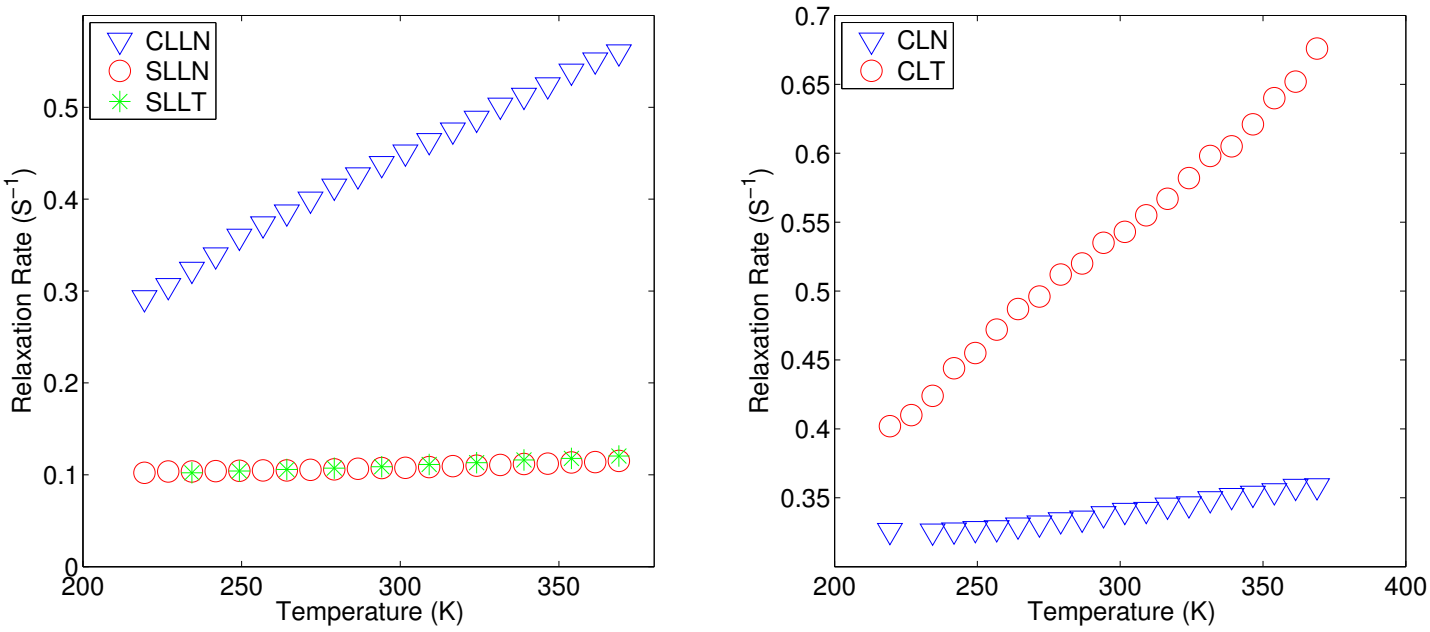

FIG. 3.3: SLR rate of Sample from group **1** (left) and from group **2** (right) at 7.06 T.

strontium (114 pm for Ca^{2+} and 132 pm Sr^{2+}), this provides enough room for the surrounding ions to get more displaced in the system, hence it will result more distorted crystal structure. It is also evident that CLLN has a lower tolerance factor than SLLT and SLLN [1]. This changes cause an increase in the distortion of the cell making it more sensitive to temperature changes, as suggested by the relaxation rate measurements. Furthermore, as can be seen in Fig. 3.3 and Fig. 3.4 ,the lithium cations relax faster in CLLN than in SLLN (or SLLT) do, even though they only differ by the identity of one cation at the A-sites, suggesting that calcium cations play an important role in the relaxation of lithium cations in the samples.

As for group **2**, we notice that the difference in relaxation rates between CLT and CLN are quite obvious, as can be seen from Fig. 3.3 and 3.4. Given the compositions of cations at nBn for these two samples are identical with SLLT and SLLN, the significant

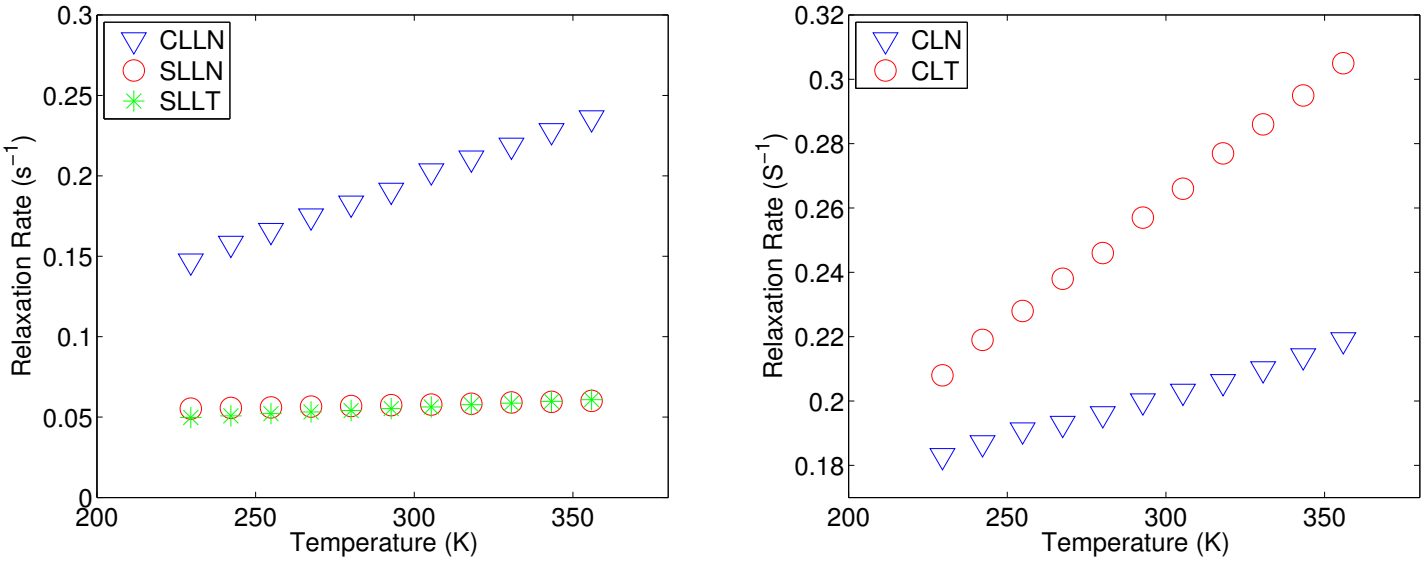

FIG. 3.4: SLR rate of Sample from group **1** (left) and from group **2** (right) at 17.6 T.

change in the relaxation of the system must be strongly influenced by the identity of the ion at A-site, namely Ca^{2+} cations. This also corroborates our hypothesis from previous paragraph that calcium cations strongly influence the relaxation, hence the dynamics, of the system.

Since relaxation rates for all samples increase linearly with temperature, one may be tempted to conclude that the dominant relaxation mechanism for these samples is the single-phonon process (refer to Eq. 3.12). However, we are going to need to prove the field dependence before drawing any such conclusion. Field dependent relaxation measurements are covered in the next sub-section.

3.4.2 Magnetic field dependence

Measurements at both low and high field show that the relaxation rate for all samples decreases with increasing magnetic field ($T_1^{-1} \sim B_0^{-n}$, where n can take any values)

Compound	Linear Fit	
	LF	HF
SLLT	$(1.343\pm0.101)\times10^{-4}$ T + (0.070 ± 0.003)	$(8.797\pm0.204)\times10^{-5}$ T + (0.023 ± 0.001)
SLLN	$(8.176\pm0.646)\times10^{-5}$ T + (0.084 ± 0.002)	$(3.815\pm0.263)\times10^{-5}$ T + (0.046 ± 0.001)
CLLN	$(1.778\pm0.050)\times10^{-3}$ T - (0.088 ± 0.015)	$(7.026\pm 0.171)\times10^{-4}$ T - (0.013 ± 0.005)
CLT	$(1.758\pm0.050)\times10^{-3}$ T + (0.016 ± 0.014)	$(7.638\pm0.111)\times10^{-4}$ T + (0.033 ± 0.003)
CLN	$(2.495\pm0.202)\times10^{-4}$ T + (0.266 ± 0.006)	$(2.721\pm0.147)\times10^{-4}$ T + (0.121 ± 0.004)

TABLE 3.1: Line of Best Fit

as can be seen in Fig. 3.5 and Fig. 3.6. This result is very different to what we expect from the theory of relaxation by spin-phonon coupling in insulating materials. Theory predicts that the relaxation rate is proportional to the square of magnetic field for a direct one phonon process (Eq. 3.12) and field-independent for indirect two phonon (Raman) process (Eq. 3.13). Thus the experiments rule out the dominant contributions from spin-phonon coupling for the systems under study in this thesis. This is not unusual, since relaxation due to spin-phonon coupling has often been found to be too weak to account for experimentally measured relaxation rates, especially at moderate and higher temperatures (as in our case). More effective relaxation mechanisms, such as moving ions/defects, reorientation of polar groups or adsorbed species, and relaxation due to paramagnetic impurities, often mask the relaxation induced by the spin-phonon coupling.

One possible mechanism that fits the criteria for the relaxation rates be proportional with respect to temperature, and also inversely proportional to magnetic field strength, is relaxation due to paramagnetic impurities where the contact of the nuclear spin system with the lattice occurs via localized electronic states, e.g. paramagnetic impurities [57]. This relaxation mechanism is known to be mediated by nuclear spin diffusion that occurs through mutual dipole-dipole induced spin flips between neighboring nuclear spins, resulting in nuclear magnetization transfer from distant nuclear spins to the local-

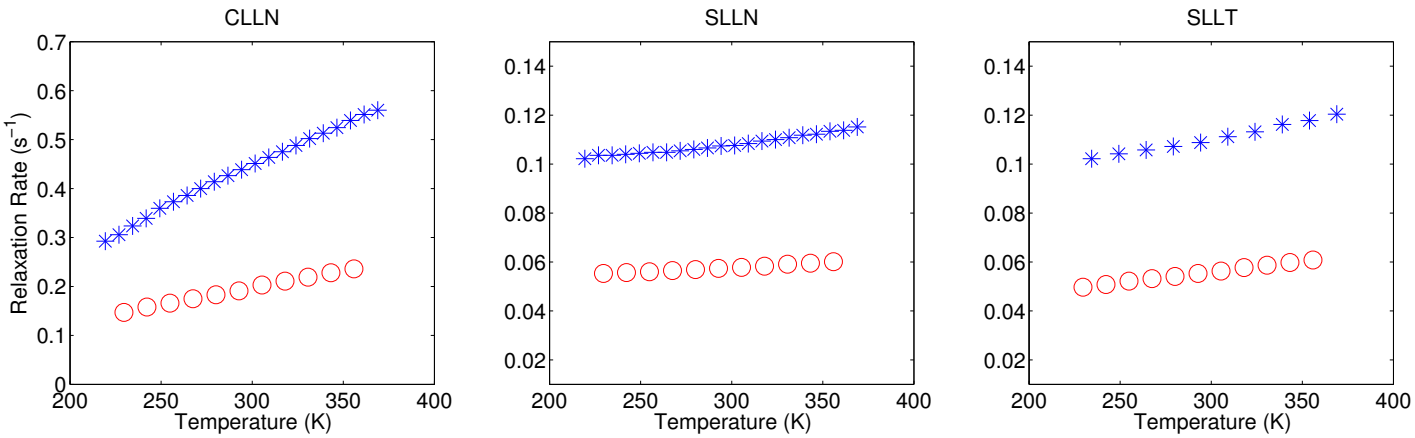

FIG. 3.5: SLR rate of samples for group **1** at both field. Red circles are data taken at 7.06 T while blue crosses are data from 17.6 T.

ized electron spins [61–65]. Readers are encouraged to read Appendix B for a detailed discussion of this mechanism.

To reduce the uncertainty of whether there are paramagnetic impurities or not, electron paramagnetic resonance measurements (EPR) were performed on the samples and the result can be seen in Fig. 3.7. The spectra show main broad signal at $g = 2$ (centered around, $3,500$ Gauss) with different intensity from sample to sample. Obviously, the origin of the broad signal cannot be assigned without additional experiments. Since the identity of paramagnetic species and the concentration of the paramagnetic centers are unknown, the relaxation mechanism due to spin diffusion to paramagnetic centers will be quite hard to be figured out qualitatively and quantitatively.

3.5 Conclusion

Nuclear spin-lattice relaxation rates of ^{7}Li in cation-ordered microwave dielectric samples were investigated using solid-state NMR spectroscopy. Measurements were

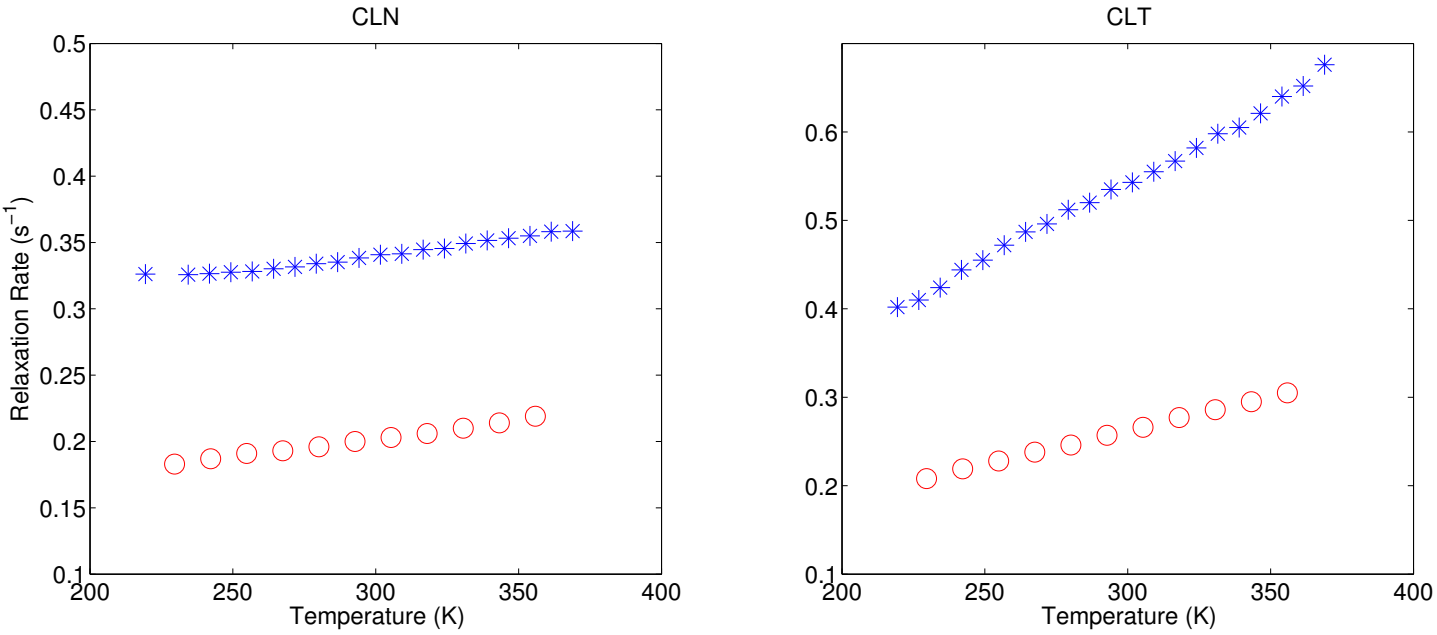

FIG. 3.6: SLR rate of samples for group **2** at both field. Red circles are data taken at 7.06 T while blue crosses are data from 17.6 T.

made at two different magnetic field strengths over the temperature range $220 - 370$ K. Nuclear spin-lattice relaxation rates of the samples were measured using saturation recovery technique with magic angle spinning to increase resolution and sensitivity. The relaxation rates for all samples were observed to increase linearly with increasing temperature. Data obtained at two different magnetic field strength show that the relaxation rates were inversely proportional with respect to magnetic field strength. From these two facts, it's found that the dominant relaxation mechanism in this system must be due to spin-diffusion to paramagnetic impurities. However, more studies to characterize paramagnetic species are crucial to get a more complete understanding of the spin relaxation mechanism.

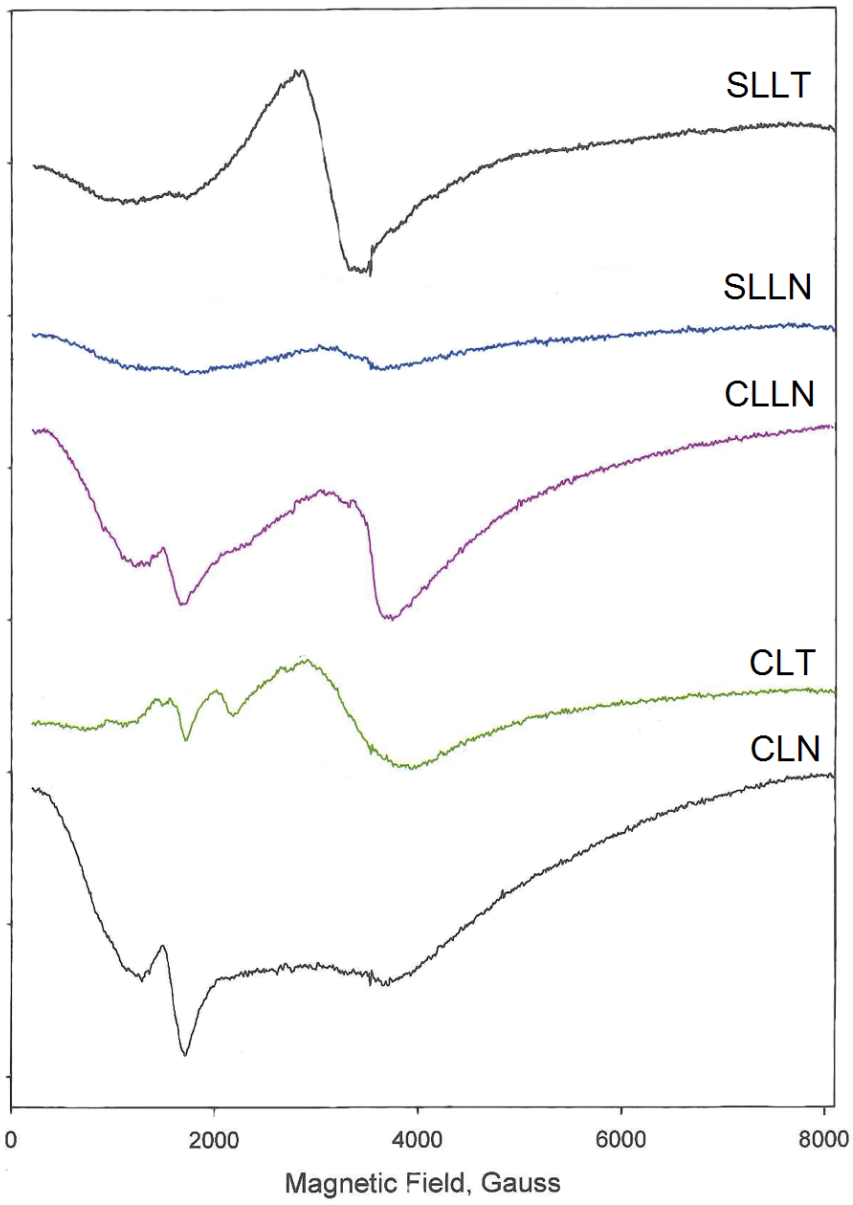

FIG. 3.7: Continuous wave (CW) EPR measurements of the microwave dielectric samples at room temperature.

CHAPTER 4

First Principle Calculation of NMR Parameters

It is generally difficult to convincingly assign observed NMR transition frequencies (and intensities) to specific chemical structures. Historically, these assignments mostly rely on NMR investigations of relatively simple molecular systems whose chemical structure has been determined by other techniques. However, this time-honored procedure is difficult to apply to the perovskites of interest in this thesis because there are no suitable model materials whose detailed molecular architecture is known with precision over the distance scale of a few lattice spacings. Modern computational procedures provide an increasingly powerful approach for addressing this assignment problem. It is now possible to compute NMR quadrupole coupling constants and chemical shifts for realistic model structures with accuracy approaching that of the experimental parameters themselves. Moreover, computations of perovskite phonon band structure, in concert with existing theories of nuclear spin relaxation of quadrupolar nuclei via spin-phonon coupling may offer unique insight into local librational dynamics of disordered

structures [66].

Theoretical calculations provide a useful and alternative approach in assigning spectra. The use of ssNMR and first-principle calculations in a combined approach has previously assisted the study of materials. The calculated values for isotropic chemical shift and quadrupolar parameters can be compared with experimental NMR parameters to help the assignment. This approach relies on testing of several structural models, including models for disorder. This also enables us to study the relations between local structure and NMR parameters.

In this chapter, I will explore the theory behind density functional theory (DFT) and carry out calculations for NMR parameters (chemical shielding and EFG). The calculation uses software based on DFT and takes into account the periodicity of crystalline structure through the implementation of periodic boundary conditions. Chemical shielding tensors were calculated using the gauge including projector augmented wave (GIPAW) [67, 68] implemented in the Quantum Espresso (QE) computer code package [69]. Unlike calculation of the shielding, the calculation of EFG tensors is relatively simple since they depend only on the ground state properties (i.e. ground state charge density and wave function).

4.1 Introduction to Density Functional Theory

According to quantum mechanics, the energy and time-dependent behaviour of collections of particle can be predicted by solving the Schrödinger equation for the system

$$\hat{H}\Psi_i = E_i\Psi_i \tag{4.1}$$

where $\hat{H}$ is the total Hamiltonian operator of the system. Hamilton operator for a system with *M* nuclei and *N* electrons (in the absence of magnetic and electric fields) can be written as [1]

$$\hat{H} = -\frac{1}{2}\sum_{i=1}^{N}\nabla_i^2 - \frac{1}{2}\sum_{A=1}^{M}\frac{1}{M_A}\nabla_A^2 - \sum_{i=1}^{N}\sum_{A=1}^{M}\frac{Z_A}{r_{iA}} + \sum_{i=1}^{N}\sum_{j>i}^{N}\frac{1}{r_{ij}} + \sum_{A=1}^{M}\sum_{B>A}^{M}\frac{Z_A Z_B}{r_{AB}} \tag{4.2}$$

Here *A* and *B* run for *M* nuclei while *i* and *j* denote the *N* electrons in the system. The first two terms describe the kinetic energy of the electrons and the nuclei. The other three terms describe the electron-nuclear attraction, inter-electronic repulsion, and inter-nuclear repulsion respectively.

The first procedure used to simplify the above complicated equation is the Born-Oppenheimer approximation. This approximation is based on the fact that since nuclear mass is far greater than the mass of electron, the nuclei move much more slowly than the electrons. Hence for the first step, we can safely ignore the nuclear kinetic energy or $\left(\hat{T}_n = -\frac{1}{2}\sum_{A=1}^{M}\frac{1}{M_A}\nabla_A^2 = 0\right)$ and the nuclear potential becomes a constant. Also, We can consider the nuclear potential as an *external* potential, V_{ext}, that the electrons feel. The remaining Hamiltonian becomes

$$\hat{H}_e = -\frac{1}{2}\sum_{i=1}^{N}\nabla_i^2 - \sum_{i=1}^{N}\sum_{A=1}^{M}\frac{Z_A}{r_{iA}} + \sum_{i=1}^{N}\sum_{j>i}^{N}\frac{1}{r_{ij}} = \hat{T}_e + \hat{H}_{ne} + \hat{V}_{ee} \tag{4.3}$$

The solution for this electronic Hamiltonian is electronic wave function, Ψ_e, and electronic energy, E_e. The total energy, E_{tot} the sum of E_e and the constant inter-nuclear repulsion term

$$E_{tot} = E_e + E_n \tag{4.4}$$

[1] This expression is using the atomic units

where

$$E_n = \sum_{A=1}^{M} \sum_{B>A}^{M} \frac{Z_A Z_B}{r_{AB}} = \text{constant} \tag{4.5}$$

However, this approximation doesn't remove the difficulties arising from the many-body nature of the interacting electrons. For a system with *N* electrons and nuclear potential V_{ext}, variational principle states that the energy computed from a guessed Ψ is an upper-bound to the true ground state, E_0. Full minimization of the functional $E[\Psi]$ with respect to all allowed *N*-electrons wave functions will give the true ground state Ψ_0 and energy $E[\Psi_0] = E_0$. In other words, the ground state energy is a functional of the number of electrons *N* and the nuclear potential V_{ext}.

Although the conceptual root of DFT may come from Thomas-Fermi model [70, 71], the theorems of Hohenberg-Kohn (HK) [72] are the main factor that makes DFT as one of the most widely used formalism in quantum mechanical calculation. The first HK theorem demonstrates that ground state property of a many-electron system is uniquely determined by an electron density that depend only on three spatial coordinates. Thus the electron density determines *N* and V_{ext}. Now, we can write the total energy as

$$E[\rho] = T_e[\rho] + E_{ee}[\rho] + E_{ne}[\rho] = F_{HK}[\rho] + \int \rho(\vec{r}) V_{ne}(\vec{r}) d\vec{r} \tag{4.6}$$

where

$$F_{HK}[\rho] = T_e[\rho] + E_{ee}[\rho] \tag{4.7}$$

The functional $F_{HK}[\rho]$ is the Holy grail of DFT and if it were known, we would have solved Schrödinger equation exactly. The explicit form of this functional lies completely in the dark and is the major challenge of DFT. Fortunately, we still can make progress in doing the calculation by replacing the real system into an auxiliary one obeying the same Hamiltonian of Eq. 4.6. The approach introduced by Kohn-Sham [73] (KS) replaces

the many-body system into one electron system. The *ansatz* of KS assumes that the ground state density of the original interacting system is equal to some chosen non-interacting system. In other words, KS approach tries to replace Eq. 4.7 into

$$F_{KS}[\rho] = T_s[\rho] + E_{Hartree}[\rho] + E_{XC}[\rho] \tag{4.8}$$

where $E_{Hartree}$ is the classical electrostatic interaction energy of the electrons. This approach can be considered exactly soluble (using computational method) with all the difficulty of many-body terms incorporated into an *exchange-correlation functional*. This term and the corresponding energy expression are the only unknowns in the KS approach to DFT. The KS Schrödinger-like equation can be described as

$$(\hat{H}_{KS} - \epsilon_i)\phi_i(r) = 0 \tag{4.9}$$

where ϵ_i is the eigenvalue and $\hat{H}_{KS}$ is the effective KS Hamiltonian defined as

$$\hat{H}_{KS}(\vec{r}) = -\frac{1}{2}\nabla^2 + V_{KS}(\vec{r}) \tag{4.10}$$

and

$$V_{KS}(\vec{r}) = V_{ext}(\vec{r}) + \frac{\delta E_{Hartree}}{\delta n(\vec{r})} + \frac{\delta E_{XC}}{\delta n(\vec{r})} \tag{4.11}$$

The electron density is obtained from the set of non-interacting one-electron orbitals $\phi_i(r)$ and described as

$$\rho(r) = \sum_{occ} \|\phi_i(r)\|^2 \tag{4.12}$$

4.1.1 Exchange-correlation functional

Local density approximation

One of the simplest exchange-correlation functional is local density approximation (LDA) and it forms the basis of most approximate exchange-correlation functional. At the heart of this model is the idea of a *uniform electron gas*. This is a system in which electrons move on a positive background charge distribution such that the total ensemble is neutral. The central idea of LDA is the assumption that we can write E_{XC} in the following form.

$$E_{XC}^{LDA}[\rho] = \int \rho(\vec{r})\epsilon_{XC}(\rho(\vec{r}))d\vec{r} \tag{4.13}$$

where $\epsilon_{XC}(\rho(\vec{r}))$ is the exchange-correlation energy per particle of an uniform electron gas of density $\rho(\vec{r})$ and the energy per particle is weighted with probability of $\rho(\vec{r})$. The $\epsilon_{XC}(\rho(\vec{r}))$ can be further split into exchange and correlation distributions,

$$\epsilon_{XC}(\rho(\vec{r})) = \epsilon_X(\rho(\vec{r})) + \epsilon_C(\rho(\vec{r})) \tag{4.14}$$

The exchange part, ϵ_X, which represents the exchange energy of an electron in a uniform electron gas of a particular density, was originally developed by Bloch and Dirac in the late 1920's

$$\epsilon_X = -\frac{3}{4}\left(\frac{3\rho(\vec{r})}{\pi}\right)^{1/3} \tag{4.15}$$

Unfortunately, no explicit expression is known for the correlation part, E_C. However, highly accurate numerical quantum Monte-Carlo simulations of the homogeneous electron gas are available [74].

Generalized gradient approximation

The first step beyond LDA is to use the gradient of the charge density, $\nabla\rho(\vec{r})$, in addition to the electron density, $\rho(\vec{r})$, at a particular point. This is done primarily to account for any non-homogeneity of the true electron density. Thus, the exchange-correlation is termed *generalized gradient appoximation*. The exchange-correlation energy for this approximation can be described as,

$$E_{XC}^{GGA}[\rho_\alpha, \rho_\beta] = \int f(\rho_\alpha, \rho_\beta, \nabla\rho_\alpha, \nabla\rho_\beta)d\vec{r} \tag{4.16}$$

A lot of important progress has been made in deriving succesful GGA approximation in which researchers have been employed sum rules, general scaling properties, etc.

4.1.2 Plane-wave pseudopotential DFT formalism

For numerical implementation, it is necessary to expand the KS orbitals using a set of basis functions. Blöch's theorem provides a very nice solution for calculation in solids employing the periodic boundary condition and crystal symmetries. In this theorem, the electron orbitals can be expressed in term of plane wave basis set as,

$$\phi_j(r) = \sum_k \exp(-ikr)u_{j,k}(r) \tag{4.17}$$

where the summation runs over the reciprocal vectors *k*, which often to be chosen as equidistant mesh in the first Brillouin zone defined by the crystallographic unit cell. $u_{j,k}(r)$ are periodic functions with respect to the real space lattice vectors. These func-

tions can also be expanded in terms of plane waves as

$$u_{j,k}(r) = \sum_{G} c_{j,k}(G) \exp(-iGr) \tag{4.18}$$

where **G** is the reciprocal lattice vector. The choice of this expansion has several advantages, such as simplicity, efficiency, and independence from atomic positions (in contrast to localized orbitals basis sets). In term of numerical calculation, the approach also has another advantage in which implementation of calculation of matrix-vectors products through fast Fourier transform can be done easily using parallel computation. The quality of this basis set is adjusted through a *single* parameter known as cut-off (kinetic) energy, E_{cut}, limiting the summation in Eq. 4.18 to wavelengths fulfilling the condition

$$\frac{|k + G_{max}|^2}{2} < E_{cut} \tag{4.19}$$

Even with this cut-off energy, such calculations are still computationally expensive since the basis set wavefunctions are required to be orthogonal with respect to each other. This means there will be a lot of nodes for valence electron wavefunctions and calculation using plane-wave basis set will be very inefficient. The pseudopotential method aims at a drastic reduction of the number of electrons by keeping only the *valence* electron while freezing (eliminating) the *core* electrons. The core-valence interactions are replaced by an effective potential, namely the pseudopotential, so that the Schrödinger equation contains a modified effective potential term instead of the Coulomb potential term for all-electron or full potential. The valence electrons are described by pseudo-wavefunctions with significantly fewer nodes (i.e. smooth) and greatly reduces the number of plane waves in the expansion of Eq. 4.19. A pseudopotential is generated in an atomic calculation and then used to compute properties

of valence electrons in molecules and solids, since the core states remain almost unchanged. This approach treats the valence electrons as moving in background of ionic core. Furthermore, the fact that pseudopotentials are not unique allows the freedom to choose forms that simplify the calculations and the interpretation of the resulting electronic structure.

The most popular form of pseudopotential follows the Martin-Troullier[75] recipe in the Kleinman-Bylander[76] form and is known as norm-conserving pseudopotential (NCPP). However, a pseudopotential known as ultra-soft pseudopotential (USPP), which use a generalised formalism is becoming more common. This form introduced by Vanderbilt[77] and allows an increase of the core region radius without loss of accuracy. Hence, the use of a *reliable* pseudopotential is crucial in DFT calculations.

4.2 Computation of NMR parameters

The calculation of EFG, in principle, is straightforward since it is a direct function of the ground state. The EFG components, $V_{\alpha\beta}(r)$, can be calculated from the charge density as

$$V_{\alpha\beta}(r) = \int dr' \frac{\rho(r')}{|r - r'|} \left\{ \delta_{\alpha\beta} - 3 \frac{(r_\alpha - r'_\alpha)(r_\beta - r'_\beta)}{|r - r'|^2} \right\} \tag{4.20}$$

Eq. 4.20 highlights the fact that the EFG tensor depends upon the charge density close to the nucleus. As the *pseudo*-valence density has a non-phyiscal form in the core region one has to reconstruct the true density, i.e. *all-electron*, in that region. This is the purpose of the projector augmented wave (PAW) reconstruction method [78–80]. It introduces a linear transformation that uses predefined functions (i.e. projectors) to reconstruct the true all-electron wavefunction in the core region using the pseudo-wavefunction. Once the ground state charge density has been determined (i.e.

converged) the EFG calculation is very short.

The magnetic shielding tensor is defined through the response of the system to an external uniform magnetic field as in Eq. 1.27. From [67], the determination of $\mathbf{B}_{ind}$ proceeds through the calculation of the first-order induced current density $\mathbf{J}^{(1)}$ which can be found to be

$$\begin{aligned}\mathbf{J}^{(1)}(r) &= -\sum_{j}^{occ}(\phi_j^{(0)}(r)\nabla\phi_j^{(1)}(r) + \phi_j^{(1)}(r)\nabla\phi_j^{(0)}(r)) - \frac{1}{c}\rho_0(r)\mathbf{A}(r) \\ &= \mathbf{J}_p^{(1)}(r) + \mathbf{J}_d^{(1)}(r)\end{aligned} \tag{4.21}$$

The summation runs over the occupied states and $\rho_0(r)$ is the unperturbed charge density. $\phi_j^{(0)}(r)$ are the unperturbed KS orbitals and $\phi_j^{(1)}(r)$ are their first-order perturbed orbitals due to external magnetic field. The latter make the determination of shielding tensor much more demanding than EFG tensor. $\mathbf{A}(r)$ is the vector potential connected to $\mathbf{B}_0$ through

$$\mathbf{A}(r) = \frac{1}{2}\mathbf{B}_0 \times (\vec{r} - \vec{r_0}) \tag{4.22}$$

where r_0 is the so-called gauge origin. $\mathbf{B}_{ind}$ is finally obtained from the Biot-Savart law described as,

$$\mathbf{B}_{ind} = \frac{1}{c}\int dr' \mathbf{J}^{(1)}(r) \times \frac{\vec{r} - \vec{r_0}}{|\vec{r} - \vec{r_0}|^3} \tag{4.23}$$

To solve the gauge origin problem, Mauri and Pickard [67], combining with PAW approach, devised a theoretical basis for computing all-electron responses to magnetic field. They introduced projectors fulfilling the theoretical requirement of gauge invariance. This led to the gauge invariant projector augmented wave (GIPAW)

4.3 Computational Details

Electronic structure calculations of the NMR parameters were carried out using Quantum Espresso (QE) computer code package [69], employing periodic DFT and the GIPAW method [67] which allows the reconstruction of the all-electron wave function in the presence of magnetic field. The generalized gradient approximation (GGA) and PBE functional [81] were used, and core-valence interaction were described by ultrasoft pseudopotentials [68]. A planewave energy cutoff of 50-70 Ry was employed, and integrals over the Brillouin zone were performed using Monkhorst-Pack *k*-point spacing. The checking and testing calculations were converged as far as possible with respect to both cut off kinetic energy and *k*-point spacing and the optimized values were used for the samples calculation. The structural parameters (unit cell size and shape, and all atomic positions) for all compounds were obtained from literature diffraction studies and kept constant. Hence, no geometry optimization of the crystal structures was performed. In order to calculate NMR parameters, all ions are relaxed from their average positions. This work was performed [in part] using computing facilities at the College of William and Mary which were provided by contributions from the National Science Foundation, the Commonwealth of Virginia Equipment Trust Fund and the Office of Naval Research.

4.4 Preliminary Test

Using the tensors as provided by the calculations, namely the EFG and shielding tensors, we can determine NMR parameter values. Unfortunately, there are many different conventions and the choice is up to the end user. However, there are only two important parameters that need to be supplied by end-user for converting the outputs

into experimental values, i.e. shielding to chemical shift parameters and EFG tensor to quarupolar parameters.

While it is straightforward calculation for calculating quadrupolar parameters, it is not the case for the absolute isotropic shielding tensor which was define in Eq. 1.33. This value can be approximated by Eq. 1.34 giving the isotropic chemical shift. Several methods have been described to calculate $\sigma_{\mathrm{iso}}(ref)$. The first is by directly calculating a single reference compound with known and trusted NMR shift values. The second approch is by fitting the calculated values for a set of studied systems to the experimental values using Eq. 1.34. In this thesis, I will use the latter where it has become the standard practice.

4.4.1 Niobium Test Calculation

In order to provide a solid ground to test the method as well as a way to fit chemical isotropic values, five niobium-containing systems were calculated using QE package. The studied compounds were $LiNbO_3$, $YNbO_4$, $NbBO_4$, $LaNbO_4$, and La_2KNbO_6. The calculation will be compared against the reported values from literature. These results can be seen in Table 4.1. A Quadrupolar coupling constant, C_{Q}, of ^{93}Nb where calculated by multiplying quadrupole moment (*Q*) of -0.32 mBarn to V_{ZZ} obtained from DFT calculation. The IUPAC recommendation is to use external saturated solution of $NbCl_5$ as a primary ^{93}Nb chemical shift reference standard. However, $\sigma_{\mathrm{iso}}^{\mathrm{ref}}$ for this standard is not known with sufficient accuracy. Hence, a slightly modified version of Eq. 1.34, was used to related the calculated σ values with chemical shift δ as has been suggested by Truflandier *et. al.* [82]

$$\delta = a(\sigma_{\mathrm{iso}}^{\mathrm{ref}} - \sigma) \tag{4.24}$$

In Eq. 4.24 both a and $\sigma_{\mathrm{iso}}^{\mathrm{ref}}$ were evaluated from a linear regression between the

computed $\sigma_{\rm iso}$ and experimental $\delta_{\rm iso}$. A value of $\sigma_{\rm iso}^{\rm ref} = -1147.8$ was determined from the linear regression analysis as shown in Fig. 4.1

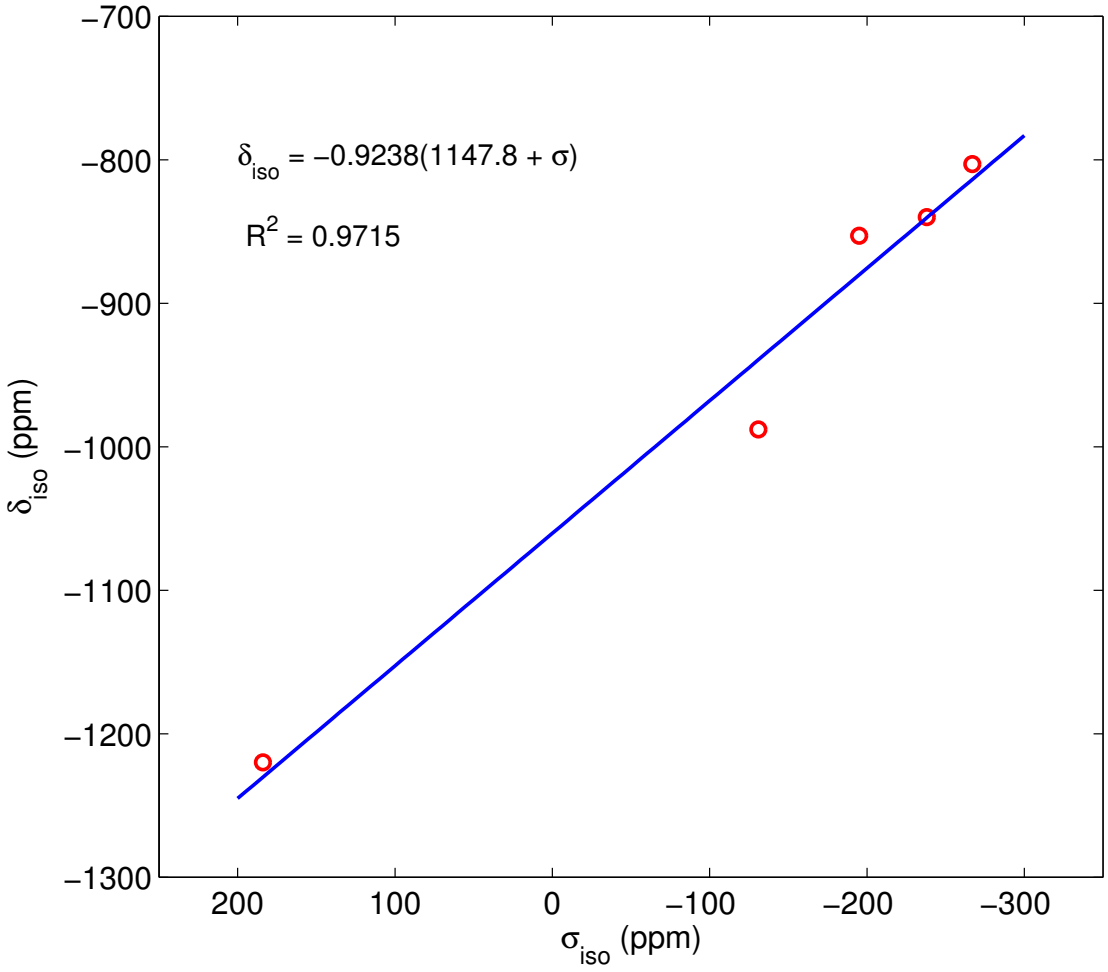

FIG. 4.1: Correlation between QE calculated isotropic values of ^{93}Nb chemical shielding tensor, $\sigma_{\rm iso}$, and experimental ^{93}Nb chemical shifts, $\delta_{\rm iso}$.

Sample	δ_{iso}(ppm)	Δ_δ (ppm)	η_δ	C_Q (MHz)	η_Q
$YNbO_4$ (Four-coordinated)					
DFT pbe	-839	-185	0.47	77.6	0.44
DFT pbesol	-840	-190	0.50	80.9	0.39
Expt[83]	-840	-179	0.430	82.33	0.38
$LaNbO_4$ (Four-coordinated)					
DFT pbe	-880	-237	0.57	81.3	0.2
Expt[83]	-853	-238	0.56	86.55	0.19
La_2KNbO_6 (Five-coordinated)					
DFT pbe	-813	-690	0.03	67.8	0.05
Expt[53]	-803	-640	0.02	71.43	0.07
$LiNbO_3$ (Six-coordinated)					
DFT pbe	-929	123	0.002	27.3	0.00038
DFT pbesol	-939	113	0.002	22.5	0.00034
Expt[83]	-988	115	0	22.25	0
$NbBO_4$ (Eight-coordinated)					
DFT pbe	-1237	236	0.0011	7.3	0.0074
DFT pbesol	-1230	232	0.0007	10.2	0.0013
DFT other[53]	-1220	219	0	8.8	0

TABLE 4.1: ^{93}Nb NMR parameters calculation for niobium containing systems.

4.5 Results and Discussion

4.5.1 Group 1 vs Group 2

As discussed in Chapter 2, the mixed occupancy of A-site between Ca/La and Sr/La become the source of disorder in the system for group **1**. In this thesis, we are going to focus our attention to group **2** (single A-site system) before trying any attempts to describe the system of group **1** (mixed A-site system). The reason for this is because group **2** presents a much simpler system than group **1** does in terms of atomic configurations. Once we have the full understanding in describing this system, we can use the knowledge to tackle more complex system such as group **1**.

4.5.2 CLT Calculation

The DFT calculation of CLT with 1:3 layer ordering was performed on a super-cell with 40 atoms. The system is comprised of 2 lithium atoms, 6 tantalum atoms, 8 calcium atoms, and 24 oxygen atoms as shown in Fig. 4.2. During the calculation, the lattice parameters were kept constant while the atomic positions were fully relaxed. The pseudo-potential files were obtained from THEOS website, while the generation files for these pseudo-potentials were handled and distributed through the PSLibrary project [84]. For calcium atoms, 3s, 4s and 3p valence orbitals were used; for oxygen atoms, 2s and 2p orbitals were considered as valence states; for lithium atoms, 1s and 2s valence states were used; and for tantalum atoms, valence states of 5s, 5p, 6s and 5d were used. Several convergence tests for *k*-point spacing, cut-off energy, and cut-off density were performed. The final calculations used k-point spacing of $4 \times 6 \times 3$, kinetic energy cut-off of 60 Ry, and density cut-off of 550 Ry.

Since no ^{181}Ta NMR measurement was performed, the result of the calculation can

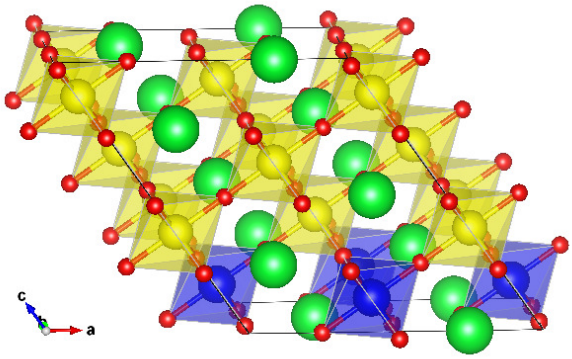

FIG. 4.2: 40 atoms unit cell for CLT calculation. Li^{+} octahedra are shown in blue, Ta^{5+} octahedra are in yellow; $Ca^{2}+$ ions are in cyan while oxygen ions are in red.

only be compared to ^{7}Li NMR measurements. In addition, the calculated value of σ_{iso} for the lithium cannot be reported since no prior calibration of $\sigma_{\mathrm{iso}}^{\mathrm{ref}}$ was made for this system. The calculation result can be seen in Table 4.2.

Sample	δ_{iso} (ppm)	Δ_{δ} (ppm)	η_{δ}	C_Q (kHz)	η_Q
CLT					
Li calc	$-$	1.3	0	132	0.15
Li meas'd	-1.05	-10.15	0.91	45.4	0.45

TABLE 4.2: Calculated NMR parameter values of CLT

As can be seen from the table, the predicted values for both NMR chemical shielding and quadrupolar parameters does not match with the values obtained from experiments. The table shows the value of C_{Q} which is off by a factor of three. The reason for this is due to the fact that the real value of C_{Q} for ^{7}Li is very small (around 50 kHz). Furthermore, as can be seen from niobium test result, the predicted C_{Q} values from the the calculation gave a deviation as small as 2 MHz from the experimental ones. Taking this into account, it was realized that achieving a calculation result within a reasonable accuracy for lithium NMR parameters in this system is not possible. However, by tak-

ing into account the noise of the calculation result, it can be argued that the lithium quadropolar coupling predicted by the calculation is quite remarkable seeing how close it is compared with the experimental values.

4.5.3 CLN Calculation

There is a little confusion for CLN structure where two layered ordering compositions were found from two different experiments [13]. Initial studies suggested that the CLN system exhibits (non-stoichiometric) 1:2 ordering [1] while subsequent investigation demonstrated a layered 1:3 ordering of Li and Nb [2]. For the sake of completenes, in this thesis, investigations for both possibilities were performed.

1:3 Layer ordering

The CLN 1:3 layer ordering lattice parameters were found to be very similar with the CLT [2]. Hence, only a few adjustment for the input file were necessary (for example, replacing tantalum atoms with the niobium). The unit cell used for the calculation is the same with Fig. 4.2. In addition, for the calculation, the values of *k*-point grid, energy and density cut-off were kept the same. After relaxing the atoms, the NMR parameter calculations were performed and the result can be seen in Table 4.3.

For lithium NMR parameters, the calculations give the same result as for CLT. That is, the quadrupolar parameters were off by a factor of three. Again, this is likely due to the value of C_{Q} for lithium. As for niobium prediction, the calculations gave a very close result with the experimental values. The measured C_{Q} (using Czjzek model) gave a value of 16.1 MHz while the calculation gave result of 17.7 and 26.7 MHz.

Sample	δ_{iso} (ppm)	Δ_δ (ppm)	η_δ	C_Q (MHz)	η_Q
CLN					
Li calc'd	$-$	1.6	0.34	88 kHz	0.07
Li meas'd	-0.21	16	0.81	29 kHz	0.55
Nb1 calc'd	-870	79	0.34	17.7 MHz	0.57
Nb2 calc'd	-880	156	0.71	26.7 MHz	0.21
Nb meas'd	-935	44	N/A	16.1 MHz	N/A

TABLE 4.3: Calculated NMR parameter values of CLN

1:2 Layer ordering

The electronic structure calculation of CLN with 1:2 layer ordering of Li^+/Nb^{5+} cations was also performed. Since this layer ordering is non-stoichiometric, a random-site model layer configuration was devised. In this model the structure consist of one mixed layer and two pure layers while maintaining the overall charge neutrality of the system. The occupancies used in the model assumed that the $B''_{2/3}$ positions were exclusively of Nb atoms (pure layer) and the $B'_{1/3}$ position contained a random distribution of lithium and niobium atoms (mixed layer). In the mixed layers, the ratio for Li^+ to Nb^{5+} is 3:1 as in the form of $(Li_{3/4}Nb_{1/4})$. Using this assumption, the chemical formula can be re-written as $Ca((Li_{3/4}Nb_{1/4})_{1/3}Nb_{2/3})O_3$.

To accommodate all of these assumptions, one super-cell with 120 atoms was constructed. This super-cell contains 6 lithium atoms, 18 niobium atoms, 24 calcium atoms, and 72 oxygen atoms. In this super-cell, there are two mixed Li^+/Nb^{5+} layers where in each layer there are **three** Li^+ cations and **one** Nb^{5+} cation. Using permutation of Nb^{5+} position in each mixed layer, a total of **16** configurations of crystal structure was obtained. One configuration, $\alpha 1$, can be seen in figure 4.3.

The naming of the crystal structure configurations will be based on the position of Nb^{5+} cation in the first and second mixed layer. A greek letter was used to mark

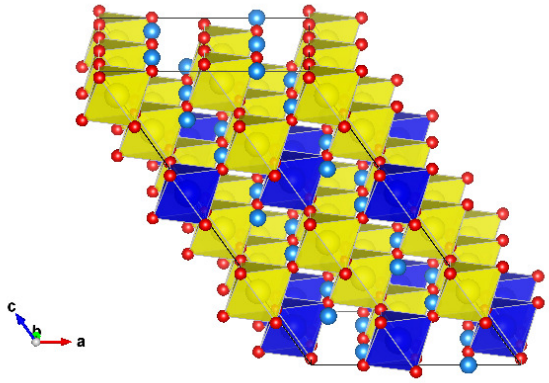

FIG. 4.3: Super-cell for 1:2 layer ordering of CLN with 120 atoms. There are two layers of mixed Li^{+}/Nb^{5+} cations. Li^{+} octahedra are shown in blue, Nb^{5+} octahedra are in yellow; $Ca^{2}+$ ions are in cyan while oxygen ions are in red.

the position of niobium in the first layer while using number for the second one. The top-view schematic representations for each layer can be seen in figure 4.4 and 4.5. Therefore, $\alpha 1$ configuration will have niobium positioned at point α in the first layer and point '1' in the second layer. Based on these configurations and mirror symmetry, it's clear that there are only four unique configurations need to be considered, and they are $\alpha 1$, $\alpha 2$, $\beta 2$, and $\alpha 4$.

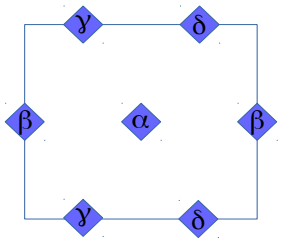

FIG. 4.4: 1^{st} mixed layer of CLN

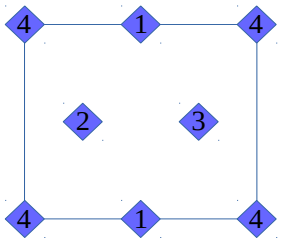

FIG. 4.5: 2^{nd} mixed layer of CLN

Calculation and Result

The total ground state energy calculation for all crystal configurations can be seen in Table 4.4. From the previous section, using mirror symmetry, it is argued that there

are only four unique configurations present in the system. However, with the help of ground state energy calculation, it seems there may only be three different possible configurations for this system (since the energy different between $\alpha 2$ and $\beta 2$ is only 0.2 meV). This assumption can be corroborated by analyzing the atoms in the nearest neighbour. Both $\alpha 2$ and $\beta 2$ configurations, show an identical nearest neighbour atoms such as seen in Table. 4.5 and Table 4.6 (I chose Nb(7) as an example). Therefore, we only need to relax the atomic positions of $\alpha 1$, $\alpha 2$, and $\alpha 4$ configurations for the purpose of calculating the NMR parameters.

Configuration	E_{tot} (meV)
$\alpha 1$	387.6
$\alpha 2$	128.5
$\beta 2$	128.7
$\alpha 4$	0

TABLE 4.4: The ground state total energy for all CLN configurations. The energy at $\alpha 4$ was taken as 0 meV

Once atomic position relaxation calculations are carried out, the NMR parameter calculations can be performed. The results for all three unique configurations are tabulated in the following Tables. In Table 4.9, the isotropic chemical shift of $\alpha 4$ configuration falls in the range of $2 - 400$ ppm while the C_{Q} is between 160 - 360 MHz. In (solid) niobium oxide compounds, this set of values is un-physical [52, 53, 83]. Therefore, $\alpha 4$ configuration is ruled out as a possible solution for 1:2 layer ordering of CLN.

To give more detailed information on the distribution of the quadrupolar parameters and to correlate with local structure features, the plot of isotropic chemical shift, δ_{iso}, with respect the quadrupolar coupling, C_{Q}, can be used and Fig. 4.6 shows the correlation

Bond	Lengths (Å)
Nb(7) - O(96)	2.00
Nb(7) - O(120)	2.00
Nb(7) - O(76)	2.00
Nb(7) - O(99)	2.00
Nb(7) - O(70)	2.00
Nb(7) - O(52)	2.00
Nb(7) - Ca(48)	3.46
Nb(7) - Ca(26)	3.46
Nb(7) - Ca(45)	3.47
Nb(7) - Ca(46)	3.47
Nb(7) - Ca(27)	3.47
Nb(7) - Ca(28)	3.47
Nb(7) - Ca(32)	3.48
Nb(7) - Ca(42)	3.48
Nb(7) - Nb(23)	4.00
Nb(7) - Nb(24)	4.00

TABLE 4.5: The Nearest neighbour atoms of Nb(7) for CLN.

Bond	angle
O(96) - Nb(7) - O(120)	90.00°
O(96) - Nb(7) - O(76)	179.99°
O(96) - Nb(7) - O(99)	90.00°
O(120) - Nb(7) - O(76)	90.00°
O(120) - Nb(7) - O(99)	179.99°
O(76) - Nb(7) - O(99)	89.99°

TABLE 4.6: Bond angles of Nb(7) for CLN.

Configuration	δ_{iso}(ppm)	Δ_δ (ppm)	η_δ	C_Q (MHz)	η_Q
Li1	–	-3.53	0.679	0.086	0.9361
Li2	–	-3.53	0.679	0.086	0.9361
Li3	–	-1.13	0	0.084	0.1733
Nb4	-987.2	142	0.923	50.5	0.0928
Nb5	-800.0	-284	0.372	15.0	0.9893
Nb6	-861.1	-185	0.060	141	0.0442
Nb7	-886.7	138	0.977	93.4	0.7762
Nb8	-886.7	138	0.977	93.4	0.7762
Nb9	-878.0	-235	0.464	31.9	0.9375
Nb10	-878.0	-235	0.464	31.9	0.9375
Nb11	-927.3	190	0.372	56.6	0.3200
Nb12	-877.9	-97.4	0.606	118	0.1562

TABLE 4.7: Calculated NMR parameters of $\alpha 1$

between these two parameters. Even though the figure shows a scattered-data, it can be argued that there may be, at least, two niobium sites predicted by the calculations. If this assumption is true, the site at lower chemical shifts is characterized by relatively broad C_{Q} distribution, while the site at higher chemical shifts is characterized by a narrower C_{Q} range. However, this assumption should be taken as an overstatement to a complex problem. Therefore we cannot draw a direct comparison to the experimental results. It is important to note that the number of atoms in the unit cell cannot really capture the disorder of the nBn atom of niobium in the mixed layer. Since the unit cell will always be repeated, ideally a huge number of atoms are necessary for complete understanding of a disordered system.

Atom	δ_{iso}(ppm)	Δ_δ (ppm)	η_δ	C_Q (MHz)	η_Q
Li1	–	2.48	0.799	0.082	0.0319
Li2	–	-3.98	0.011	0.075	0.7451
Li3	–	2.8	0.903	0.050	0.9124
Li4	–	-3.99	0.011	0.075	0.7446
Li5	–	2.48	0.798	0.082	0.0318
Li6	–	2.8	0.903	0.050	0.9122
Nb7	-982.2	211	0.377	67.3	0.1600
Nb8	-982.0	211	0.377	67.3	0.1599
Nb9	-855.1	152	0.803	47.7	0.6541
Nb10	-857.1	-188	0.946	86.5	0.9478
Nb11	-890.8	-211	0.358	48.0	0.7784
Nb12	-886.5	-466	0.574	80.7	0.1424
Nb13	-856.9	-188	0.944	86.5	0.9476
Nb14	-854.9	152	0.803	47.4	0.6542
Nb15	-886.3	-466	0.574	81.0	0.1423
Nb16	-890.7	-211	0.358	48.0	0.7792
Nb17	-856.9	-188	0.944	86.5	0.9476
Nb18	-854.9	152	0.803	47.4	0.6542
Nb19	-886.3	-466	0.574	80.7	0.1423
Nb20	-890.7	-211	0.358	48.0	0.7792
Nb21	-855.1	152	0.803	47.4	0.6541
Nb22	-857.1	-188	0.946	86.5	0.9478
Nb23	-890.8	-211	0.358	48.0	0.7788
Nb24	-886.5	-466	0.574	80.7	0.1424

TABLE 4.8: Calculated NMR parameters of $\alpha 2$

Atom	δ_{iso}(ppm)	Δ_δ (ppm)	η_δ	C_Q (MHz)	η_Q
Li1	–	6.3	0.695	0.190	0.9857
Li2	–	6.3	0.689	0.191	0.9874
Li3	–	4.3	0.875	0.320	0.4266
Nb4	-12.0	729.8	0.015	167.5	0.5535
Nb5	-383.4	-500.9	0.129	359.8	0.4227
Nb6	-36.8	-620.1	0.823	111.9	0.9464
Nb7	-376.6	-880.5	0.816	162.3	0.4893
Nb8	-368.4	-870.6	0.780	160.9	0.5228
Nb9	-439.8	-328.0	0.768	263.5	0.7730
Nb10	-428.9	-331.8	0.740	258.1	0.7393
Nb11	1.8	-1281.6	0.395	194.6	0.4914
Nb12	-348.0	-434.4	0.124	373.8	0.4464

TABLE 4.9: Calculated NMR parameters of $\alpha 4$

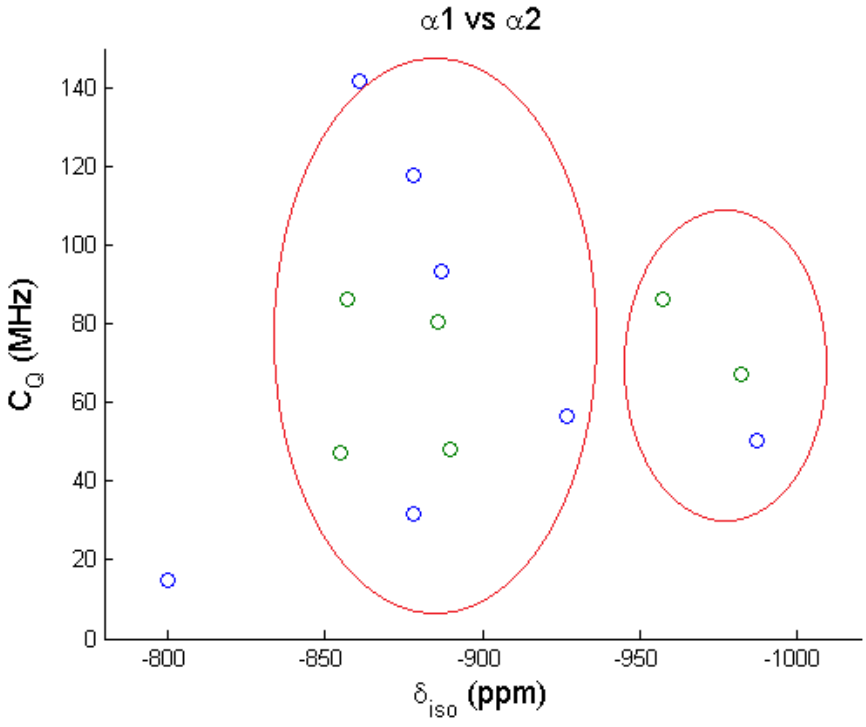

FIG. 4.6: The combined NMR parameter distribution for both $\alpha 1$ (blue circle) and $\alpha 2$ (green circle). The red ellipses are meant for a guide to the eyes only.

4.6 Conclusion

In this chapter, I have addressed the problem of local vs average structure of cation-ordered microwave dielectric materials. The use of DFT calculation helps for better understanding of the system. Due to the presence of disorder in group **1**, DFT calculation was performed only for group **2**. The preliminary test on niobium compounds gave promising results for the calculation of the real samples. The DFT calculations of lithium NMR parameters for both CLT and CLN show results which are very close to the measured values. Unfortunately, a good result within a reasonable accuracy is not possible to achieve with the current method. Two sets of calculation for CLN were performed which corresponds to 1:3 and 1:2 layering ordering. The calculations of NMR parameters for 1:3 layer ordering gave a very good results compare to the measured values. However, the calculations of NMR parameters for 1:2 layer ordering show broad distribution of chemical shifts and quadrupolar distributions. To get a more accurate calculation result, using a bigger unit cell which contain more number of atoms will be beneficial.

CHAPTER 5

Conclusion and Prognosis

My thesis work has led to a structural characterization of two different group of cation-ordered complex perovskite materials. The materials studied in this thesis, show high dielectric constant in microwave region, hence a good candidate for microwave telecommunication applications. All the crystal structure presented were characterized by X-ray diffraction to show an average structure of layer ordering. To give insight into the mechanism which give rise to high dielectric constant, also to find out differences between the average and local structures, Solid-state NMR was used as the key method to address these aspects.

The presence of many kinds of defects, which are the source of local disorder and lattice distortions, made the spectra acquired using traditional NMR technique very difficult to achieve. This hinder the local structure characterizations of the systems. At the same time, these systems are absolutely not trivial from the point of view of NMR spectroscopy, since they contain quadrupolar nuclei and/or paramagnetic centers. A satisfactory approach to this kind of materials was made possible only in the last years, thanks to the development both of the NMR hardware technology and of sophis-

ticated pulse sequences. Particularly relevant for the study of the systems presented in this thesis are the availability of very high-field magnet, fast-spinning probes, advanced electronic components of the spectrometers, and the use of adequate pulse sequences.

Using ^{7}Li and ^{93}Nb solid-state NMR spectroscopy, local structure characterizations for these systems were achieved. Lithium NMR parameters could be accurately calculated using model that incorporate quadrupolar and chemical shift interaction along with Euler angles which bring the chemical shift tensor to EFG principal axis. Niobium NMR measurements were found to show a distribution over NMR parameters (quadrupolar coupling and chemical shift isotropy). It is also possible to show this distribution with the help of quantum mechanical calculation. However, the source of disorder in the system was proven to be a challenge.

APPENDIX A

Transition Rate Equation; Spin-Lattice Relaxation by a fluctuating EFG

More generally, Eq. 3.4 can be written as

$$W_{mr,m'r'} = \frac{1}{\hbar^2} \times \int_0^t [\langle m', r'| \hat{H}_{Q,i}(t) |m, r\rangle \langle m', r'| \hat{H}_{Q,i}(t') |m, r\rangle + \langle m, r| \hat{H}_{Q,i}(t) |m', r'\rangle \langle m', r'| \hat{H}_{Q,i}(t') |m, r\rangle] dt' \quad \text{(A.1)}$$

It is usually assumed that the ensemble average $\overline{\langle m', r'| \hat{H}_{Q,i}(t) |m, r\rangle \langle m', r'| \hat{H}_{Q,i}(t') |m, r\rangle}$ vanishes for $|t - t'| \rightarrow \infty$. This means that the involved transitions become phase-incoherent after the time difference, $\tau_c = t - t'$. In addition, the correlations are assumed to be stationary, i.e., in the ensemble average the products of the matrix elements in A.1 are a function of the time difference, $t - t'$, only. For $\hat{H}_{Q,i}(t)$ we consider the time-dependent quadrupole Hamiltonian, and especially the fact that in the ensemble average, the matrix elements of $\hat{H}_{Q,i}$ vanish, $\overline{\langle m', r'| \hat{H}_{Q,i}(t) |m, r\rangle = 0}$, or the mean value is

considered to be part of the static quadrupole interaction. $\hat{H}_{Q,i}(t)$ can be written as,

$$\hat{H}_{Q,i}(t) = \frac{eQ}{2I(2I-1)} \sum_{q=-2}^{+2} (-1)^q T_q^{(2)} V_{-q,\mathrm{int}}^{(2)} \exp(i\omega_c t) \tag{A.2}$$

where $V_{-q,\mathrm{int}}^{(2)}$ is the operator for the components of the electric field gradient in the interaction picture and defined as

$$V_{-q,\mathrm{int}}^{(2)}(t) = \exp\{-\frac{i}{\hbar}(\hat{H}_L)t\} V_{-q}^{(2)}(t) \exp\{\frac{i}{\hbar}(\hat{H}_L)t\} \tag{A.3}$$

Eq. A.2 and Eq. A.3 show that the spin-dependent part of the quadrupole Hamiltonian restricts the transitions in the spin-system according to the matrix elements

$$\langle m'| T_0^{(2)} |m\rangle = \frac{3m^2 - I(I+1)}{\sqrt{6}} \delta_{m',m} \tag{A.4}$$

$$\langle m'| T_{\pm 1}^{(2)} |m\rangle = \mp(2m \pm 1) W_m^{\pm} \delta_{m',m\pm 1} \tag{A.5}$$

$$\langle m'| T_{\pm 2}^{(2)} |m\rangle = 2 W_{m\pm 1}^{\pm} W_m^{\pm} \delta_{m',m\pm 2} \tag{A.6}$$

where m is the quantum magnetic number for *Zeeman* interaction and

$$W_m^{\pm} = \frac{1}{2}\sqrt{(I \mp m)(I \pm m + 1)} \tag{A.7}$$

Since we are calculating the transition rates for $m \neq m'$, one is left with single- and double-quantum transitions. Therefore, we have

$$W_{mr,m'r'}^{\pm} = \frac{2}{\hbar^2}\Big[\frac{eQ}{2I(2I-1)}\Big]^2 \times \Big[(2m \pm 1)^2 (W_m^{\pm})^2 \widetilde{W}_1(r,r') \delta_{m',m\pm 1} + (2W_m^{\pm})^2 (W_{m\pm 1}^{\pm})^2 \widetilde{W}_2(r,r') \delta_{m',m\pm 2}\Big] \tag{A.8}$$

with

$$\widetilde{W}_n(r,r')\delta_{m',m\pm1} = \int_{-\infty}^{+\infty} \exp\{i[\pm n\omega_0 + (E_r - E'_r)/\hbar]\tau\} \times \mathrm{Re}\Big[\langle r'|\, V^{(2)}_{\pm2}(t)\,|r\rangle\, \langle r'|\, V^{(2)}_{\mp2}(t-\tau)\,|r\rangle\Big] d\tau \tag{A.9}$$

and given that

$$W_n(r,r') = \frac{e^2Q^2}{4I\hbar^2}\widetilde{W}_n(r,r') \tag{A.10}$$

We arrive at the general transition rate equation,

$$\begin{aligned} W_{mr,m'r'} = {} & \frac{(2m\pm1)^2(I\mp m)(I\pm m+1)}{(2I)(2I-1)^2} W_1(r,r')\delta_{m',m\pm1} \\ & + \frac{(I\mp m)(I\pm m+1)(I\pm m+2)}{(2I)(2I-1)^2} W_2(r,r')\delta_{m',m\pm2} \end{aligned} \tag{A.11}$$

APPENDIX B

Spin-Lattice Relaxation rate due to paramagnetic centers

When paramagnetic centers are present in the system, the nuclear spins are interacting with the time-varying local magnetic fields produced by these centers. This interaction can cause transition for the nuclear states and the transition probability of one nucleus due to a single paramagnetic center separated by distance *r* is given by

$$P = T_1^{-1} = 3(\gamma_n \gamma_p \hbar)^2 S(S+1) r^{-6} \sin^2\theta \cos^2\theta \frac{\tau_c}{1+\tau_c^2\omega^2} \tag{B.1}$$

where γ_n and γ_p is the gyromagnetic ratio of the nucleus and paramagnetic ion, respecitvely; θ is the angle between the line connecting nucleus and paramagnetic ion to static magnetic field; *S* is the spin of paramagnetic ion; τ_c is the correlation time of the *z*-component of paramagnetic ion spin.

By employing MAS to the system, the angular dependence of this interaction get

averaged over the angle θ so that equation (B.1) is replaced by,

$$T_1^{-1} = \frac{2}{5}(\gamma_n\gamma_p\hbar)^2 S(S+1) r^{-6} \frac{\tau_c}{1+\tau_c^2\omega^2} = \frac{C}{r^6} \tag{B.2}$$

with C = $\frac{2}{5}(\gamma_n\gamma_p\hbar)^2 S(S+1)\frac{\tau_c}{1+\tau_c^2\omega^2}$. Due to the inverse sixth power dependence on distance, only those nuclei close to the impurity are affected by this interaction, while the relaxation at lattice sites far from the impurity occurs by nuclear spin-spin diffusion.

If a saturation state is achieved initially, the nuclear magnetization will be built up most rapidly near the paramagnetic ion, as it is clear to see from equation (B.2). This gives rise to a spin-temperature gradient which causes spatial transport of nuclear magnetization. Assuming fixed position for both nuclear spins and paramagnetic ions, the nuclear spin magnetization per unit volume, *M*, is expressed as

$$\begin{aligned}\left(\frac{\partial M}{\partial t}\right)_{total} &= \left(\frac{\partial M}{\partial t}\right)_p + \left(\frac{\partial M}{\partial t}\right)_d \\ &= -\frac{(M-M_0)}{T_1} + D\nabla^2 M\end{aligned} \tag{B.3}$$

where M_0 is the equilibrium value of the magnetization per unit volume at the lattice temperature; *D* is spin diffusion constant; $\left(\frac{\partial M}{\partial t}\right)_p$ represents the rate of change due to direct interaction of the nuclear spins with paramagnetic ion; while $\left(\frac{\partial M}{\partial t}\right)_d$ represents the rate of change due to spin-spin diffusion magnetization transport. Letting $m = M - M_0$, equation (B.3) can be expressed as

$$\frac{\partial m}{\partial t} = D\nabla^2 m - \frac{C}{r^6} m \tag{B.4}$$

In general, this expression is very difficult to solve. Approximation is made by considering the concentration of paramagnetic impurity in the crystal is so small that each nuclear spin only being affected by one single paramagnetic ion. In solving equation (B.4), steady state solution is assumed. In addition, it also assumes that there is no magnetization transfer into the inside of a "barrier" i.e. $\left(\frac{\partial m}{\partial r}\right)_{r=b} = 0$ where *b* is barrier radius. There are three limiting cases need to be considered as they can give some physical insight about the system.

- Diffusion-dominant[1]

  This happens when the direct relaxation term is small and not able to establish a large spin-temperature. In this case, the transfer of nuclear magnetization is faster than the paramagnetic ion can equilibrate the nuclear spins surrounding it. The relaxation rate is given by

$$T_1^{-1} = \frac{4\pi N_p C}{3b^3} \propto B_0^{-2} \tag{B.5}$$

  where N_p is the paramagnetic ions density

- Diffusion-limited:

  For this case, the direct relaxation rate is large enough yet spin-spin diffusion can still happen. The relaxation rate is given by

$$T_1^{-1} = \frac{8\pi}{3} N_p C^{1/4} D^{3/4} \propto B_0^{-1/2} \tag{B.6}$$

- Diffusion-vanishing:

  When the direct relaxation term is too big, then the basic assumption of single paramagnetic center is not particularly valid anymore. In this case, it is important to think

[1] This is called rapid-diffusion in references

that the nuclei are relaxed by many paramagnetic centers. The relaxation rate is then given by

$$T_1^{-1} \approx 50 N_p^{3/4} C^{1/2} D^{1/2} \propto B_0^{-1} \tag{B.7}$$

BIBLIOGRAPHY

[1] A. Borisevich and P. K. Davies, Applied Physics Letter **84**, 1347 (2004).

[2] H. Wu, Ph.D. thesis, University of Pennsylvania (2005).

[3] C. C. Homes, T. Vogt, S. M. Shapiro, S. Wakimoto, and A. P. Ramirez, Science **293**, 673 (2001).

[4] A. Belous, *Dielectric Materials* (2012), vol. Microwave dielectrics based on complex oxide systems, in-tech ed.

[5] K. Wakino, K. Minai., and H. Tamura, J. Am. Ceram. Soc. **67**, 278 (1984).

[6] E. A. Nenasheva, L. P. Mudroliuba, and N. F. Kartenko, J. Eur. Ceram. Soc. **23**, 2443 (2003).

[7] R. I. Scott and C. Hampson, J. Eur. Ceram. Soc. **23**, 2467 (2003).

[8] C.-W. Ahn, H.-J. Jang, S. Nahm, H.-M. Park, and H.-J. Lee, J. Eur. Ceram. Soc. **23**, 2473 (2003).

[9] I.-N. Lin, C.-T. Chia, H.-L. Liu, H.-F. Cheng, and C.-C. Chi, Jpn. J. Appl. Phys **41**, 6952 (2002).

[10] C.-W. Ahn, S. Nahm, S.-J. Yun, H.-M. Park, and H.-J. Lee, Jpn. J. Appl. Phys **42**, 6964 (2003).

[11] A. G. Belous, J. Eur. Ceram. Soc. **26**, 1821 (2006).

[12] P. K. Davies, Matter. Sci. **4**, 467 (1999).

[13] P. K. Davies, H. Wu, A. Borisevich, I. E. Molodetsky, and L. Farber, Annu. Rev. Mater. Res. **38**, 369 (2008).

[14] F. Galasso, J. R. Barrante, and L. Katz, J. Am. Chem. Soc. **83**, 2830 (1961).

[15] H. Tamura, T. Konoike, Y. Sakabe, and K. Wakino, J. Am. Ceram. Soc. **67**, c59 (1984).

[16] I. G. Siny, R. Katiyar, and A. Bhalla, Journal of Raman Spectroscopy. **29**, 385 (1998).

[17] K. J. D. Mackenzie and M. E. Smith, *Multinuclear Solid-state NMR of inorganic Materials* (Pergamon, Oxford, 2002).

[18] A. Abragam, *The Principles of Nuclear Magnetism* (Oxford University Press, London, 1961).

[19] I. I. Rabi, J. R. Zacharias, S. Millman, and P. Kusch, Phys. Rev. **53**, 318 (1938).

[20] E. M. Purcell, H. C. Torrey, and R. V. Pound, Phys. Rev. **69**, 37 (1946).

[21] F. Bloch, W. W. Hansen, and M. Packard, Phys. Rev. **69**, 127 (1946).

[22] F. Bloch, Phys. Rev. **70**, 460 (1946).

[23] F. Bloch, W. W. Hansen, and M. Packard, Phys. Rev. **70**, 474 (1946).

[24] R. R. Ernst and W. A. Anderson, Rev. Sci. Instrum. **37**, 93 (1966).

[25] E. L. Hahn, Phys. Rev. **80**, 580 (1950).

[26] P. P. Man, Concepts Magn. Reson. **42**, 1552 (2013).

[27] N. F. Ramsey, Phys. Rev. **78**, 699 (1950).

[28] N. F. Ramsey, Phys. Rev. **83**, 540 (1951).

[29] N. F. Ramsey, Phys. Rev. **86**, 243 (1952).

[30] E. A. C. Lucken, *Nuclear Quadrupolar Coupling Constants* (Academic Press, London, 1969).

[31] M. Mehring, *Principle of High Resolution NMR in Solids* (Springer-Verlag, 1983), 2nd ed.

[32] J. W. Akitt and W. S. McDonald, J. magn. Reson. **58**, 401 (1984).

[33] O. Knop, E. M. Palmer, and R. W. Robinson, Acta. Crystallogr. Sect. A. **A31**, 19 (1975).

[34] A. P. M. Kentgens, Geoderma **80**, 271 (1997).

[35] A. Llor and J. Virlet, Chem. Phys. Lett. **152**, 248 (1988).

[36] A. Samoson, A. Lippmaa, and A. Pines, Mol. Phys. **65**, 1013 (1988).

[37] Y. Wu, B. Q. Sun, A. Pines, A. Samoson, and E. Lippmaa, J. Magn. Reson. **89**, 297 (1990).

[38] K. T. Mueller, B. Q. Sun, G. C. Chingas, and J. W. Zwanziger, J. Magn. Reson. **86**, 470 (1990).

[39] L. Frydman and J. S. Harwood, J. Am. Chem. Soc. **117**, 5367 (1995).

[40] M. H. Levitt and R. Freeman, Journal of Magn. Reson. **33**, 473 (1969).

[41] V. M. Goldschmidt, Die Naturwissenschaften **21**, 477 (1926).

[42] M. A. Pena and J. L. Pierro, Chem. Rev. **101**, 7 (2001).

[43] P. K. Davies, J. Tong, and T. Negas, J. Am. Ceram. Soc. **80**, 1727 (1997).

[44] L. Katz and R. Ward, Inorg. Chem **3**, 205 (1964).

[45] M. Akbas and P. K. Davies, J. Am. Ceram. Soc. **81**, 1061 (1998).

[46] A. Medek, J. S. Harwood, and L. Frydman, J. Am. Chem. Soc. **117**, 122779 (1995).

[47] A. Samoson, E. Kundla, and E. Lippmaa, J. Magn. Reson. **49**, 350 (1982).

[48] D. Massiot, F. Franck, M. Capron, I. King, S. L. Calve, B. Alonso, J. O. Durand, B. Bujoli, Z. Gan, and G. Hoatson, Magn. Reson. Chem. **40**, 70 (2002).

[49] C. Jager, G. Kunath, P. Losso, and G. Scheler, Solid state Nucl. Magn. Reson. **2**, 73 (1993).

[50] G. Czjzek, J. Fink, F. Gotz, H. Schmidt, J. M. D. Coey, J. P. Rebouillat, and A. Lienard, Phys. Rev. B: Condens. Matter **23**, 2513 (1981).

[51] J. P. d'Espinose de Lacaillerie, C. Fretigny, and D. Massiot, Journal of Magn. Reson. **192**, 244 (2008).

[52] O. B. Lapina, D. F. Khabibulin, A. A. Shubin, and V. V. Tersikh, Prog. Nucl. Magn. Reson. Spectrosc. **53**, 128 (2008).

[53] E. Papulovskiy, A. A. Shubin, V. V. Tersikh, C. J. Pickard, and O. B. Lapina, Phys. Chem. Chem. Phys **15**, 5115 (2013).

[54] D. H. Zhou, G. L. Hoatson, and R. L. VOld, Journal of Magn. Reson. **167**, 242 (2004).

[55] A. Flambard, L. Montagne, L. Delevoye, and S. Steuernagel, Solid State Nucl. Magn. Reson. **32**, 34 (2007).

[56] J. P. Amoureux and C. Fernandez, Solid state Nucl. Magn. Reson. **10**, 211 (1998).

[57] N. Bloembergen, Physica **25**, 386 (1949).

[58] J. V. Kranendonk, Physica **20**, 781 (1954).

[59] J. V. Kranendonk and M. B. Walker, Can. J. Phys. **46**, 2441 (1968).

[60] R. D. Shannon, Acta Cryst. **A32**, 751 (1976).

[61] G. R. Khutsishvili, Proc. Inst. Phys. Acad. Sci. Georgia (USSR) **4**, 3 (1956).

[62] P. G. De Gennes, J. Phys. Chem. Solids **7**, 345 (1958).

[63] W. E. Blumberg, Phys. Rev. **119**, 79 (1960).

[64] A. G. Rorschach Jr., Physica **30**, 38 (1964).

[65] I. J. Lowe and D. Tse, Phys. Rev. **166**, 279 (1968).

[66] M. I. Gordon and M. J. R. Hoch, J. Phys. C. **11**, 783 (1978).

[67] C. J. Pickard and F. Mauri, Phys. Rev. B. **63**, 245101 (2001).

[68] J. R. Yates, C. J. Pickard, and F. Mauri, Phys. Rev. B. **76**, 024401 (2007).

[69] P. Giannozzi, S. Baroni, N. Bonini, M. Calandra, R. Car, C. Cavazzoni, D. Ceresoli, G. L. Chiarotti, M. Cococcioni, I. Dabo, et al., J. Phys.: Condens. Matter **21**, 395502 (2009).

[70] L. H. Thomas, Proc. Cambridge Phil. Roy. Soc. **23**, 542 (1927).

[71] E. Fermi, Rend. Accad. Naz. **6**, 602 (1927).

[72] P. Hohenberg and W. Kohn, Phys. Rev. **136**, 864 (1964).

[73] W. Kohn and L. J. Sham, Phys. Rev. **140**, 1133 (1965).

[74] D. M. Ceperley and B. J. Alder, Phys. Rev. Lett **45**, 566 (1980).

[75] N. Troullier and J. L. Martins, Phys. Rev. B **43**, 1993 (1991).

[76] L. Kleinman and D. M. Bylander, Phys. Rev. Lett. **48**, 1425 (1982).

[77] D. Vanderbilt, Phys. Rev. B **41**, 7892 (1990).

[78] C. G. V. de Walle and P. E. Blöchl, Phys. Rev. B **47**, 4244 (1993).

[79] P. E. Blöchl, Phys. Rev. B **50**, 17953 (1994).

[80] H. M. Petrilli, P. E. Blöchl, P. Blaha, and K. Schwarz, Phys. Rev. B **57**, 14690 (1998).

[81] J. P. Perdew, K. Burke, and M. Ernzerhof, Phys. Rev. Lett. **77**, 3865 (1996).

[82] L. Truflandier, M. Paris, C. Payen, and F. Boucher, J. Phys. Chem. B **110**, 21403 (2006).

[83] J. V. Hanna, K. J. Pike, T. Charpentier, T. F. Kemp, M. E. Smith, B. E. G. Lucier, R. W. Schurko, and L. S. Cahill, Chem-Eur. J. **16**, 3222 (2010).

[84] A. D. Corso, Comp. Mat. Sci. **95**, 337 (2014).

VITA

Rony Gustam Kalfarisi

Rony Gustam Kalfarisi was born on August 15, 1985 in Medan, North Sumatra, Indonesia. He comes from low education family, his father graduated from technical school while his mother only graduated from elementary school. Since his young age, he was determined that one day he would study abroad. He realized that he was one step closer to his goal by getting scholarship for undergraduate to study physics at University of Pelita Harapan, Tangerang, Indonesia. His dream came true when he got accepted to continue his study in physics at College of William and Mary in Williamsburg, Virginia in 2010. In 2012, he joined Prof. Gina Hoatson and Dr. Robert Vold NMR spectroscopy group as an endeavour to develop his skill and interest in both physics and science.